A Relativistic Analysis of Proton-induced Knockout Reactions From Oxygen Isotopes With Direct and Inverse Kinematics.

by

Kanting Evidence Motimele

UNIVERSITY *of the*
WESTERN CAPE

A Dissertation presented to the Faculty of Natural Science in the Department of Physics and Astronomy

of

University of the Western Cape

In partial fulfilment of the requirements for the magister scientiae degree

Supervisors:

Prof. B.I.S Van der Ventel

Prof. R. Lindsay

November 2020

Abstract

A Relativistic Analysis of Proton-induced Knockout Reactions From Oxygen Isotopes With Direct and Inverse Kinematics.

by

Kanting Evidence Motimele

In this study a complete set of exclusive $(\vec{p}, 2p)$ polarization transfer observables of closed-shell oxygen isotopes are calculated using both direct and inverse kinematics using the relativistic plane wave impulse approximation. The interaction matrix is written in terms of the SPVAT (scalar, pseudoscalar, vector axial vector, tensor) covariants where each amplitude is obtained directly from experimental phase shifts. A relativistic mean field theory approximation is used to compute boundstate wave functions of the nucleons. We study the evolution of polarization transfer observables within oxygen isotopes and identify observables which may discriminate between these isotopes. The same kinematical conditions are considered for both direct and inverse kinematics: the incident energy is set at 504 MeV and coplanar angles are fixed at $(22.12°, -40.30°)$. The results indicate that only three spin observables, namely, A_y, P and D_{nn} distinguish different oxygen isotopes at these kinematical conditions in the inverse kinematics.

Declaration

I, the undersigned, declare that the work contained in this thesis, **Relativistic Analysis of Proton-induced Knockout Reactions From Oxygen Isotopes With Direct and Inverse Kinematics**, is my original work and has not previously in its entirety or part been submitted at any university for a degree, and that all the sources I have used or quoted have been indicated and acknowledged by complete references.

K.E Motimele	Date

Acknowledgements

I am grateful to the following people and institutions whose direct or indirect contributions have made this work a success:

- First and foremost, I would like to extend my sincere gratitude to my thesis supervisor Prof Van der Ventel for introducing me to this research field and giving the opportunity to do this work. Your support, devotion and dedication to me as your student has helped me enjoy every moment of this research. I learned a lot from you in the duration of this work on both a personal and academic level. I am immensely grateful for the knowledge and skills I developed under your supervision. Your patience, guidance and insights encouraged me to always look forward to our next meeting I already miss those meetings. I thank you for the confidence and trust you have in me.
- I also want to express my kind appreciations to my co-supervisor Prof Lindsay for unwavering and continued support and dedication to me as your student. Your willingness and swiftness to which you attend to my academic needs always amaze me. I thank you for the numerous opportunities and stimulating discussions we have had. I always felt welcomed every time I walked into your office without setting up a meeting which is all the time. I hope your office door remains widely open for other students after me to also drop into your office unannounced.
- Thanks to Prof Weigel of the Stellenbosch University for allowing me to drop in on his relativistic quantum mechanics and relativistic quantum field theory lectures in 2019 and 2020, respectively. This thesis has greatly benefited from the experience and knowledge gained from your lectures and for that I say thank you prof.
- I would like to extend my deepest gratitude to my countless family members and friends whose love, support and understanding were the driving force throughout the course of this academic journey.
- To the University of the Western Cape Physics Department and my peers there I'm thankful for warm hospitality I received from the first day.
- To National Research Fund (NRF) of South Africa I am grateful for the financial support.
- Finally, baie dankie to Stellenbosch University Department of Physics for allowing me to use their resources.

Contents

List of Figures

List of Tables

Chapter 1

Scientific Motivation

1.1 Introduction

At the low energies (<1 GeV) relevant to the structure and dynamics of nuclei, nucleons are the basic degrees of freedom. Nucleons are complex objects composed of quarks which interact via gluons. The underlying theory governing this interaction is called quantum chromodynamics (QCD). However, in the energy regime relevant to nuclear physics QCD is non-perturbative and very difficult to solve analytically and numerically. For many years, the nonrelativistic Shrödinger equation has been the dynamical equation of preference with nucleons treated as degrees of freedom in the investigations of nuclear structure and nucleon-nucleon (NN) interaction. However, in this work we will adopt a relativistic[1] framework within which to perform the investigations of nuclear structure and reactions of β-unstable nuclei lying far from the valley of stability. The nucleons are taken as fundamental degrees of freedom interacting via exchange of various mesons. The questions of great importance this study will try to answer are related to the understanding of the interaction between nucleons in the nuclear medium and its relationship to the underlying fundamental interactions to the understanding of the many-body manifestations of the nucleus as a system of correlated fermions. This will be achieved by looking at the groundstate properties of nuclei such as total binding energy, single-nucleon energies and wave functions, density profiles etc.

The choice of relativistic formalism is motivated by the immense success this formalism has enjoyed in the description of nuclear structure and nuclear scattering phenomena of both stable and exotic nuclei. The relativistic formalisms point to the importance of relativistic effects and provide natural explanations for the observed features of nuclear matter. The potential of the relativistic approach became apparent in the very early history of quantum field theory (QFT) when it was recognised that the concept of spin within the relativistic dynamics is intrinsic, i.e., it occurs as a natural consequence of using the relativistic Dirac equation. There are many consequences of taking a relativistic approach to solving fundamental nuclear physics problems. This will be motivated below.

Nonrelativistic nuclear physics based on the solution of the Shrödinger equation has provided exceptional theoretical results over the past decades. In recent years there has been a successful application of ab initio methods of nuclear physics. Ab initio nuclear theory describe the atomic nucleus beginning from all constituent nucleons and the fundamental forces between them and aims at predicting the properties of nuclei. The idea is to solve the nonrelativistic Shrödinger equation and derive accurate nuclear interactions using chiral effective field theory (EFT). This effective field theory (EFT) includes all interactions compatible with the symmetries of QCD, ordered by the size of

[1] By relativistic we mean that the dynamical equation of motion is the Dirac Equation with its relativistic treatment of the dynamics and kinematics

their contributions. The degrees of freedom in EFT are nucleons and pions. The common techniques used in the exact ab initio calculations [4, 5, 6, 7] for very light nuclei ($A = 3, 4$) involve solving the nonrelativistic many-nucleon Schrödinger equation with the inter-nucleon interactions as the only input. There exists plenty of ab initio calculations that are applicable to medium and heavy nuclei. The enormous progress made in the last 10 years in this theory is largely due to the powerful ab initio approaches and high-performance computing chiral EFT. In this dissertation we take a rather modest approach as opposed to that of ab initio theory. We study the nuclear structure of unstable nuclei in the framework of relativistic mean field theory and proton knockout scattering reactions with unstable nuclei of are investigated within the context of relativistic impulse approximation.

In the 1970s the idea that nuclear dynamics should be described within a relativistic framework gained traction following the success of quantum hydrodynamics (QHD) of Walecka [8, 9]. QHD is a model for the study of the relativistic nuclear many-body problem through an effective Lagrangian field theory. It describes nuclear matter as resulting from interactions between nucleons (baryons) in the nucleus through the exchange of mesons. A relativistic mean field approximation to QHD provides a framework to describe nuclear structure of finite and infinite nuclear matter using a minimal number of phenomenological parameters . The relativistic treatment of fundamental nuclear physics problems proved to provide satisfactory explanations to nuclear phenomena such as small binding energy, large spin-splitting, nuclear saturation and density dependence of the interaction. For instance, the density dependence of the interaction is due to the fact that the vector and scalar potentials have different density dependences. The differences between the vector and scalar potentials give rise to nuclear saturation in this model. The saturation of nuclear matter explains why there is only a limited number of stable nuclei in nature. The small binding energy of saturation is explained as a consequence of fine cancellation between large scalar potential and large vector potential. The model also explains the existence of a nuclear shell model with the experimentally observed level orderings, spacings, and major shell closures in nuclei. In the relativistic structure, a large spin-splitting, which is consistent with experimental observations appears naturally.

The medium energy (100-1000 MeV) nucleon-nucleus scattering physics has its origin in the 1950s and, to date, continues to provide enormous information in the studies of nuclear structure and NN interaction. The medium-energy nuclear physics is only a part of grand efforts to gain comprehensive understanding of the nature of strong forces responsible for nucleon-nucleon interactions in complex many-body systems. The experiments performed at intermediate energy allow us to focus on the NN interaction because at these energies knowledge of excited states is irrelevant. Furthermore, the medium energy scattering and small scattering angles invoke impulse approximation. The relativistic impulse approximation constitutes the cornerstone of this theoretical study. The impulse approximation assumes that the scattering process proceeds through the interaction of the incident projectile with individual nucleons in the nucleus as opposed to interacting with the nucleus as a whole. Furthermore, the approximation assumes that the nature of the interaction between the projectile and the bound nucleon is identical to the nature of the interaction between a projectile and a free nucleon, apart from including the binding aspect of the nucleon. One of the major goals of this study is to investigate the scattering of incident medium energy neutron rich nuclei off a proton target for inverse kinematics. The topical question that needs to be answered is how the free NN interaction is modified in the nuclear medium: the exclusive nature of $(p, 2p)$ reactions allows one to selectively knockout protons from deep- to low-lying single-particle orbitals in nuclei, thus enabling one to systematically study the effect of the nuclear density on the NN interaction.

The relativistic analysis of scattering reactions began with the pioneering work of Clark and collaborators [10, 11, 12, 13, 14] when they solved the Dirac equation with large attractive vector and a large repulsive phenomenological potentials to obtain excellent quantitative results for proton-nucleus spin observables. McNeil, Shepard and Wallace developed a parameter-free theoretical description called the relativistic impulse approximation (RIA) which was in accordance with the results of Clark

et. al [15, 16]. The relativistic impulse approximation models are Lorentz covariant allowing for reliable extrapolation to extreme conditions of density, temperature or momentum transfer. The ability of relativistic models to describe elastic and inelastic proton-nucleus spin observables combined with failures of the nonrelativistic Shrödinger equation-based models to describe the analysing power for quasielastic (p, p') scattering at 500 MeV from ^{40}Ca and ^{208}Pb targets, lead to the development of the Relativistic (Dirac) Plane Wave Impulse Approximation (RPWIA) for quasielastic proton-nucleus scattering [17]. The relativistic NN amplitudes are based on a Lorentz-invariant parametrization of the standard five Fermi invariants (the so-called SVPAT form). In the RPWIA strong optical scalar and time-like vector components of mean-fields in the medium enhance the lower components of the Dirac nucleon wave functions of the projectile and target nucleons through effective masses as derived in relativistic mean-field theory. It is through the use of an effective nucleon mass that the effect of the spectator nucleons is taken into account, i.e., the fact that scattering takes place inside the nuclear medium.

1.2 Exclusive Proton Knockout Reactions

The exclusive proton knockout reaction $A(a, a'b')C$ refers to a process wherein an incident proton a with intermediate energy (100 - 1000 MeV) knocks out a bound proton b from a stationary target nucleus A. The two protons (scattered projectile and the ejected nucleon) are detected as a correlated, coplanar pair. The kinematical properties of the two scattered protons and of the residual fragment carry valuable spectroscopic information about the particular quantum state of the struck proton such as, for instance, its internal momentum and single-nucleon separation energy. Experiments of this kind were first observed in 1952 at Berkeley laboratory [18, 19]. The explanation of the direct proton-proton scattering mechanism inside the nucleus was provided in a number of later experiments [20, 21, 22, 23]. At intermediate energy range, the mean free path of a proton inside a nuclear matter is of order of magnitude comparable to the nuclear radius and the interaction is strongly localized, since the de Broglie wavelength[2]of the projectile is smaller than the average inter-nucleon distance in the nucleus. The initial investigations of quasifree reactions focused solely on $(p, 2p)$ knockout reactions but they have since been extended to include other quasifree scattering processes such as $(e, e'p)$, $(\pi, \pi'p)$, (p, pn), (p, pd) and $(\alpha, 2\alpha)$ [24].

Quasifree scattering (QFS) using direct kinematics with stable beams has provided enormous information on the single-particle properties of nuclei (such as single-nucleon separation energies, wave-functions and spectroscopic factors) [24] along the stability line. This reaction mechanism alone offers the possibility to study not only the outer part but also allows the direct exploration of deeper regions inside the nucleus. Besides, the use in the study of single particle properties of the nuclear structure proton knockout reactions are a powerful tool to study the nature of the strong interaction in nuclear matter. Since the process involves NN scattering in the nuclear field, quasifree scattering provides a direct mechanism to investigate the NN interaction inside the nuclear medium [25]. It was recognized early on in the history of proton knockout reactions that they can be used to study the nature of the strong nuclear interaction in the nuclear medium [26]. However, investigations in this fashion had to wait for the progress in the development of the theoretical description of effective NN interaction in the 1980's [27], as well as the availability of high quality polarized beams. Polarized particle beams necessitate the measurement of spin observables, considered to be a more stringent test of reaction models than cross-sections. In this study we will calculate a complete set of exclusive $(p, 2p)$ spin observables to investigate the nature of NN interaction in some selected nuclei located away from the valley of stability.

The exclusive $(p, 2p)$ reaction is preferred over inclusive quasielastic (p, p') for the measurement of polarization transfer observables for the following reasons:

[2]The de Broglie wavelength is defined as $\lambda = hc/pc$ with p the particle's momentum

1. The ambiguities in nuclear structure and reaction mechanisms present in the description of quasielastic scattering are minimized in exclusive $(p, 2p)$ scattering processes.

2. The quasielastic scattering deals with the superposition of scattering amplitudes of all nucleons of the nucleus whereas quasifree knockout deals basically with the scattering amplitude of a single nucleon [28].

3. An additional advantage of exclusive over inclusive quasifree scattering is that the two-body kinematics can be specified through the experimental setup.

The theoretical and experimental developments of quasifree proton $(p, 2p)$ and electron $(e, e'p)$ scattering from stable nuclei have taken place at the same time and their results have been complementary [29, 30]. The advantage of this was that the the results obtained from quasifree proton $(p, 2p)$could be compared to those coming from quasifree proton $(e, e'p)$. The electron induced reactions have the advantage of high accuracy of such measurements because electrons have longer mean free path in nuclear matter thus reducing the distortion to just one of the outgoing particles. The electron-induced knockout reactions are sensitive to the whole volume of the nucleus from surface to the centre, and therefore they are ideal for studying the sensitivity of the spectroscopic factors to the radius. The near model independence of $(e, e'p)$ reactions is an attractive feature but these reactions have low cross sections, due to the fact electrons interact with the nuclear matter only via electromagnetic interaction [29]. The small electromagnetic cross section of electron-induced reactions combined with biased selectivity for reaction with protons is an undesirable feature to study single-particle states of neutrons, which are of a great interest in particular for investigation of the nuclear structure in exotic nuclei with a large neutron-proton asymmetry. Furthermore, despite being much easier to handle theoretically, the measurement of $(e, e'p)$ cross sections requires double coincidence which is difficult. The challenges associated with using electron-induced reactions in the investigations of the structure of exotic nuclei will be addressed by an experiment such as The ELectron Ion Scattering experiment (ELISe) [31]. In such experiments it will be possible to measure the scattering of electrons off radioactive nuclei to study the nuclear structure of exotic nuclei.

Despite the unique opportunity to utilise electrons as probe to explore the structure of exotic nuclei that will be provided by experiments such as ELISe, the $(p, 2p)$ reaction offers a number of advantages. For instance, in the studies of deeply bound nuclear states, the possibilities offered by $(p, 2p)$ are almost unparalleled. Moreover, the lower accuracy of $(p, 2p)$ due to the larger distortion in the nuclear medium is partially compensated for by their much higher cross sections and the possibility of the study of neutron knockout [29]. However, quasifree scattering (QFS) in direct kinematics with stable beams are limited to the study of the nuclei lying in the stability region. The quick-fix solution is to make stationary targets of unstable isotopes, however in practice, it is very difficult to produce such isotopes as they are short-lived, for that reason, the experiments with inverse kinematics are required. In the inverse kinematics a radioactive nuclear beam composed of nuclei of interest collides with a proton target (e.g., liquid hydrogen, CH2, etc). In terms of inverse kinematics, the quasifree scattering process proceed via a single collision between an energetic nucleon in a projectile nucleus and the proton target. This interaction is strongly localized if the projectile has intermediate energy range and the nucleon removal process can be seen as an interaction between the (quasi) free nucleon of the projectile nucleus and the target proton. The proton target increases the sensitivity to the more deeply bound states. In addition, if the appropriate choice for incident energy is made, the rescattering in the final state can be minimized, since the nucleon-nucleon interaction cross-section reaches its minimum around 250 - 350 MeV.

The study of unstable nuclei with inverse kinematics has already revealed the secrets hidden in the vastness of nuclear landscape. One of the first experiments with unstable beams showed that when the interaction cross sections of light isotopes of lithium and beryllium were measured [32, 33], they exhibited much larger radii than was predicted for stable nuclei via the empirical nuclear radius

formula. The apparent deviation from the empirical relation is attributed to a phenomenon called nuclear 'halo' wherein a core of protons and neutrons can appear to be spatially separated from pure neutron matter that surrounds it like a halo-like structure. Single nucleon knockout reactions have also proven useful for other structure investigations in nuclei such as, observing the breakdown of the $N = 8$ shell gap e.g. in the neutron-rich ^{12}Be [34] along with other investigations into the breakdown of known shell gaps and the emergence of new ones in the so-called 'island of inversion' [35].

1.3 Exotic Nuclei

There are less than three hundred (300) stable or long-lived nuclides which are found along the valley of stability in the nuclear chart. The stable and near stable nuclei studied to date show only a glimpse of the many complexities that nuclear matter can pose. A much richer view will be revealed in the study of nuclei with extreme proton-neutron composition which is the critical feature of radioactive nuclear beams (RNBs). When the unstable nuclei, the number is now over three thousand[3][36], are explored, many exotic nuclear phenomena have been observed such as the nuclear halo [37], quenching of magic numbers [38], new collective excitation modes [39] etc. The N/Z ratio between the number of neutrons and protons gives an accurate indication of whether the nucleus is stable or unstable. In stable nuclei, the ratio N/Z indicates that proton-neutron system is at equilibrium and occurs in nature. Contrastingly, unstable nuclei tend to undergo a beta decay (thus changing the ratio N/Z) to reach equilibrium, i.e., more tightly bound nuclei at the valley of stability. Such nuclei have unusual N/Z ratio and are typically short-lived compared to the nuclei lying in valley of stability. The further the nucleus is from the region of stability in the nuclear chart, the shorter its lifetime. The isotopes found far from stability are often referred to as radioactive isotopes or exotic nuclei. Exotic nuclei come in two configurations subject to whether they have excess neutrons or deficiency in neutrons relative to stable nuclei: neutron-rich or neutron-deficient. The neutron-deficient nuclei are less extended compared to neutron-rich nuclei since the Coulomb interaction between protons in the nucleus overcomes strong nuclear force limiting the number of protons that can be added in a chain. Exotic nuclei have their existence limit beyond which no more neutrons/protons can be added. This limit is called the neutron/proton drip line collectively. The proton drip line has been experimentally established up to protactinium ($Z = 91$). The presence of proton drip line near the stability valley is due to Coulomb interaction. The neutron drip line has only been identified for light nuclei up to $Z \leq 8$ and their precise location in the nuclear chart has not yet been pinpointed. For the most isotopic chains the neutron drip lines remain elusive. Since neutrons do not possess an electric charge and neither attraction nor repulsion exists between them, numerous neutrons may be clustered into nuclei starting from the valley of stability. Consequently, the nuclear landscape separating the neutron drip line and the valley of stability is large and difficult to probe experimentally.

In stable nuclei, the magic numbers predicted by the shell model and observed experimentally are valid, but away from the valley of stability towards exotic nuclei, which are nuclei close to the drip-lines, the large energy gaps which characterize magic nuclei are not that pronounced or become quenched and in some cases new ones can appear. The experimental observations reveal that neutron shells $N = 8$, 20 for stable nuclei disappear in very neutron-rich nuclei and are replaced with $N = 6$, 16 shells [40]. As a result, some exotic nuclei that were expected to be magic are not and others, which were not expected, turn out to be magic nuclei. This shell quenching in exotic nuclei is predicted for neutron numbers all the way up to the $N = 82$ shell closure, while for protons it appears to stop much sooner ($Z = 20$). This is because the Coulomb force prevents the descent of higher energy orbitals from the continuum approaching the bound states [41], a process that is often linked to shell quenching. Observation of $N = 82$ shell quenching, would shed light on the astrophysical r-process by allowing a better fit of the data we have for element abundances [42].

[3]The theoretical prediction put the number at 7000

To drive the point home by means of an example: the expected magic numbers $N = 8$ in ^{11}Li and $N = 20$ for the oxygen isotopes can not be confirmed by experiments. The shell model predicts ^{11}Li to be a magic nucleus, with the two valence neutrons in the orbital $1p^{1/2}$. However, experiments [32, 33] observe a large radius and a mixture of the $1p^{1/2}$ and the $1s^{1/2}$ shells in this nucleus, resulting in the disappearance of the magicity of the $N = 8$. In the case of the oxygen isotopic chain, the chain finishes at ^{24}O and the neutron drip line for the oxygen isotopes starts with ^{26}O and therefore, there is no evidence for ^{28}O to be bound, consequently, the $N = 20$ vanishes as magic number. Experimental evidence suggests that in the oxygen isotope ^{24}O the valence neutrons mainly populate the $2s^{1/2}$ orbital, creating a large gap between the $2s^{1/2}$ and $1d^{3/2}$ orbits making this nucleus doubly magic [43, 44, 45]. It has been observed [46] that the energy of the first excited state for ^{22}O is relatively high making $N = 14$ a sub-shell closure for the oxygen isotopes. This behaviour seen in $N = 14$ is not observed with the same strength for the ^{21}N [47, 48] and it has vanished for ^{20}C [49]. All these works show that the magic numbers are not universal along the nuclear landscape as it was thought; they evolve when we move far from the β-stability.

Accelerator facilities have immensely contributed to the understanding and knowledge of atomic nuclei especially those lying along the valley of stability, experimental data obtained from these facilities is essential in the development and refinement of theoretical models. The production of radioactive nuclear beams has enabled the investigations of new territories of the nuclear landscape far from the β-stability line. Moreover, this allows one to also test the validity of the models that were developed to explore nuclei in the stability valley. There are two main techniques used for the production of unstable ions namely Isotope Separation On-Line (ISOL), and in-flight separation. In the ISOL method, a primary beam bombards a thick production target and depending on the composition of the target, a range of different species are produced through various reaction mechanisms, such as fragmentation, fission and spallation. The ions of interest are then extracted from the production target and guided through an electromagnetic mass analyser, which separates different masses. If there is a chemical element that is not ionised, laser ionization may be used to selectively ionize specific elements. Finally, the selected ions can be re-accelerated if necessary.

In the in-flight separation technique, a primary beam impinges on the thin production target. It is often essential for the primary beam to be heavy and energetic so that reaction fragments can recoil out of the thin target. The in-flight method has the advantage of applicability to short-lived RNBs and does not depend on the chemistry of unstable ions. It is worth mentioning that this technique is not restricted to high energy beams, in fact, at Notre Dame University there is a complete programme that utilises low-energy RIBs for in-flight method and unlike the ISOL method it can produce almost all ions between the proton and neutron drip lines. The ISOL technique produces ions with higher intensities and better optical qualities than the ones produced by the in-flight technique. Some of the operational accelerator facilities that use ISOL for RNBs production are REX-ISOLDE at CERN (Switzerland), SPIRAL at GANIL (France) and Louvail-la-Neuve (Belgium). The following are some of the operational facilities which use in-flight separation method: A1900 at NSCL (USA), SISSI-ALPHA at GANIL (France) and RIPS at RIKEN (Japan). Many more RIB accelerator facilities are planned and most of them will become operational in the near future[4]. For further details on different aspects of ISOL and in-flight techniques the interested reader can consult the following reviews [50, 51, 52] and [53, 54] references of the therein.

1.4 Objectives of this Study

We mentioned the objectives of this study in passing in the previous sections. Here we list the main objectives we seek to accomplish in this work.

[4] *see* http://www-elsa.physik.uni-bonn.de/accelerator_list.html for a complete list

1. To write the new relativistic mean field theory codes which incorporates pairing correlation for the study of exotic nuclei.

2. To study the nuclear structure, in particular, groundstate properties and variety of nuclear phenomena, of nuclei throughout the nuclear landscape within the framework of relativistic mean field theory.

3. To perform the first study of a complete set of the exclusive $(p, 2p)$ spin observables of exotic nuclei with inverse kinematics.

4. Finally, compare spin observables of magic oxygen isotopes to gauge medium modification as nuclei become neutron-rich.

1.5 Organization of Dissertation

We want to highlight that in this work exclusive $(p, 2p)$ knockout reaction refers to the nuclear reactions in which all the protons are polarized unless stated otherwise. In the direct kinematics, the incident proton is polarized and the two outgoing (scattered and knocked out) protons are polarized. There is a large body of theoretical and experimental work dedicated to these types of reactions see latest review in Ref. [55]. For the inverse kinematics, a target proton is polarized and the two outgoing protons are also polarized. The experimental investigations of exclusive $(p, 2p)$ knockout reaction with inverse kinematics have only been achievable in the recent years [56]. RIKEN facility in Japan is one of the leading RIB laboratories investigating unstable nuclei with polarized proton targets. As far as we know there has never been any theoretical study looking at spin observables of the exclusive $(p, 2p)$ knockout reaction with inverse kinematics. We are encouraged by the developments taking place at RIKEN that in the near future it will be possible to measure a complete set of spin polarization observables for exclusive $(p, 2p)$ knockout reaction with inverse kinematics and hence, we undertake this theoretical task. In this manuscript, we adopt the conventions of Bjorken and Drell [57]. Furthermore, all kinematic quantities are expressed in natural units $\hbar, = c = 1$, unless stated otherwise.

In chapter 2 we present the nuclear structure of both stable and unstable nuclei nuclei within the context of relativistic mean field theory. A systematic theoretical study of oxygen isotopes is performed for exclusive $(p, 2p)$ scattering reactions with direct and inverse kinematics, and analysed within the relativistic impulse approximation framework in chapter 3. Chapter 5 is devoted to the summary and outlook.

Chapter 2

RELATIVISTIC MEAN FIELD THEORY

2.1 Introduction

The primary goal of nuclear physics is to provide a comprehensive description of the nature of the interaction between two or more nucleons in complex many-body systems such as finite nuclei and neutron stars. The quantum chromodynamics (QCD) of quarks and gluons is a fundamental theory of strong interactions. QCD describes the interaction between quarks through the exchange of gluons. Hence, it is reasonable to expect QCD to explain possible modification to hadron properties in the nuclear medium. However, enormous challenges make it an insurmountable task to solve the theory in the non-perturbative regime of relevance to nuclear systems. The problem of studying nuclear systems in a relativistic formalism from first principles of QCD is circumvented by formulating a consistent microscopic treatment of nuclear systems using hadronic degrees of freedom. A relativistic description of nuclear many-body problem based on hadrons as degrees of freedom is known as quantum hadrodynamics (QHD). In this theory, the strong interaction between nucleons in finite nuclei and extended nucleonic matter is due to the exchange of various mesons (quanta of nuclear force). Although, QHD is an effective field theory it is constrained by QCD symmetries: parity invariance, Lorentz invariance, isospin symmetry, electromagnetic gauge invariance and chiral symmetry. This formulation offers several advantages: (i) in nuclear experiments hadrons are the actual degrees of freedoms that are observed as opposed to quarks which are more fundamental and are described by QCD, (ii) the hadronic calculations can be calibrated by requiring that they reproduce empirical nuclear properties and scattering observables, (iii) and QHD allows for the mesonic degrees of freedom to be included at the beginning of the development of the model and principles of causality, retardation and relativistic kinematics can be easily incorporated in the relativistic field theoretic approach.

The first successful QHD model [8] was formulated by taking into account only the contributions of σ and ω mesons to the Lagrangian density and no nonlinear terms were incorporated. The model was introduced by Walecka in 1974 and to distinguish it from subsequent QHD models it is called QHD-I or the $\sigma - \omega$ model. Since the introduction of QHD-I, many other QHD models have been developed to address various inadequacies of the $\sigma - \omega$ model. The extension by Serot, referred to as QHD-II model [58], in addition, to σ and ω mesons includes charged vector ρ and charged pseudoscalar π mesons. This model also incorporates the electromagnetic interaction through the photon field A_μ to account for the Coulomb repulsion between protons in nuclei.

The mesons are selected according to their quantum properties: parity, spin and isospin. The isoscalar-scalar field σ, with quantum numbers $(J^\pi, T) = (0^+, 0)$ mediates a long- and mid-range

attraction between nucleons. Within relativistic mean field (RMF) theory, it is included as an effective field to simulate the two-pion exchange of the nuclear force and it is responsible for the intermediate range attractive part of the nucleon-nucleon interaction. The isoscalar-vector ω $(1^+, 0)$ is included to reproduce the short-range repulsive interaction. An isovector-vector ρ $(1^-, 1)$ is needed to describe the dependence of the nuclear force on isospin. In principle[1], other mesons can also be included such as the π $(0^-, 1)$[2] and η mesons which are pseudoscalar in nature and do not obey the ground-state parity symmetry. It can be shown that pseudoscalar mesons do not enter in the relativistic Hartree approximation when the nuclear ground state is spherically symmetric and a parity eigenstate.

When the parameter set of QHD-I is fitted to reproduce bulk properties of the nuclear matter, unreasonably large compressibility $K \approx 550$ MeV is predicted as opposed to experimentally observed value of $K = 210 \pm 30$ MeV from breathing mode energy experiments. This is due to the absence of non-linear terms in the original Walecka model. The non-linear terms ensure self-interaction of mesons. Buguta and Bodmer [59] introduced the σ self-coupling in the Lagrangian density in order to improve the calculation of the incompressibility of the nuclear matter. The inclusion of the scalar σ meson self-couplings led to a better prediction of finite nuclei properties and improved value of the incompressibility of the nuclear matter. There is a huge number of parameter sets such as NL1 [60], NL2 [61] and NL-SH [62] inspired by Lagrangian density containing σ meson self-coupling terms. However, these parametrizations fail to reproduce the nuclear properties of unstable nuclei in a satisfactory manner. Thus, the failure led to the introduction of the ω self-coupling term in the Lagrangian density. This resulted in parameter sets TM1 [63] and TM2 [63] which reproduce the nuclear properties of light and heavy unstable nuclei, respectively. The PK1 [64] parameter set was developed as an improvement on TM1. The PK1 parameter set provides improved prediction of the nuclear symmetry energy and compressibility. The NL3 [2] parameter set was introduced to address various shortcomings of RMF models and proved to predict experimental values very well for both stable and unstable nuclei. However, it was suggested that the NL3 parameter set only reproduces the giant monopole resonance (GMR) in ^{280}Pb by accident. It was hypothesised that if that were true the NL3 model would have to overestimate the giant monopole resonance (GMR) in ^{90}Zr and underestimate the isovector giant dipole resonance (IVGDR) in ^{280}Pb. The results agreed with the hypothesis and led to the development of FSUGold parameter set [3] which is an accurately calibrated RMF model. The FSUGold introduces a coupling term between ω meson and ρ meson to improve density dependence of the nuclear asymmetry energy without altering saturation of the nuclear matter. FSUGold introduces two isovector-scalar coupling terms that are absent in NL3. In this work we will employ the parameter sets of NL3 and FSUGold models. *See* Table 2.2.

In the next section we provide the formalism of our model based on the effective Lagrangian density of QHD, we also make two important assumptions: no sea approximation and mean field approximation. In the no sea approximation, all the contributions from antiparicles are neglected. It is employed in plenty of relativistic models at mean field, Hartree-Fock and Bethe-Brueckner-Goldstone treatment. The mean field approximation cuts down all the quantum fluctuations from meson fields and as a result meson fields can be treated as classical fields. This removes many-body effects because the nucleons move independently in the common mean field.

[1] In this STUDY we deal with nuclear states having good parity hence we shall only consider the mesons with natural parity $\pi = (-1)^J$. The currents with unnatural parity have vanishing expectation values.

[2] The pionic field is a basic ingredient of microscopic nuclear force that does not enter at classical Hartree level because it leads to parity breaking field which has not been observed in actual nuclei.

Table 2.1: The fields in NL3 and FSUGold

Field	Description	Particles	Mass	coupling
ψ	Baryon	$p, n, \ldots$	M	
ϕ	Neutral scalar meson	σ	m_s	$g_s\bar{\psi}\phi\psi$
V_μ	Neutral vector meson	ω	$m_{\rm v}$	$g_{\rm v}\bar{\psi}\gamma^\mu V_\mu\psi$
π	Charged pseudoscalar meson	π	m_π	$ig_\pi\bar{\psi}\gamma^5\boldsymbol{\tau}\cdot\boldsymbol{\pi}\psi$
$\mathbf{b}_\mu$	Charged vector meson	ρ	m_ρ	$\frac{1}{2}g_\rho\bar{\psi}\gamma^\mu\boldsymbol{\tau}\cdot\mathbf{b}_\mu\psi$
A_μ	Photon	γ	$m_\gamma = 0$	$e\bar{\psi}\gamma^\mu\frac{1}{2}(1+\tau_3)A_\mu\psi$

2.2 Lagrangian Density

In this section, we present quantum hadrodynamics within the framework of relativistic mean field theory wherein the nucleons in the many-body systems, interact via the exchange of various mesons and the photon mediate electromagnetic interaction between protons. The total Lagrangian density for quantum hadrodynamics is given by

$$\mathcal{L} = \mathcal{L}_0 + \mathcal{L}_{int}, \tag{2.1}$$

where the first term in equation (2.1) represents the Lagrangian density for particles in free space

$$\begin{aligned}\mathcal{L}_0 = \bar{\psi}(i\gamma^\mu\partial_\mu - M)\psi + \frac{1}{2}\partial^\mu\phi\partial_\mu\phi - \frac{1}{2}m_s^2\phi^2 - \frac{1}{4}V^{\mu\nu}V_{\mu\nu} \\ + \frac{1}{2}m_{\rm v}^2V^\mu V_\mu - \frac{1}{4}\mathbf{b}^{\mu\nu}\cdot\mathbf{b}_{\mu\nu} + \frac{1}{2}m_\rho^2\mathbf{b}^\mu\cdot\mathbf{b}_\mu - \frac{1}{4}F^{\mu\nu}F_{\mu\nu}\ .\end{aligned} \tag{2.2}$$

Refer to the above Table 2.1 for the meaning of various fields. The field tensors for the vector mesons and electromagnetic field are defined as:

$$V_{\mu\nu} = \partial_\mu V_\nu - \partial_\nu V_\mu, \tag{2.3}$$
$$\mathbf{b}_{\mu\nu} = \partial_\mu\mathbf{b}_\nu - \partial_\nu\mathbf{b}_\mu, \tag{2.4}$$
$$F_{\mu\nu} = \partial_\mu A_\nu - \partial_\nu A_\mu, \tag{2.5}$$

where ψ is the isodoublet nucleon field, A_μ is the massless photon field, and ϕ, V_μ, and $\mathbf{b}$ represent the isoscalar scalar $\sigma-$, isoscalar-vector $\omega-$, and isovector-vector ρ-meson field, respectively.

The strong nuclear force between the nucleons (i.e., protons and neutrons) is mediated by isoscalar and isovector mesons. The isoscalar mesons are blind to the isospin of nucleons and thus interact with protons and neutrons in exactly same way whereas the isovector mesons, on the other hand, can distinguish nucleons according to their isospin, and thus, interact with protons and neutrons in different ways. The interaction between various particles is contained in the second term of Eq. (2.1) and has the following form:

$$\mathcal{L}_{int} = \bar{\psi}\big[g_s\phi - (g_{\rm v}V_\mu + \frac{g_\rho}{2}\boldsymbol{\tau}\cdot\mathbf{b}_\mu + \frac{e}{2}(1+\tau_3)A_\mu)\gamma^\mu\big] - U_{\rm eff}(\phi, V^\mu, \mathbf{b}^\mu). \tag{2.6}$$

Here $\boldsymbol{\tau}$ are the isospin Pauli matrices and τ_3 is the third component of $\boldsymbol{\tau}$. Note that $(1+\tau_3) = \tau_p$ is the isospin projection operator which projects out proton from the isodoublet nucleon field since it is the one interacting with the photon. The first term in Eq. (2.6) contains the conventional Yukawa couplings between the nucleons and the mesons. The self and mixed non-linear meson interactions are incorporated in the last term $U_{\rm eff}(\phi, V^\mu, \mathbf{b}^\mu)$.

All possible meson interactions permitted by symmetry considerations to a given order in a power-counting scheme are included, in line with effective field theory, in $U_{\rm eff}(\phi, V^\mu, \mathbf{b}^\mu)$. In this work we employ the effective interaction of the form [3]

$$U_{\rm eff}(\phi, V^\mu, \mathbf{b}^\mu) = \frac{\kappa}{3!}(g_s\phi)^3 + \frac{\lambda}{4!}(g_s\phi)^4 - \frac{\zeta}{4!}(g_{\rm v}^2 V^\mu V_\mu)^2 - \Lambda_v(g_\rho^2 \mathbf{b}_\mu \cdot \mathbf{b}^\mu)(g_{\rm v}^2 V^\nu V_\nu), \tag{2.7}$$

where coefficients κ, λ, ζ and $\Lambda_{\rm v}$ denote four meson couplings. The first two κ and λ are coupling constants of isoscalar meson self-interaction. They were introduced by Boguta and Bodmer [59] to reduce the nuclear incompressibility coefficient of symmetric nuclear matter from a very large value predicted by QHD model [8] to one that is obtained from breathing mode energy measurements [65] mentioned earlier. The third coefficient ζ, like the first two, is also a coupling constant of isoscalar meson self-interaction responsible for the softening of equation of state (EoS) of symmetric nuclear matter, it was introduced by Muller and Serot [66], when they realized that it possible to build models with different values of ζ that reproduced the same nuclear properties at normal densities but produced maximum neutron-star masses differing by almost one solar mass. The mixed isoscalar-isovector ($\omega - \rho$) coupling $\Lambda_{\rm v}$ improves the density dependence of the symmetry energy. $\Lambda_{\rm v}$ was introduced by Horowitz and Piekarewicz [67].

We are now ready to derive the equation of motions from the Lagrangian density $\mathcal{L} = \mathcal{L}_0 + \mathcal{L}_{int}$ through the application of Euler-Lagrangian equations:

$$\frac{\partial \mathcal{L}}{\partial q} - \partial_\mu \left(\frac{\partial \mathcal{L}}{\partial(\partial_\mu q)} \right) = 0, \tag{2.8}$$

where q are generalized coordinates and denote various fields in Table 2.1. Thus, the field equations for baryons is the Dirac equation

$$\left[\gamma_\mu(i\partial^\mu - V) - (M - S)\right]\psi = 0, \tag{2.9}$$

where scalar (S) and vector (V) potentials with Lorentz character are defined as

$$V = g_{\rm v}V_\mu + g_\rho \boldsymbol{\tau} \cdot \mathbf{b}_\mu + \frac{e}{2}(1+\tau_3)A_\mu, \tag{2.10}$$

$$S = g_s\phi. \tag{2.11}$$

The field equations of the mesons and photons are the Klein-Gordon equations:

$$(\partial^\mu\partial_\mu + m_s^2)\phi = -g_s\bar{\psi}\psi - \zeta\phi^2 - \lambda\phi^3, \tag{2.12}$$

$$\partial_\nu V^{\mu\nu} + m_{\rm v}^2 V^\mu = g_{\rm v}\bar{\psi}\gamma^\mu\psi, \tag{2.13}$$

$$\partial_\nu \mathbf{b}^{\mu\nu} + m_\rho^2 \mathbf{b}^\mu = g_\rho\bar{\psi}\gamma^\mu\boldsymbol{\tau}\psi + g_\rho(\mathbf{b}^\mu \times V^{\mu\nu}), \tag{2.14}$$

$$\partial_\nu F^{\mu\nu} = e\bar{\psi}\gamma^\mu\frac{1+\tau_3}{2}\psi. \tag{2.15}$$

2.3 Relativistic Mean Field Limit

The Dirac equation Eq. (2.9), Klein-Gordon equation Eq. (2.12) and Maxwell's equations with source terms Eqs. (2.13 - 2.15) form a system of coupled, nonlinear differential equations. To solve these equations we resort to the mean field limit, i.e., Hartree approximation in which meson fields and photon field operators are replaced by their classical fields (i.e., expectation values). For a static and spherical symmetric system, the mean field approximation leads to the following:

Table 2.2: Parameter sets for the two relativistic mean field models: NL3 [2] and FSUGold [3]. The parameters κ and the $\sigma-$meson mass m_s are given in MeV. Masses of nucleon M = 939 MeV, $\omega-$meson $m_{\rm v} = 782.5$ MeV and $\rho-$meson $m_\rho = 786$ MeV are fixed in both models.

Model	$m_{\rm s}$	$g_{\rm s}^2$	$g_{\rm v}^2$	g_ρ^2	κ	λ	ζ	$\Lambda_{\rm v}$
NL3	508.194	104.3871	165.5854	79.6000	3.8599	-0.015 905	0.0000	0.0000
FSUGold	491.500	112.1996	204.5469	138.4701	1.4203	+0.023 762	0.0600	0.0300

$$\begin{aligned}
\phi \to \langle\phi\rangle &= \phi_0(\mathbf{x}), && (2.16)\\
V^\mu \to \langle V^\mu\rangle &= g^{\mu 0} V_0(\mathbf{x}), && (2.17)\\
\mathbf{b}_a^\mu \to \langle \mathbf{b}_a^\mu\rangle &= g^{\mu 0}\delta_{a3}\mathbf{b}_0(\mathbf{x}), && (2.18)\\
A^\mu \to \langle A^\mu\rangle &= g^{\mu 0} A_0(\mathbf{x}). && (2.19)
\end{aligned}$$

In a static and symmetric nucleus, current conservation ensures that the spatial components of $V^\mu, \mathbf{b}^\mu$ and A^μ have vanishing contribution to the static limit. As a result, we only consider the time-like components of the vector fields: V^0, b^0, and A^0. Furthermore, charge conservation guarantees that only the the third component($\rho_{0,3}$) of the isovector ρ^0 contributes to the interaction. Similarly, the baryon sources to which the mesons and photons couple are replaced by their expectation values in the mean-field ground state:

$$\begin{aligned}
\bar\psi(x)\psi(x) \to \langle\bar\psi(x)\psi(x)\rangle &= \rho_{\rm s}(\mathbf{x}), && (2.20)\\
\bar\psi(x)\gamma^\mu\psi(x) \to \langle\bar\psi(x)\gamma^\mu\psi(x)\rangle &= g^{\mu 0}\rho_{\rm v}(\mathbf{x}), && (2.21)\\
\bar\psi(x)\gamma^\mu\tau_i\psi(x) \to \langle\bar\psi(x)\gamma^\mu\tau_i\psi(x)\rangle &= g^{\mu 0}\delta_{i3}\rho_3(\mathbf{x}), && (2.22)\\
\bar\psi(x)\gamma^\mu\tau_p\psi(x) \to \langle\bar\psi(x)\gamma^\mu\tau_p\psi(x)\rangle &= g^{\mu 0}\rho_{\rm p}(\mathbf{x}). && (2.23)
\end{aligned}$$

Here $\rho_{\rm s}(\mathbf{x})$ denotes Lorentz scalar density, $\rho_{\rm v}$ is the baryon density and ρ_3 is the isovector density which is the difference between neutron $\rho_{\rm n}$ and proton $\rho_{\rm p}$ densities.

The nucleons satisfy the Dirac equation in the presence of mean-field potentials having Lorentz scalar and vector character:

$$[i\gamma_\mu(\partial^\mu - (M - g_{\rm s}\phi) - \gamma^0(g_{\rm v}V_0 + g_\rho\tau b_0 + \frac{e}{2}(1+\tau_3)A_0)]\psi = 0. \quad (2.24)$$

The various meson fields satisfy nonlinear and inhomogeneous Klein-Gordon equations with nuclear densities acting as their sources:

$$\begin{aligned}
\nabla^2\phi_0 - m_{\rm s}\phi_0 - \partial_{\phi_0}U_{\rm eff}(\phi_0, V_0, b_0) &= -g_{\rm s}\rho_{\rm s}, && (2.25)\\
\nabla^2 V_0 - m_{\rm v}V_0 + \partial_{V_0}U_{\rm eff}(V_0, V_0, b_0) &= -g_{\rm v}\rho_{\rm v}, && (2.26)\\
\nabla^2 b_0 - m_\rho b_0 + \partial_{b_0}U_{\rm eff}(V_0, V_0, b_0) &= -\frac{g_\rho}{2}\rho_3. && (2.27)
\end{aligned}$$

The photon field obeys the Poisson equation with the proton density as a source:

$$\nabla^2 A_0 = -e\rho_{\rm p}. \quad (2.28)$$

2.4 Rotationally Invariant Systems

For a spherically symmetric nuclear potential, the solutions to single particle Dirac equation have the form

$$\mathcal{U}_\alpha(\mathbf{x}) = \mathcal{U}(\mathbf{x})_{n\kappa mt} = \begin{pmatrix} g_{n\kappa t}(x)\mathcal{Y}_{\kappa m}(\hat{\mathbf{x}}) \\ \\ if_{n\kappa t}(x)\mathcal{Y}_{-\kappa m}(\hat{\mathbf{x}}) \end{pmatrix}, \tag{2.29}$$

where n is the principal quantum number, κ is the generalized relativistic angular momentum which uniquely specifies both the orbital l and total j angular momenta:

$$j = |k| - \frac{1}{2}, \quad l = \begin{cases} \kappa & \text{for } \kappa > 0, \\ 1-\kappa & \text{for } \kappa < 0 \end{cases}, \quad l' = 2j - l = \begin{cases} \kappa - 1 & \text{for } \kappa > 0 \\ -\kappa & \text{for } \kappa < 0 \end{cases}, \tag{2.30}$$

and m is the projection of j. The spin spherical harmonics, $\mathcal{Y}_{\pm km}(\hat{\mathbf{x}})$, which determine the angular and spin parts of the wave function are given by

$$\mathcal{Y}_{\kappa m} = \sum_{s_{z'}=\pm\frac{1}{2}} \left\langle l, \frac{1}{2}, m_l, m_s | jm \right\rangle Y_{l,m-s_{z'}}(\hat{\mathbf{x}})\chi_{s_{z'}} \ , \tag{2.31}$$

$$\mathcal{Y}_{-\kappa m} = \sum_{s_{z'}=\pm\frac{1}{2}} \left\langle l', \frac{1}{2}, m_l, m_s | jm \right\rangle Y_{l,m-s_{z'}}(\hat{\mathbf{x}})\chi_{s_{z'}} \ , \tag{2.32}$$

where the bracket $\langle\rangle$ denotes the usual Clebsch-Gordon coefficients and Y_{l,m_l} are the usual spherical harmonics of order l. The Pauli spinors $\chi_{s_{z'}}$ are

$$\chi_{s_{z'}=\frac{1}{2}} = \begin{pmatrix} 1 \\ 0 \end{pmatrix} \quad \text{and} \quad \chi_{s_{z'}=-\frac{1}{2}} = \begin{pmatrix} 0 \\ 1 \end{pmatrix}. \tag{2.33}$$

The upper and lower radial wavefunctions are denoted by $g_\alpha(x)$ and $f_\alpha(x)$, respectively. One gets two coupled differential equations of the bound nucleon radial wavefunctions upon substitution of Eq. (2.29) into Eq. (2.9):

$$\frac{\mathrm{d}}{\mathrm{d}x}g_\alpha(x) - \frac{\kappa}{x}g_\alpha(x) - [E - V_0 + M - S_0]f_\alpha(x) = 0, \tag{2.34}$$

$$\frac{\mathrm{d}}{\mathrm{d}x}f_\alpha(x) - \frac{\kappa}{x}f_\alpha(x) + [E - V_0 + M + S_0]g_\alpha(x) = 0. \tag{2.35}$$

The normalization condition is given by

$$\int_0^\infty \mathrm{d}r \left[g_\alpha^2(x) + f_\alpha^2(x)\right] = 1. \tag{2.36}$$

A system of coupled differential Eqs. (2.24 - 2.27) and (2.34 - 2.35) form what is known as relativistic Hartree equations. To obtain the numerical solution to the Hartree equations a self-consistent iterative procedure is implemented to solve the Dirac equation (2.24) with scalar and vector potentials obtained from the solutions of the Klein-Gordon equations(2.25 - 2.27). The self-consistency starts with Woods-Saxon-shaped meson fields to produce boundstate energies and corresponding wave functions for single-particle states. The scalar and vector densities calculated from these wave functions are utilised as sources for the meson and electromagnetic fields and, in turn, the meson and electromagnetic fields determine the mean-field potentials for the nucleons. The Green functions techniques are utilised to produce new meson fields. The iterative procedure continues until self-consistency is

obtained. One then obtains the ground-state properties of the nucleus of interest, such as total binding energy, single-nucleon energies, root mean square proton and neutron radii and wave functions, distribution of meson and photon fields, and density profiles. We developed a new computer program to perform the numerical calculations presented in this chapter. In appendix A we describe the program in detail. Note that we incorporated the BCS model pairing correlation for the open-shell nuclei.

The Eqs. (2.20 - 2.23) put on display the richness of treating nuclear many body problem with relativistic quantum field theory as five types of nuclear densities: scalar, pseudoscalar, vector, axial-vector and tensor emerge in a natural manner as opposed to nonrelativistic treatment where only one is observed namely the matter (vector) nuclear density. For closed shell nuclei, Eqs. (2.20 - 2.23) can be rewritten so that one obtains scalar density, vector density, isovector density and charge density:

$$\rho_{\rm s}(r) = \sum_{\alpha}^{occ} \bar{\mathcal{U}}_{\alpha}(\mathbf{x})\mathcal{U}_{\alpha}(\mathbf{x}), \tag{2.37}$$

$$\rho_{\rm v}(r) = \sum_{\alpha}^{occ} \bar{\mathcal{U}}_{\alpha}(\mathbf{x})\gamma^0\mathcal{U}_{\alpha}(\mathbf{x}), \tag{2.38}$$

$$\rho_{3}(r) = \sum_{\alpha}^{occ} \mathcal{U}^{\dagger}_{\alpha}(\mathbf{x})\tau_3\mathcal{U}_{\alpha}(\mathbf{x}), \tag{2.39}$$

$$\rho_{\rm p}(r) = \sum_{\alpha}^{occ} \mathcal{U}^{\dagger}_{\alpha}(\mathbf{x})\frac{1+\tau_3}{2}\mathcal{U}_{\alpha}(\mathbf{x}), \tag{2.40}$$

where $\mathcal{U}_{\alpha}$ is a single-particle Dirac spinor for boundstate nucleon. The summations run over all occupied single particle states.

The proton root-mean-square (rms) matter radius is given by:

$$r = [\langle r^2 \rangle]^{\frac{1}{2}} = \left[\frac{1}{Z}\int {\rm d}\tau \;\; r^2\rho_{\rm v,p}(r)\right]^{\frac{1}{2}}. \tag{2.41}$$

and charge mean-square radius is given by:

$$r = [\langle r^2_{\rm ch} \rangle]^{\frac{1}{2}} = \left[\frac{1}{Z}\int {\rm d}\tau \;\; r^2\rho_{\rm ch}(r)\right]^{\frac{1}{2}}. \tag{2.42}$$

2.5 Halo Nuclei and Skin

As the number of neutrons in a particular nucleus increases, the nuclear surface gets diffuse and nuclear density decreases. This leads to the two important phenomena of neutron halos and skins. The nuclei whose radius is significantly larger than the radius predicted by empirical radius formula $r = r_0 A^{\frac{1}{3}}$ are called neutron halo nuclei. This phenomenon emerges within light neutron-rich nuclei along or on the drip line. In neutron halo nuclei, a core of protons and neutrons can appear to be separated from other neutron matter that surrounds it in a halo-like structure. This is depicted by a long tail in the matter distribution due to the wave function of the weakly bound nucleons, i.e., halo nuclei have density distribution reaching further out than expected. ^{11}Li is the first nucleus observed experimentally that has neutron halo. Some nuclei with one neutron halo are ^{14}N, ^{11}Be, ^{19}C ^{6}He and those which have two-neutron halo ^{6}He, ^{14}Be and ^{17}B. Besides, one and two neutron halo nuclei there exists a neutron halo nucleus formed by four neutrons: ^{8}He. The trait of nuclear halo in exotic nuclei is not limited to neutron halo. There are some exotic nuclei with possible proton halo for example: ^{17}N, ^{17}F and ^{8}B. There exist halo nuclei that are not formed by nucleon such as hypertriton where Λ particle orbits around a deuterium core.

In heavy or unstable neutron-rich nuclei the excess neutrons are pushed out against the surface tension forming a neutron skin, which is defined as the difference between the neutron and proton root-mean-square radii. This phenomenon takes place when the number of neutrons increases with respect to the constant number of protons. The isospin asymmetry forces, in general, prefer uniform proton and neutron densities throughout the nucleus. However, protons become more bound with increase of the neutron number and hence, the density distribution of protons can not extend to the nucleus surface. From the macroscopic point of view, the nuclear medium of neutron-rich nuclei applies sufficient pressure to hold protons in the core of the nucleus and consequently, the surface is composed of neutron skin. Neutron skins characterize a form of nuclear matter considered to exist only in neutron stars. Some of the ideal nuclei for studying neutron skin thickness are ^{48}Ca, stable ^{208}Pb and ^{118}Sn Isotopes. They are stable, neutron-rich doubly magic nuclei. These properties are essential in ensuring that theoretical and experimental uncertainties are minimal in extracting neutron thickness.

Chapter 3

RELATIVISTIC PLANE WAVE MODEL

3.1 Introduction

Proton knock-out, and in particular exclusive $(p, 2p)$ reactions, in direct kinematics (*see* Fig. 3.1) with stable beams has proven to be an essential device to study the single-particle properties of nuclei and the nucleon-nucleon NN interaction in a nuclear medium along the beta stability valley. In direct kinematics, an incident proton beam ejects a bound proton from the target nucleus. In the medium energy regime the probability for nucleon-nucleon collisions (multi-scattering) within the nuclear field is expected to be significantly reduced and the interaction is assumed to be dominated by single-collision processes, i.e., a quasifree[1]collision between the incident proton and the bound proton. As stated in chapter 1, the proton $(p, 2p)$ knockout scattering reaction is essentially a nucleon-nucleon interaction which consists of two primary applications; (1) as a mechanism to study the single particle properties of a target nucleus and (2) as a tool to investigate in-medium nucleon-nucleon NN interactions.

The availability of high-energy radioactive beams allows in principle to utilise the method of $(p, 2p)$ knockout scattering in inverse kinematics with hydrogen targets. The knockout reactions that occur in inverse kinematics are expected to play a crucial role in investigating the structures of those unstable nuclei, with the evaluation of these reactions serving as a spectroscopic tool. It is expected that in future $(p, 2p)$ knockout reactions will be performed with unstable nuclear beams and polarized proton target. With polarized beams both nuclear structure and the nature of strong NN interaction in nuclear matter of such nuclei will be able to be studied. Because the process involves NN scattering in the nuclear field, quasifree scattering provides a direct mechanism to investigate the NN interaction inside the nuclear medium. At the kinematical conditions considered in this work it is expected that nuclear distortion effects on the scattered protons will become negligible. Hence, the plane wave model should be sufficient for study of complete set of spin-transfer observables.

The use of relativistic plane wave models to study polarization transfer observables has contributed an immense qualitative and quantitative information regarding the nature of strong NN interaction in the nuclear field. In the study of quasielastic (p, p') with RPWIA model[68, 69, 70], it was observed that the use of relativistic models lead to a phenomenon of the quenching of analyzing power relative to values of free NN scattering. Quenching effect is when values calculated with relativistic models

[1]This means we can consider the collision of the projectile and the struck nucleon as "free" and the residual nucleus as a spectator in the reaction.

appear to be suppressed relative to the corresponding free NN scattering values. Since the quenching of analysing of power does not emerge in the nonrelativistic models, it was interpreted as the relativistic signature. The quenching effect of analyzing power seen as the evidence of nuclear medium effects[]. However, in Ref [71, 72] it was shown the quenching of analysing power may be due to the use IA1 representation of NN interaction. The reduction of analyzing power relative to free proton-proton scattering values is also observed in exclusive $(p, 2p)$ knockout reactions[73, 74]. In Ref [28] it was shown that that density-dependent corrections to meson-nucleon coupling constants and meson masses have the effect of suppressing the analyzing power and other spin transfer observables. RPWIA has also been used to study the sensitivity of exclusive proton knockout spin observables to different Lorentz invariant representations of the NN interaction [75]. In Ref[76], the influence of effective masses on spin transfer observables of the exclusive $(p, 2p)$ was studied extensively within relativistic plane wave impulse approximation (RPWIA).

It has been shown that polarization transfer observables provide information regarding the modification of the free nucleon-nucleon (NN) interaction by the surrounding nuclear medium in the intermediate energy region [77, 78]. This implies that nucleon-nucleon interactions in free space can be realized by polarization transfer observables. The polarization transfer observables permit us to study the influence of the surrounding nuclear medium on the free NN interaction. Since the plane wave models provided good description of the spin transfer observables it was reasoned that they are insensitive to distortions. The hand-waving argument insisted that since polarization transfer observables are effectively the ratios of linear combinations of spin-dependent cross sections the effects of distortions largely cancel out. However, it was shown in Ref [78] in the study of exclusive $(p, 2p)$ reaction that this argument is only sufficient for certain kinematical conditions such as zero recoil momentum. In this work our use of RPWIA model motivated by the fact that this model has proven to be an effective probe of sensitivity of nuclear medium-modifications. Furthermore, since this is the first study to describe polarization transfer observables with the inverse kinematics RPWIA should be adequate to give initial feel of the behaviour of the spin transfer observables. By using RPWIA model with the NN amplitudes represented by five-term Lorentz invariant parametrization of the NN scattering matrix, we avoid complications associated with relativistic distorted wave impulse approximation and IA2. A plane wave model should provide a reasonable description of the scattering observables at intimidate energies. Exclusive $(p, 2p)$ scattering is an ideal tool to investigate medium modifications of the NN interaction [77, 28]. The suppression of analyzing power is not limited to quasielatic data, it was also observed in the study of exclusive $(p, 2p)$ scattering reaction [74].

In this chapter we exploit the features of $(p, 2p)$ scattering in order to employ a relativistic plane wave impulse approximation (RPWIA) for the task of studying nucleon-nucleon interaction in the nuclear medium of selected oxygen isotopes. It will be interesting to see how polarization observables vary within a particular isotopic chain. The variation or evolution of polarization observables will allow us to study the nuclear medium modification in oxygen isotope as neutron number increases. The isotopes will be investigated with both direct and indirect scattering reactions, however, as a first step the theoretical formalism below is provided in terms of direct kinematics. Direct kinematics are intuitive and will make transition into indirect kinematics more convenient. The use of direct kinematics will permit us to perform numerical checks and compare our results with the previous works. By direct kinematics we mean that the nucleus of interest serves as a target and in the indirect (inverse) kinematics unstable isotope serves as a projectile and the stationary proton is placed as a target. The core assumption of relativistic plane wave impulse approximation remains that the $(p, 2p)$ knockout reaction is a two-body scattering process (i.e., for direct kinematics proton-nucleus interaction and for inverse kinematics nucleus-proton interaction).

There exist two parametrizations of the scattering operator $\hat{F}$ namely IA1 [15, 16] representation of $\hat{F}$ and IA2 [79, 80] representation of $\hat{F}$. In IA1 representation $\hat{F}$ is parametrized in terms of five Fermi (scalar, pseudo-scalar, vector, axial-vector, and tensor) invariant amplitudes and the

experimental data completely specify $\hat{F}$. There exists a large number of SPVAT parametrizations of NN scattering matrix models; the most successfully include McNeil-Ray-Wallace parametrization [15, 16], Goldburger-Nambu- Öehme GNO invariants [81] and perturbative invariants [82]. However, these models suffer from a plenty of ambiguities inherent in most IA1 representations such as failure to distinguish between pseudoscalar and pseudovector pion-nucleon coupling. In addition, the aforementioned models do not provide adequate explanation for the exchange behaviour of the NN amplitudes in the nuclear medium [83, 84]. The IA1 model which addresses these shortcomings is called relativistic Horowitz-Love-Franey (HLF) model wherein the amplitudes are parametrized in terms of Yukawa-type meson exchanges. HLF model extends the positive energy scattering data to the full Dirac space of two particles thereby prescribing the negative energy matrix elements [85]. In this model the direct and exchange terms are evaluated explicitly, consequently, allowing one to investigate direct and exchange contributions separately.

In the present study a target nucleus is modelled as a Fermi gas in the context of relativistic mean field theory. Furthermore, RPWIA implicitly takes into account the effect of external nucleon via the inclusion of constant effective masses within Dirac plane wave spinors. This is a realistic treatment of scattering process since the collision occurs within a nuclear medium. The RPWIA model we present is expected to provide a reasonable approximation of spin transfer observables since at the momentum transfers and excitation energies of interest initial and final distortion effects to be minimum. The details of the nuclear structure of the nuclei of interest are incorporated via the the boundstate wavefunction which is calculated in relativistic mean field theory. Section 2.4 illustrates the features of the radial boundstate is computed within the context of the RMF theory. In our model we use FSUGold parameter set.

This chapter presents the theoretical formalism for the computation of spin transfer observables with direct and inverse kinematics within the context of relativistic plane wave model. In section 3.2 we will develop a relativistic plane wave framework that will allow us to compute spin observables for the exclusive $(p, 2p)$ reaction in direct and inverse kinematics. In section 3.3 we compute the spin observables and the NN interaction is given by IA1 representation. We also present a flowchart diagram in Fig. 3.3 for the Python programming language code that that was written to compute numerical values of the spin transfer observables.

3.2 Theoretical Formalism

Here we present and discuss the formulation of the relativistic plane wave model. We use it to analyse exclusive $(p, 2p)$ reactions performed with direct and indirect kinematics. Fig. 3.1 displays the schematic view for coplanar geometry of the $A(a, a'b')C$ reaction in the laboratory frame. Here the notation $A(a, a'b')C$ represents the exclusive $(p, 2p)$ reaction where an incident proton a interacts and knocks out a bound proton b from a specific orbital in the target nucleus A generating a one-hole state, resulting in three particles in the final state, namely, the recoil residual nucleus C and two outgoing protons a' and b' which are detected in coincidence at coplanar laboratory scattering angles (on opposite sides of the incident beam) $\theta_{a'}$ and $\theta_{b'}$, respectively. Note that the probability for a proton knockout reaction described above to occur is related to the triple differential cross section [24, 77]:

$$\frac{d^3\sigma}{dE_a d\Omega_a d\Omega_b} = \frac{F_{kin}}{(2s_a+1)(2J_b+1)} S_{L_b J_b} \sum_{\gamma} |T_{LJM_J}(s_a, s_{a'}, s_{b'})|^2. \tag{3.1}$$

A spectroscopic factor $S_{L_b J_b}$ gives the probability that a proton is found in an orbital specified by the orbital angular momentum and total angular momentum quantum numbers. In the above expression F_{kin} is a kinematical factor defined as

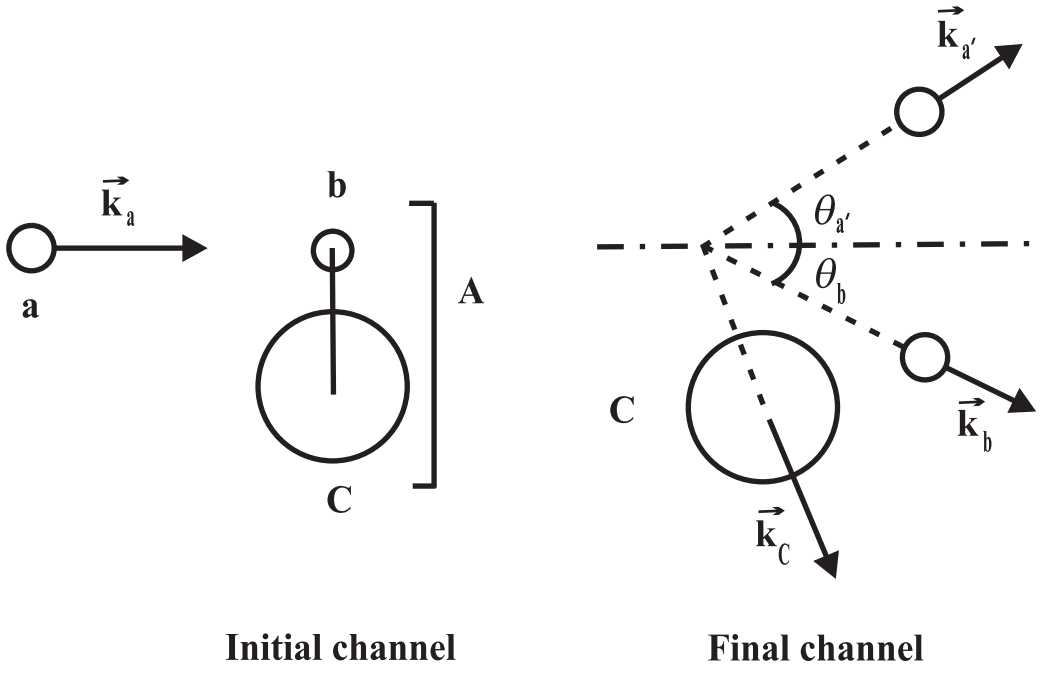

Figure 3.1: Schematic representation for proton knockout reaction $(p, 2p)$ in the lab frame.

$$F_{kin} = \frac{E_a E_{a'} E_{b'}}{(2\pi)^5} \frac{k_{a'} k_{b'}}{k_a} \left[1 + \frac{E_{b'}}{E_C} \left(1 - \frac{k_a}{k_{b'}} \cos\theta_{b'} + \frac{k_{a'}}{k_b} \cos(\theta_{a'} + \theta_{b'}) \right) \right]^{-1}, \tag{3.2}$$

where E_i and k_i denote the total energies and momenta of incident proton a, two outgoing protons a' and b', and the residual nucleus C. The summation γ of the transition matrix $T_{LJM_J}(s_a, s_{a'}, s_{b'})$ in Eq. (3.1) is taken over all spin components $s_a, s_{a'}$ and $s_{b'}$ in initial and final states.

The most significant quantity that has to be computed in order to calculate the spin observables of interest is the invariant transition matrix element which is given by:

$$T \quad = \quad \langle f|\hat{F}|i\rangle, \tag{3.3}$$

where $|i\rangle$ and $|f\rangle$ are the initial and final nuclear states of scattering process, respectively, and $\hat{F}$ is the NN scattering operator. In this chapter, the scattering operator $\hat{F}$ is parametrized in terms of five Fermi covariants, the so-called SPVAT form or the original relativistic impulse approximation (IA1) representation of $\hat{F}$. It is defined as follows:

$$\hat{F} = \sum_{L=S}^{T} F_L(\lambda^L \otimes \lambda_L), \tag{3.4}$$

where $\lambda^L \in \{I_4, \gamma^5, \gamma^\mu, \gamma^5\gamma^\mu, \sigma^{\mu\nu}\}$, with $L = S, P, V, A, T$ and F_L is a complex NN amplitude. The symbol $\otimes$ is the Kronecker product. In this work for the IA1 calculations we use the amplitudes of Ref. [86].

We now consider Fig. 3.2, in order to compute the invariant matrix element for exclusive $(p, 2p)$ keeping in mind that RPWIA considers this reaction to be single-step process wherein the incident proton interacts only with one target nucleon in the orbit with specific quantum numbers inside the

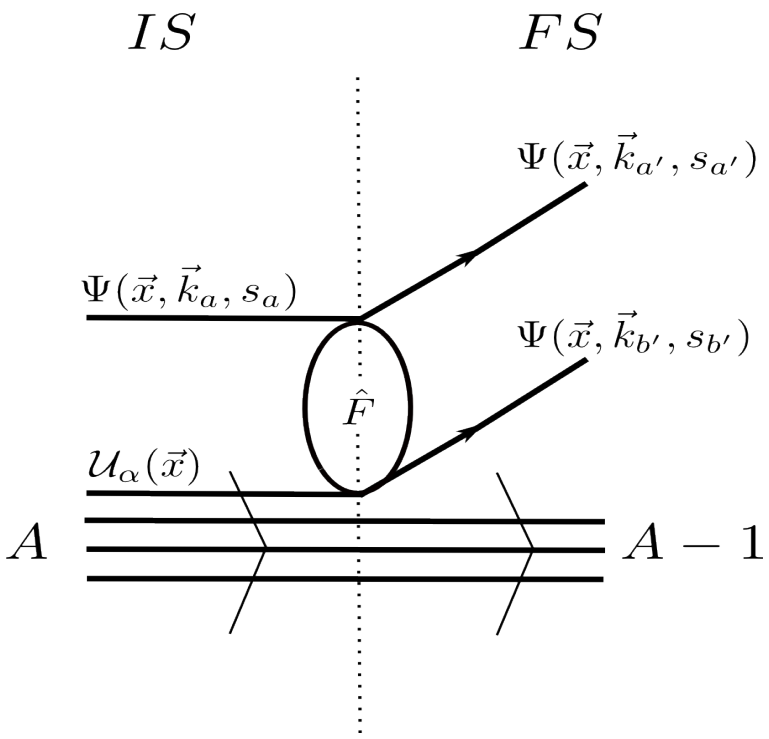

Figure 3.2: The Feynman-like diagram for the representation of proton knockout reaction $(p, 2p)$. The IS stands for the initial nuclear state and FS for final nuclear state of the scattering reaction. The scattered and the outgoing proton are detected in coincidence, while the residual nucleus remains inert.

nucleus. Thus, the RPWIA reduces the process to a two-body scattering process wherein the initial state is given by:

$$|i\rangle = |i_1\rangle \otimes |i_2\rangle = \psi^{(+)}(\vec{x}, \vec{k}_a, s_a) \otimes \mathcal{U}_{LJM_J}(\vec{x}), \tag{3.5}$$

and the final state is given by

$$|f\rangle = |f_1\rangle \otimes |f_2\rangle = \bar{\psi}^{(-)}(\vec{x}, \vec{k}_{a'}, s_{a'}) \otimes \bar{\psi}^{(-)}(\vec{x}, \vec{k}_{b'}, s_{b'}). \tag{3.6}$$

With these assumptions, we now impose the zero range approximation on the NN interaction and Eq. (3.3) becomes:

$$T_{LJM_J}(s_a, s_{a'}, s_{b'}) = \int d^3\vec{x}[\bar{\psi}^{(-)}(\vec{x}, \vec{k}_{a'}, s_{a'}) \otimes \bar{\psi}^{(-)}(\vec{x}, \vec{k}_{b'}, s_{b'})]\hat{F}[\psi^{(+)}(\vec{x}, \vec{k}_a, s_a) \otimes \mathcal{U}_{LJM_J}(\vec{x})], \tag{3.7}$$

The four-component scattering wave functions $\psi(\vec{x}, \vec{k}_i, s_i)$ are solutions to the fixed-energy Dirac scattering equations. Thus, the scattering solutions to the free Dirac equation are given by:

$$\Psi^{(+)}(\vec{x}, \vec{k}_a, s_a) = e^{i\vec{k}_a \cdot \vec{x}} U(\vec{k}_a, s_a), \tag{3.8a}$$

$$\bar{\Psi}^{(-)}(\vec{x}, \vec{k}_{a'}, s_{a'}) = e^{-i\vec{k}_{a'} \cdot \vec{x}} U(\vec{k}_{a'}, s_{a'}), \tag{3.8b}$$

$$\bar{\Psi}^{(-)}(\vec{x}, \vec{k}_{b'}, s_{b'}) = e^{-i\vec{k}_{b'} \cdot \vec{x}} U(\vec{k}_{b'}, s_{b'}), \tag{3.8c}$$

where,

- $\psi^{(+)}(\vec{x}, \vec{k}_a, s_a)$ is the relativistic scattering wave function for particle a with outgoing boundary conditions indicated by the superscript $(-)$, where $\vec{k}_a$ is the momentum of particle a in the laboratory frame, and s_a is the spin projection thereof with respect to $\vec{k}_a$ as the $\hat{z}$-quantization axis.
- $\bar{\psi}^{(-)}(\vec{x}, \vec{k}_{a'}, s_{a'})$ is the relativistic distorted wave function of the projectile a' with incoming boundary conditions where $\vec{k}_{a'}$ is the momentum of particle a in the laboratory frame, and $s_{a'}$ is the spin projection thereof with respect to $\vec{k}'_a$ as the $\hat{z}$-quantization axis.
- $\bar{\psi}^{(-)}(\vec{x}, \vec{k}_{b'}, s_{b'})$ is the adjoint relativistic scattering wave function for particle b' with incoming boundary conditions indicated by the superscript $(-)$, where $k_{b'}$ is the momentum of particle b' in the laboratory frame, and $s_{b'}$ is the spin projection thereof with respect to $\vec{k}_{b'}$ as the $\hat{z}$-quantization axis.
- $\mathcal{U}_{LJM_J}(\vec{x})$ is a boundstate wavefunction for the target proton and labelled with single-particle quantum numbers L, J and M_J. *See* chapter 2 on how it is computed.

The Dirac spinor is defined as

$$U(\vec{k}_i, s_i) = \left[\frac{E_i + m_i}{2m_i}\right]^{\frac{1}{2}} \begin{pmatrix} \chi_s \\ \dfrac{\vec{\sigma} \cdot \vec{k}_i}{E_i + m_i}\chi_s \end{pmatrix} \tag{3.9}$$

where m_i and $\vec{k}_i$ refers to the rest mass and momentum of particle $i \in (a, a', b')$ with energy $E_i = \sqrt{k_i^2 + m_i^2}$. We assume that the $x-z$ is the scattering plane and the particle with the momentum

$\vec{k}$ makes scattering angle θ_{lab} with the plane. Hence, we can compute quantity $\vec{\sigma}\cdot\vec{k}$ of Eq. (3.9) as follows

$$\begin{aligned}\vec{\sigma}\cdot\vec{k} &= \sigma_1 k_x + \sigma_2 k_y + \sigma_1 k_z, &(3.10)\\ &= k\sin\theta_{lab}\sigma_1 + k\cos\theta_{lab}\sigma_3, &(3.11)\\ &= k\begin{bmatrix}\cos\theta_{lab} & \sin\theta_{lab}\\ \sin\theta_{lab} & -\cos\theta_{lab}\end{bmatrix}. &(3.12)\end{aligned}$$

The normalization condition for the free Dirac spinors is

$$\bar{U}(\vec{k}_i, s_i)U(\vec{k}_i, s_i) = 1. \tag{3.13}$$

The Pauli spinor χ_s for projection $s = \pm\frac{1}{2}$ along an arbitrary quantization axis (i) in the rest frame of the nucleon is defined as

$$\chi_s = \sum_{s_z}\mathcal{D}^{(1/2)}_{s_z s}(\alpha,\beta,\gamma)\chi_{s_z} = \sum_{s_z}\mathcal{D}^{(1/2)}_{s_z s}(i)\chi_{s_z}, \tag{3.14}$$

in which $\mathcal{D}^{(1/2)}_{s_z s}(\alpha,\beta,\gamma)$ is a Wigner D-function written in terms of the rotation (Euler) angles $(\alpha,\beta$ and $\gamma)$ of the quantization axis with respect to the $\hat{z}$-axis. The base spin vectors for the quantization axis along the $\hat{z}$-axis are:

for spin-up

$$\chi_{s_z=1/2} = \begin{pmatrix}1\\0\end{pmatrix}, \tag{3.15}$$

and spin down

$$\chi_{s_z=-1/2} = \begin{pmatrix}0\\1\end{pmatrix}. \tag{3.16}$$

The polarized two-component spinor is expanded in terms of the base spin vectors of Eqs. (3.15) and (3.16) as follows

$$\chi_s = \chi_{s_z=+1/2} + \chi_{s_z=-1/2}. \tag{3.17}$$

One performs Wigner-D transformation on χ_s in order to get the orientation of the spin polarization. To do this, we define the longitudinal, sideways and normal polarization directions $\hat{l}$, $\hat{s}$ and $\hat{n}$, respectively. Finally, the Wigner-D function is a 2×2 matrix, given by

$$\begin{aligned}\mathcal{D}^{(1/2)}(\alpha,\beta,\gamma) &= \exp(\frac{i\sigma_3\alpha}{2})\exp(\frac{i\sigma_2\beta}{2})\exp(\frac{i\sigma_3\gamma}{2}), &(3.18)\\ &= \begin{bmatrix} e^{-i(\alpha+\gamma)/2}\cos\frac{\beta}{2} & -e^{-i(\alpha-\gamma)/2}\sin\frac{\beta}{2}\\ e^{i(\alpha-\gamma)/2}\sin\frac{\beta}{2} & e^{i(\alpha+\gamma)/2}\cos\frac{\beta}{2}\end{bmatrix}. &(3.19)\end{aligned}$$

The quantization axis $\hat{i}$ denotes the spin polarizations $\hat{l}$, $\hat{s}$ and $\hat{n}$. It is assumed that a particle is scattered along the $x-z$ plane with scattering angle θ_{lab} relative to the z-axis. Therefore, these polarizations are related to the Euler angles used in Eq. (3.19) as follows:

$$\hat{l} \quad : \qquad \alpha = 0, \quad \beta = \theta_{lab}, \qquad \gamma = 0, \tag{3.20}$$

$$\hat{s} \quad : \qquad \alpha = 0, \quad \beta = \theta_{lab} + \frac{\pi}{2}, \quad \gamma = 0, \tag{3.21}$$

$$\hat{n} \quad : \qquad \alpha = \frac{\pi}{2}, \quad \beta = \frac{\pi}{2}, \qquad \gamma = 0. \tag{3.22}$$

Following the substitution of Eqs. (3.20 - 3.22) into Eq. (3.19), we obtain

$$\mathcal{D}^{(1/2)}(\hat{l}) = \begin{bmatrix} \cos\frac{\theta_{lab}}{2} & -\sin\frac{\theta_{lab}}{2} \\ \sin\frac{\theta_{lab}}{2} & \cos\frac{\theta_{lab}}{2} \end{bmatrix}, \tag{3.23}$$

$$\mathcal{D}^{(1/2)}(\hat{s}) = \begin{bmatrix} \frac{1}{\sqrt{2}}(\cos\frac{\theta_{lab}}{2} - \sin\frac{\theta_{lab}}{2}) & \frac{1}{\sqrt{2}}(\sin\frac{\theta_{lab}}{2} + \cos\frac{\theta_{lab}}{2}) \\ \frac{1}{\sqrt{2}}(\sin\frac{\theta_{lab}}{2} + \cos\frac{\theta_{lab}}{2}) & \frac{1}{\sqrt{2}}(\cos\frac{\theta_{lab}}{2} - \sin\frac{\theta_{lab}}{2}) \end{bmatrix}, \tag{3.24}$$

$$\mathcal{D}^{(1/2)}(\hat{n}) = \begin{bmatrix} \frac{1-i}{2} & -\frac{1-i}{2} \\ \frac{1+i}{2} & \frac{1+i}{2} \end{bmatrix}. \tag{3.25}$$

We substitute the Eqs. (3.8) and (3.4) into Eq. (3.7) to obtain:

$$T(s_a, s_{a'}, s_{b'}) = \int d^3\vec{x}[e^{-i\vec{k}_{a'}\cdot\vec{x}}\bar{U}(\vec{k}_{a'}, s_{a'}) \otimes e^{-i\vec{k}_{b'}\cdot\vec{x}}\bar{U}(\vec{k}_{b'}, s_{b'})]\hat{F}[e^{-i\vec{k}_{b'}\cdot\vec{x}}U(\vec{k}_a, s_a) \otimes \mathcal{U}_{LJM_J}(\vec{x})]. \tag{3.26}$$

After rearranging the terms in the above expression one gets

$$T(s_a, s_{a'}, s_{b'}) = [\bar{U}(\vec{k}_{a'}, s_{a'}) \otimes \bar{U}(\vec{k}_{b'}, s_{b'})]\hat{F}[U(\vec{k}_a, s_a) \otimes \int d^3\vec{x}e^{i(\vec{k}_a\cdot\vec{x} - \vec{k}_{a'}\cdot\vec{x} - \vec{k}_{b'}\cdot\vec{x})}\mathcal{U}_{LJM_J}(\vec{x})], \tag{3.27}$$

$$\int d^3\vec{x}e^{-i\vec{K}\cdot\vec{x}}\mathcal{U}_{LJM_J}(\vec{x}) = \mathcal{U}_{LJM_J}(\vec{K}), \tag{3.28}$$

$$T(s_a, s_{a'}, s_{b'}) = \sum_{L=S}^{T} F_L[\bar{U}(\vec{k}_{a'}, s_{a'}) \otimes \bar{U}(\vec{k}_{b'}, s_{b'})](\lambda^L \otimes \lambda_L)[U(\vec{k}_a, s_a) \otimes \mathcal{U}_{LJM_J}(\vec{K})]. \tag{3.29}$$

In arriving at Eq. (3.29), we substituted Eq. (3.4) into Eq. (3.27) where we took advantage of the fact that the recoil momentum of residual nucleus is given by $\vec{k}_C = -\vec{K} = \vec{k}_a - \vec{k}_{a'} - \vec{k}_{b'}$, in order to perform Fourier transform of the relativistic bound-state wave function as illustrated by Eq. (3.28). Thus, the coordinate space boundstate wave function in chapter 2 can now be presented in momentum space as:

$$\mathcal{U}_{LJM_J}(\vec{K}) = \mathcal{U}_{LJM_J}(-k_C) = \begin{pmatrix} 4\pi i^L \mathcal{Y}_{LJM_J}(\theta_{k_C}, \phi_{k_C}) g_{LJ}(k_C) \\ \\ 4\pi i^{2J-L+1} \mathcal{Y}_{2J-L+1,JM_J}(\theta_{k_C}, \phi_{k_C}) f_{2J-L,J}(k_C) \end{pmatrix} \tag{3.30}$$

with the Fourier transforms of the radial wave functions as

$$g_{LJ}(k_C) = \int_0^\infty dx \;\; x \;\; j_L(k_C x) g_{LJ}(x), \tag{3.31}$$

$$f_{2J-L,J}(k_C) = \int_0^\infty dx \;\; x \;\; j_{2J-L}(k_C x) f_{LJ}(x). \tag{3.32}$$

Note that the $j_L(k_C x)$ are the usual spherical Bessel function of order L and the angular spin spherical harmonics are defined as

$$\mathcal{Y}_{LJm}(\theta,\phi) = \sum_{s_{z'}=\pm 1/2} \left\langle l, \frac{1}{2}, m - s_{z'}, s_{z'} | jm \right\rangle Y_{L,m-s_{z'}}(\theta,\phi)\chi_{s_z}. \tag{3.33}$$

In the spirit of RPWIA, the Eq. (3.29) may now be interpreted as the transition matrix element for a two-body scattering process in which the initial proton is bound. We apply the following property of matrices on Eq. (3.29):

$$(A \otimes B)(C \otimes D) = (AC) \otimes (BD) \tag{3.34}$$

to get

$$T = \sum_{L=S}^{T} F_L [\bar{U}(\vec{k}_{a'}, s_{a'})(\lambda^L) U(\vec{k}_a, s_a)][\bar{U}(\vec{k}_{b'}, s_{b'})(\lambda_L)(\mathcal{U}_{LJM_J}(\vec{K})]. \tag{3.35}$$

On taking the complex conjugate of Eq. (3.35) and using the following properties of matrices

$$(AB)^* = B^* A^*$$

and

$$[\bar{X}AY]^* = [\bar{X}AY]^\dagger = [\bar{Y}\bar{A}X],$$

one gets:

$$T^* = \sum_{L'=S}^{T} F^*_{L'} [\bar{\mathcal{U}}_{LJM_J}(\vec{K})(\bar{\lambda}_{L'}) U(\vec{k}_{b'}, s_{b'})][\bar{U}(\vec{k}_{a'}, s_{a'})(\bar{\lambda}^{L'}) U(\vec{k}_{a'}, s_{a'})]. \tag{3.36}$$

The product of Eqs. (3.35) and (3.36) is equal to $|T(s_a, s_{a'}, s_{b'})|^2$ which is a quantity that is needed to compute a triple differential cross section in Eq. (3.1):

$$\begin{aligned} |T(s_a, s_{a'}, s_{b'})|^2 = \sum_{L,L'=S}^{T} & F_L F^*_{L'} [\bar{U}(\vec{k}_{a'}, s_{a'})(\lambda^L) U(\vec{k}_a, s_a)][\bar{U}(\vec{k}_{b'}, s_{b'})(\lambda_L)(\mathcal{U}_{LJM_J}(\vec{K})] \\ & [\bar{\mathcal{U}}_{LJM_J}(\vec{K})(\bar{\lambda}_{L'}) U(\vec{k}_{b'}, s_{b'})][\bar{U}(\vec{k}_b, s_b)(\bar{\lambda}^{L'}) U(\vec{k}_a, s_a)]. \end{aligned} \tag{3.37}$$

Appendix C illustrates how (3.37) can be obtained using trace technique. Recall that the main reason for this development is to compute the polarization transfer observables for exclusive $(p, 2p)$ nuclear scattering reaction which are defined as ratios of linear combinations of polarized triple differential cross sections for different orientations of spin projections consistent with time reversal, parity and rotational invariance. In order to simulate a polarized $(p, 2p)$ experiment, the spin projections of

incident proton a and the scattered proton a' are fixed. The spin projections of boundstate proton b and outgoing proton b' are left unfixed. Thus, the polarized triple differential cross section is obtained by setting $\gamma = s_{b'}, M_b$ in Eq. (3.1). That is the desired form $|T(s_a, s_{a'}, s_{b'})|^2$ is obtained by summing over the spin projections of b and b' meanwhile keeping the spin projections of the particles, a and a' fixed. For the bound proton summation is taken over all possible spin projections which a proton in a state with total orbital angular momentum of J_b can have. We sum over the total angular momentum projection M_b and the spin projection $s_{b'}$. Explicitly, the desired form of $|T(s_a, s_{a'}, s_{b'})|^2$ is shown below and it is evaluated directly using the free Dirac spinor Eq. (3.9) and the boundstate wavefunction Eq. (3.30).

$$\sum_{M_b, s_{b'}} |T(s_a, s_{a'}, s_{b'}|^2 = \sum_{LL'=S}^{T} \sum_{M_b, s_{b'}} F_L F^*_{L'} [\bar{U}(\vec{k}_{a'}, s_{a'})(\lambda^L) U(\vec{k}_a, s_a)][\bar{U}(\vec{k}_{b'}, s_{b'})(\lambda_L)(\mathcal{U}_{LJM_J}(\vec{K})] \\ [\bar{\mathcal{U}}_{LJM_J}(\vec{K})(\bar{\lambda}_{L'}) U(\vec{k}_{b'}, s_{b'})][\bar{U}(\vec{k}_a, s_a)(\bar{\lambda}^{L'}) U(\vec{k}_{a'}, s_{a'})] \tag{3.38}$$

3.3 Spin Observables

In the preceding section we derived the expression for the square of transition amplitude which is a key component for the computation of the exclusive $(p, 2p)$ spin observables. Here we look at how to calculate a complete set of polarization observables in the laboratory frame, that is, the analyzing power A_y, induced polarization P, and polarization transfer coefficients $D_{i'j}$. This will permit us to study nature of NN interaction in the nuclear medium. This assertion is motivated by the fact that experimental data on spin observables suggest that quasielastic and exclusive $(p, 2p)$ scattering approximately simulates NN scattering in the nuclear medium. Thus, spin observables allow one to study medium modification of NN interaction. The effect of medium modification on spin observables can be established if P, A_y or $D_{i'j}$ for exclusive $(p, 2p)$ scattering are different from the corresponding values for free NN scattering. The other observables that can be computed for the exclusive $(\vec{p}, 2\vec{p})$ are unpolarized and polarized triple differential cross sections. To obtain the former the summation γ in Eq. (3.1) is taken over the spin of the incident proton a, the spin projection of the projectile a, the two outgoing particles a' and b', and the total angular momentum projection of the bound particle b, respectively. The latter is obtained by summing γ in Eq. (3.1) over spin projection of the outgoing particle b' and the total angular momentum projection of the bound particle b, respectively.

The NN interaction is dependent on the spin orientations of the interacting particles. Therefore, with the use of polarized beams, polarization transfer observables can be determined in the laboratory frame. The polarization experiments utilise an incident proton beam polarized in an arbitrary orientation to determine the components of the polarization of the scattered protons. The initial and final laboratory coordinate frames are defined in terms of the initial (k) and final (k') momenta in the laboratory frame. The unit vectors are defined as:

$$\hat{s} = \frac{\hat{n} \times \hat{l}}{|\hat{n} \times \hat{l}|} \tag{3.39}$$

$$\hat{n} = \frac{\hat{k}_a \times \hat{k}_{a'}}{|\hat{k}_a \times \hat{k}_{a'}|} \tag{3.40}$$

$$\hat{l} = \frac{\vec{k}_a}{|\vec{k}_a|} \tag{3.41}$$

$$\hat{s}' = \frac{\hat{n} \times \hat{l}'}{|\hat{n} \times \hat{l}'|} \tag{3.42}$$

$$\hat{n}' = \hat{n} \tag{3.43}$$

$$\hat{l}' = \frac{\vec{k}_a}{|\vec{k}_a|}. \tag{3.44}$$

The complete sets of nucleon-nucleon (NN) spin transfer observables is denoted by $D_{i'j}$ ($i' = s', n', l', j = s, n, l$) where $j(i')$ is the initial (final) polarization direction. The polarization transfer observables are defined as

$$D_{i'j} = \frac{\sum_{M_{J_b s_b}} \mathrm{Tr}(T \sigma_j T^\dagger \sigma_{i'})}{\sum_{M_{J_b s_b}} \mathrm{Tr}(T T^\dagger)} \tag{3.45}$$

where D_{0n} denotes the induced polarization, P, which is the polarization that results from the scattering of an unpolarized beam from an unpolarized target. D_{n0} refers to the analyzing power, A_y, which is the ratio of initially polarized beam (nucleons) left unpolarized after interacting with the target nucleus. The remaining polarization observables, which are also constrained by parity, charge invariance and time reversal symmetry are D_{nn}, $D_{s's}$, $D_{l'l}$, $D_{s'l}$ and $D_{l's}$. In Eq. (3.45), the symbols σ_i and σ_j refer to the 2×2 Pauli spin matrix and T refers to the 2×2 matrix which is given by

$$T = \begin{pmatrix} T_{LJ}^{s_a=\frac{1}{2}, s_{a'}=\frac{1}{2}} & T_{LJ}^{s_a=-\frac{1}{2}, s_{a'}=+\frac{1}{2}} \\ T_{LJ}^{s_a=-\frac{1}{2}, s_{a'}=+\frac{1}{2}} & T_{LJ}^{s_a=-\frac{1}{2}, s_{a'}=-\frac{1}{2}} \end{pmatrix}. \tag{3.46}$$

where s_a and $s_{a'}$ refer to the spin projections of particles a and a' along the $\hat{z}$ and $\hat{z}'$ axes, defined in Eqs. (3.39 - 3.41) and Eqs. (3.42 - 3.44), respectively.

We have now succeeded in deriving the expression for spin transfer observable (*see* Eq. (3.45)) in order to turn the mathematical equations to numbers we wrote a python code `Spinorbs`. The flow diagram illustrating how `Spinorbs` computes spin transfer is in Fig. 3.3.All kinematic quantities in the RPWIA formalism are completely specified from the following input parameters, namely

- the laboratory kinetic energy T_a of the projectile proton
- the laboratory scattering angles ($\theta_{a'}$ and $\theta_{b'}$) of two outgoing protons
- the nucleon mass m
- the mass of the target nucleus m_A
- the upper $g(r)$ and lower $f(r)$ components of boundstate wavefunction

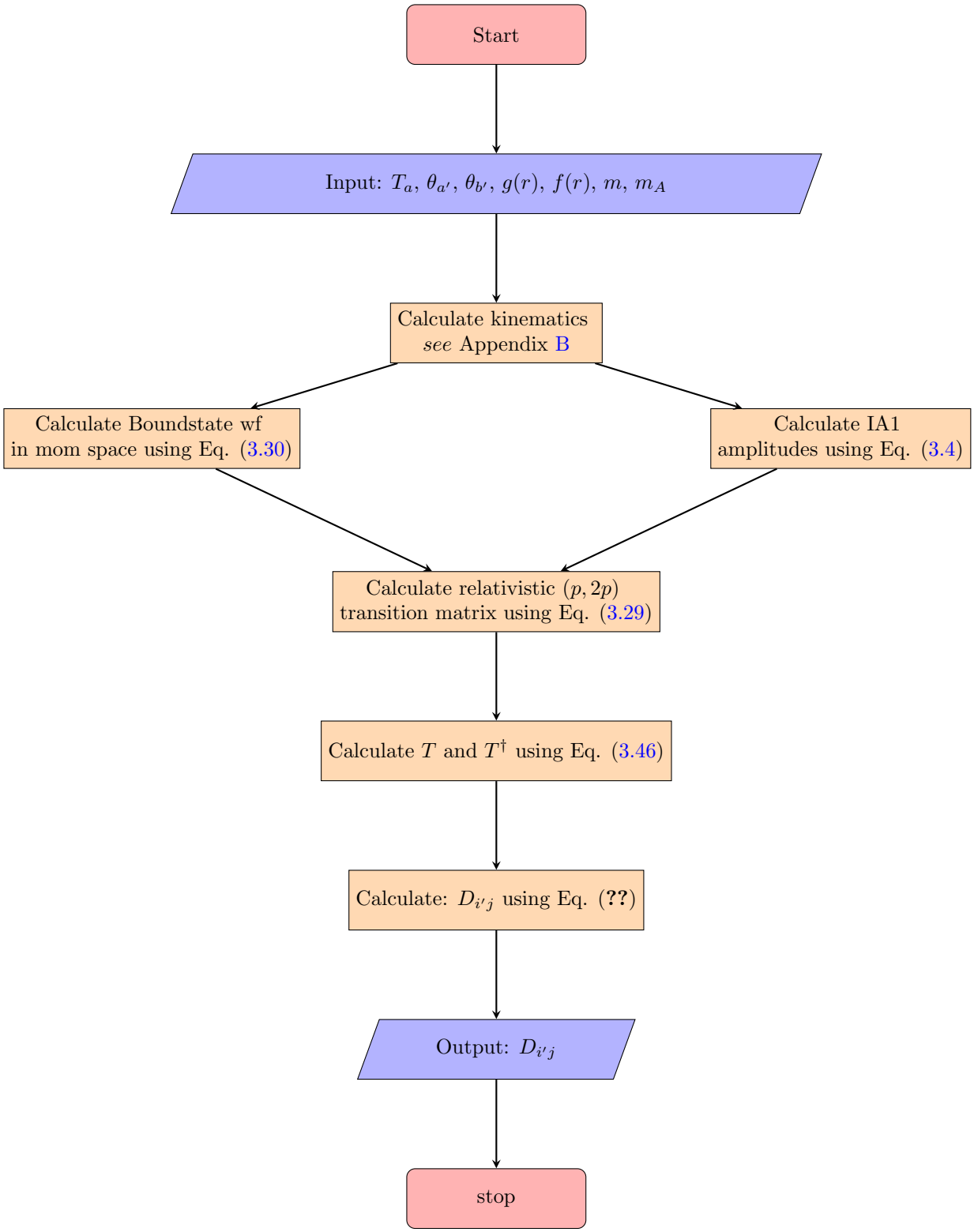

Figure 3.3: The flowchart illustrates how `Spinorbs` calculates the polarization transfer for the exclusive $(p, 2p)$ nuclear reaction.

Chapter 4

Discussion and Results

The aim of this chapter is to present and discuss the results obtained from relativistic mean field theory formalism presented in chapter 2 and relativistic plane wave model developed in chapter 3. In chapter 2 we developed a theoretical formalism to study groundstate properties of nucleus within the relativistic mean field theory. Chapter 3 focuses on the calculation of spin transfer observables of the exclusive $(p, 2p)$ knockout with both direct and inverse kinematics within relativistic plane wave formalism.

4.1 RMF results and discussions

In an effort to perform calculation based on relativistic mean field theory, we developed a Python programming language code `RMF_KE` to compute the nuclear groundstate properties using NL3 and FSUGold parameter sets within relativistic mean field theory. In Appendix A, we provide the details on how `RMF_KE` computer program operates. In order to ensure that the program works properly several numerical checks were implemented. The most important checks included comparison of calculations performed with `RMF_KE` to those calculated with a well-known RMF code, `Timora` [87]. Further numerical checks were implemented such as comparing the results from `RMF_KE` code to those generated by RMF code used in Ref [88] and they were found to be in a reasonable agreement. The Figs. 4.1 and 4.2 display the upper and lower components of proton radial wavefunction of oxygen isotopes. The expressions for the upper and lower components of radial wavefunctions are given by Eq. (2.29). We only give proton wavefunctions as these will be used to compute the the boundstate wave function which is an an integral part of transition matrix element of the exclusive $(p, 2p)$ knockout reaction. The radial wavefunctions have been calculated for all the occupied of states of ^{14,16,22,24,28}O. All oxygen nuclei plotted in Figs. 4.1 and 4.2 are magic nuclei with exception of ^{28}O nucleus. However, as seen in Eq. (3.29) the invariant transition matrix has to be evaluated in momentum space. This implies that the radial wavefunctions have to be transformed into momentum space. The Eq. (3.31) and Eq. (3.32) illustrate the Fourier transforms of the upper and lower components of position space radial wavefunctions. The Fig 4.3 depicts the upper and lower components of boundstate wave functions in momentum space as calculated with FSUGold parameter set. The momentum space radial wavefunctions have been calculated for all the occupied of states of magic oxygen nuclei for which spin transfer observables will be calculated.

Now having calculated the components of radial wavefunctions we compute the groundstate properties of various nuclei to test our model. In an effort to validate predictive power of `RMF_KE`, we opted to calculate the binding energy per nucleon, charge radius and neutron skin of various nuclei and compare with the empirical experimental data on the binding energy per nucleon, charge radius

and neutron skins from Refs [1] and [89]. Tables 4.1 and 4.2 display theoretical results for binding energy per nucleon, charge radius, and neutron-skin thickness of selected closed shell nuclei from ^{16}O to ^{68}Ni and ^{90}Zr to ^{208}Pb, respectively, which are compared with experimental values. These observables are computed with NL3 and FSUGold parameter sets which are provided in Table (2.2). The experimental data for binding energy per nucleon and charge radius were obtained from Refs. [1] and [89], respectively. The NL3 and FSUGold parameter sets reproduce experimental data for the binding energy and charge radii extremely well. Even though NL3 and FSUGold parameter sets predict different stiffness for the equation of state their prediction for binding energy and charge radii are quite similar so we can infer that these two observables have insignificant impact on the stiffness of equation of state (EoS). The results in Tables 4.1 and 4.2 show that NL3 and FSUGold models predict the ground state observables in finite nuclei throughout the nuclear chart with impressive accuracy.

We now proceed to show the evolution of average binding energy in oxygen and calcium isotopes in Fig. 4.5 and Fig. 4.6, respectively. These figures depict how binding energy changes as oxygen and calcium nucleus become neutron-rich. Figs. 4.5 and 4.6 display the evolution of groundstate energies of ^{12}O to ^{28}O and ^{34}Ca to ^{60}Ca, respectively. The data used was taken from Ref. [1] and theoretical predictions were performed with FSUGold parameter set. We also calculate single particle energies of various nuclei. Figs. 4.7 and 4.8 depict the single-neutron energy spectra of ^{24}O and ^{48}Ca, respectively, and the theoretical prediction are determined from NL3 and FSUGold parametrizations. In Fig. 4.8 there is a level inversion with $2s^{1/2}$ state occurring between $1d^{3/2}$ and $1f^{7/2}$ state. The level inversion is pronounced in the single-neutron state energies predicted by FSUGold parameter set; the NL3 parameter set predicts $2s^{1/2}$ and $1d^{3/2}$ orbital states to be almost degenerate.

In chapter 2 we also discussed the neutron skins which can be defined as the difference between neutron and proton density distributions. Fig. 4.4 shows proton and neutron density distributions in ^{208}Pb. There is a very distinct difference in the proton and neutron density distributions that is due to the fact that there are 44 excess neutrons relative to proton number in ^{208}Pb. The lead nucleus has a surface that is composed of neutrons (i.e., neutron skin). This is illustrated by huge disparities in the proton and neutron density distributions. In the Fig. 4.4 the region between the lines showing proton and neutron densities characterises what is known as neutron skin i.e a matter made purely of neutrons.

4.2 Results for Proton and Neutron Densities

Proton and neutron nuclear densities are very important in the calculation of scattering observables. In this section we present and discuss vector (matter) nuclear densities in the oxygen and calcium isotopic chains. We also discuss the evolution of charge distributions with increasing neutron number (isospin) for a fixed proton number. The calculations are performed within the relativistic mean field (RMF) formalism with NL3 and FSUGold models. Fig. 4.9 displays proton (panel a) and neutron (panel b) nuclear vector densities as a function of radial coordinate r of representative oxygen isotopes computed with FSUGold. Fig. 4.10 displays proton (panel a) and neutron (panel b) nuclear vector densities as a function of radial coordinate r of representative calcium isotopes computed with FSUGold. All the nuclei studied for both isotopic chains were found to be bound, however, from an experimental perspective the neutron drip line in oxygen chain begins at ^{26}O and consequently neither NL3 nor FSUGold is supposed to predict a boundstate of $^{26-28}$O.

It is worth noting that the differences between proton and neutron densities are directly proportional to the increase in the number of neutrons. Furthermore, as the neutron number increases, a gradual increase in the nuclear radius is observed. The effect of this is to populate and expand the neutron densities and, to a lesser degree, also the proton densities. There is a gradual decline of the proton density in the nuclear interior of oxygen isotopes as neutron numbers increase to maintain

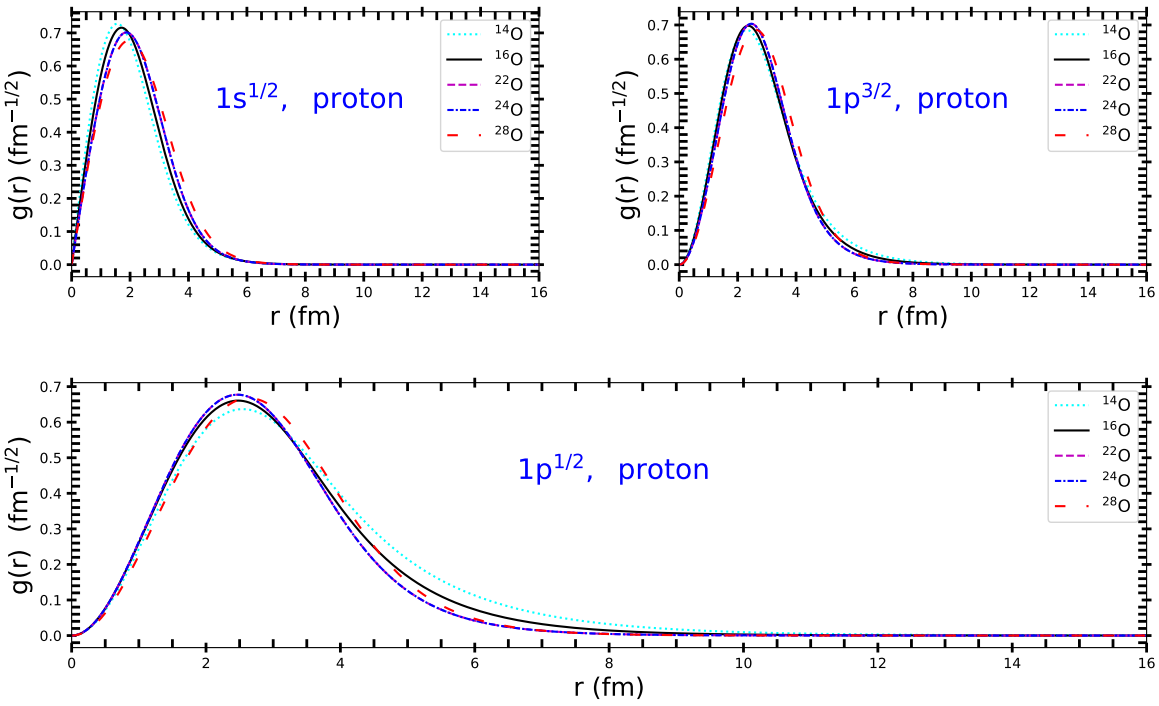

Figure 4.1: The radial upper wavefunctions g(r) of bound state protons occupying the RSM orbitals of oxygen isotopes. These radial components of the boundstate wavefunction are computed from the FSUGold parameter set.

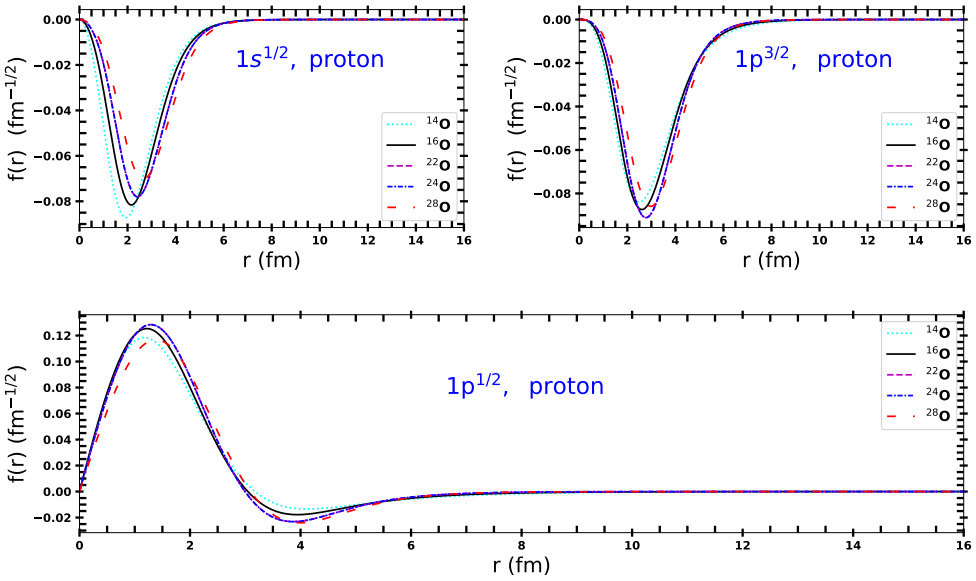

Figure 4.2: The lower radial wavefunctions f(r) of bound state protons occupying the RSM orbitals of oxygen isotopes. The radial components of the boundstate wavefunction are computed from the FSUGold parameter set.

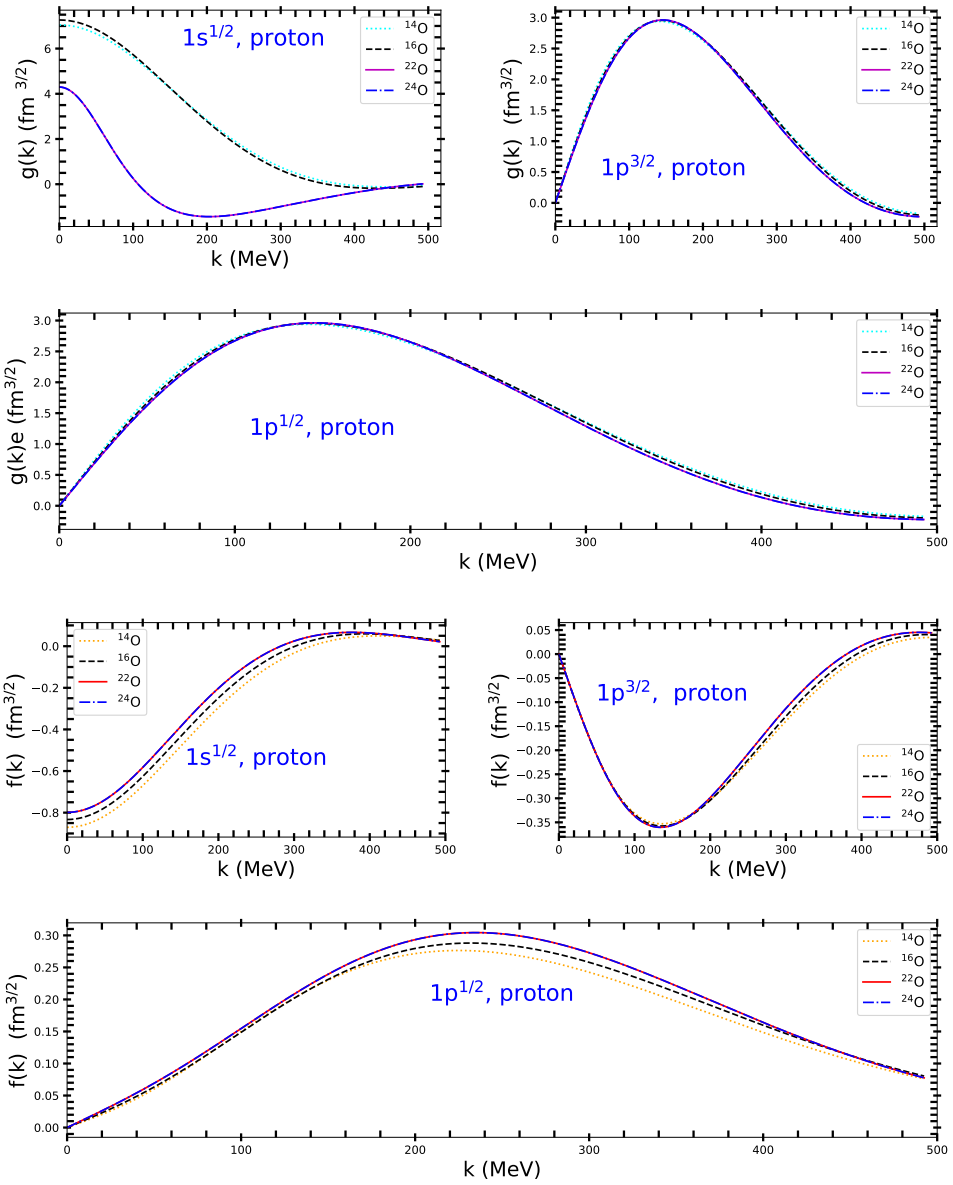

Figure 4.3: The upper g(k) and lower g(k) components of momentum space radial wavefunctions g(k) of boundstate protons occupying orbitals of oxygen isotopes. These radial components of the Dirac spinors are determined from the FSUGold parameter set.

Table 4.1: Binding energy per nucleon(B/A in MeV), charge radius (r_{ch} in fm) and neutron skin ($r_n - r_p$ in fm).

Nucleus	Observable	Experiment	NL3	FSUGold
^{16}O	B/A	7.98	8.06	7.98
	r_{ch}	2.70	2.70	2.70
	$r_n - r_p$	–	-0.03	-0.03
^{40}Ca	B/A	8.55	8.53	8.55
	r_{ch}	3.48	3.47	3.48
	$r_n - r_p$	–	-0.05	-0.05
^{48}Ca	B/A	8.67	8.66	8.58
	r_{ch}	3.48	3.49	3.48
	$r_n - r_p$	–	0.23	0.20
^{54}Ca	B/A	8.25	8.23	8.53
	r_{ch}	3.56	3.60	3.57
	$r_n - r_p$	–	0.40	0.34
^{58}Ca	B/A	7.84	7.91	8.20
	r_{ch}	–	3.62	3.60
	$r_n - r_p$	–	0.54	0.48
^{60}Ca	B/A	–	7.56	7.69
	r_{ch}	–	3.64	3.63
	$r_n - r_p$	–	0.61	0.54
^{68}Ni	B/A	8.68	8.71	8.66
	r_{ch}	–	3.88	3.88
	$r_n - r_p$	–	0.26	0.21

Table 4.2: Binding energy per nucleon(B/A in MeV), charge radius (r_{ch} in fm) and neutron skin ($r_n - r_p$ in fm).

Nucleus	Observable	Experiment	NL3	FSUGold
^{90}Zr	B/A	8.71	8.70	8.68
	r_{ch}	4.27	4.28	4.27
	$r_n - r_p$	–	-0.03	-0.03
^{98}Zr	B/A	8.25	8.30	8.68
	r_{ch}	4.40	4.38	4.40
	$r_n - r_p$	–	0.24	0.20
^{100}Sn	B/A	8.25	8.30	8.24
	r_{ch}	–	4.48	4.48
	$r_n - r_p$	–	0.08	0.08
^{116}Sn	B/A	8.52	8.50	8.24
	r_{ch}	4.63	4.63	4.63
	$r_n - r_p$	–	0.40	0.34
^{132}Sn	B/A	8.36	8.38	8.34
	r_{ch}	4.71	4.72	4.74
	$r_n - r_p$	–	0.17	0.12
^{208}Pb	B/A	7.87	7.90	7.89
	r_{ch}	5.50	5.53	5.54
	$r_n - r_p$	$0.33^{+0.16}_{-0.18}$ [90]	0.28	0.21

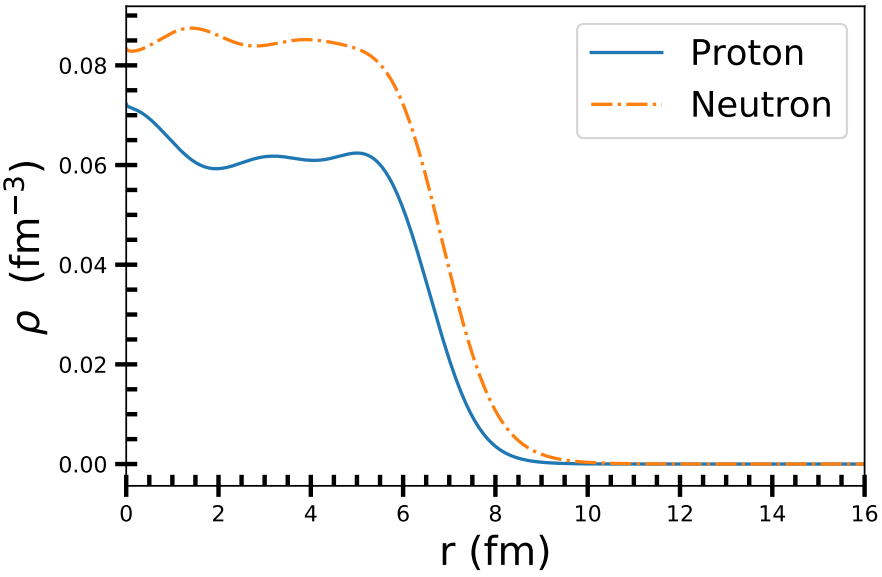

Figure 4.4: Proton and neutron density distributions in ^{208}Pb as predicted by NL3 parameter set.

the normalization to the constant number of protons. The same trend is observed in the density distributions of calcium isotopic chain in Fig. 4.10.

The nuclear charge distributions provide a significant information regarding nuclear structure of nuclei as they are directly related to the wave functions of protons. In the stability region of nuclear landscape, electron-nucleus scattering has been used as one of the powerful probes to investigate nuclear charge densities. The measurements of charge distributions of exotic nuclei are planned to be obtained by colliding electron with exotic nuclei with in storage rings at RIB facilities. The Fig. 4.11 shows theoretical predictions of charge distributions amongst the magic nuclei within isotopic oxygen chain. It is clear that addition of neutron in has an effect of lowering the charge distribution. The calculations for NL3 and FSUGold agree quite well.

4.3 RPWIA results and discussions

We begin this section by motivating our choice to calculate the polarization transfer observables for the oxygen-isotopic chain. The stable oxygen nucleus ^{16}O has been studied extensively and its structure is well-understood [91]. Furthermore, there exists studies of exclusive $^{16}\mathrm{O}(\vec{p}, 2p)$ of spin observables which will serve as a guide for the quantitative analysis we give here for select members of oxygen isotopic chain. The oxygen isotopes are interesting to investigate because they are the heaviest nuclei for which the neutron drip line has been established. The experimental evidence suggests that all neutron-rich oxygen isotopes up to ^{24}O [92] fall within the neutron drip line and that ^{25}O [93, 94], ^{26}O [95, 96], ^{27}O [97] and ^{28}O lie outside of neutron drip line. From these isotopes, ^{28}O seems to be an unexpected departure from nuclei with high stability because according to the shell-model of Mayer, Jensen and Suess the $Z = 8$ and $N = 20$ are magic number for stable nuclei. It was expected that ^{28}O composed of 8 protons and 28 neutrons would be a closed-shell nucleus or at very least display stability. However, in neuron-rich nuclei new magic nuclei have been identified and in the oxygen chain experimental observations identified ^{14,16,24}O as strong doubly magic nuclei and ^{22}O as weak doubly magic nucleus. The prevalence of magicity in the oxygen-isotopic chain and the fact that

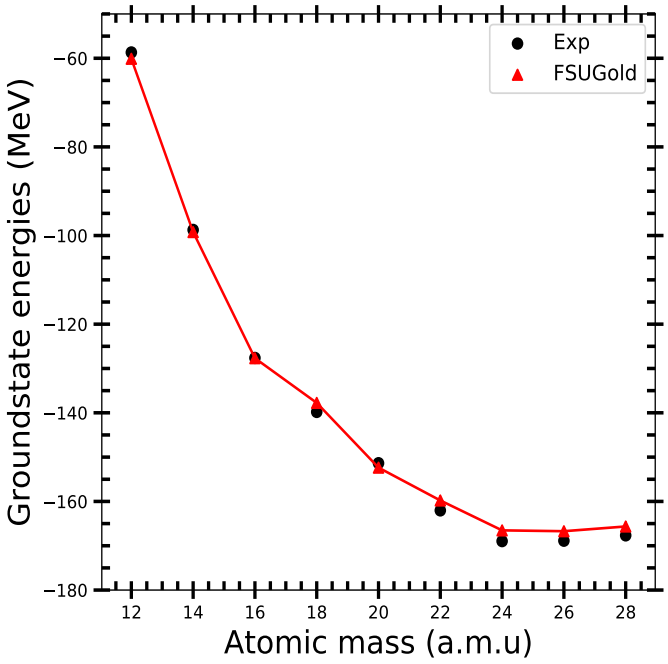

Figure 4.5: The groundstate energies of oxygen isotopes as predicted by FSUGold parameter set and the data are taken from Ref [1]. The solid line serves merely to guide the eye.

experimentally magic numbers are more accessible influenced the choice of these particular isotopes. This is in addition to the fact that oxygen isotopes being medium-size nuclei are very suited for the investigation of the details of nuclear forces. The curious features of nuclear forces between nucleons moving in orbits with specific quantum numbers are much better studied in medium nuclei.

There exists no experimental measurements for a complete set of exclusive $(p, 2p)$ scattering reaction spin observables from unstable nuclei with inverse kinematics and this presents a challenge to our theoretical study pertaining to the choice of kinematical conditions. However, TRIUMF undertook experimental measurements [73] for the analysing power of the $^{16}\mathrm{O}(p, 2p)$ reaction for different single particle orbits at an incoming energy of 504 MeV where the coplanar angles were fixed at several angle pairs. The two spin-transfer observables $D_{s's}$ and$D_{s'l}$ for nucleon knockout from an ^{16}O target were also measured in this experiment. The significance of this TRUIMF experiment from a historical perspective is that same experiment made first experimental measurements for spin transfer obervables at intermediate energies for the exclusive $(p, 2p)$ reaction. The spin transfer observables for the $(p, 2p)$ were measured as a function of the angle made by the scattered proton $\theta_{b'}$. All subsequent exclusive $(p, 2p)$ reaction experiments worldwide measured spin observables as a function of kinetic energy of the scattered proton $T_{a'}$. The TRIUMF experiment motivated the choice for energy of the incident proton and angle pairs for our calculations. The TRIUMF experiment only extracted spin transfer observables for $1s^{1/2}$ but not p-shell knockout because of uncertainties associated with fitting the low-statistics $1p^{1/2}$ and $1p^{3/2}$ peaks in the missing mass spectra. However, it is expected that in inverse kinematics these uncertainties will be minimized, therefore, in this theoretical study we extract spin observables from $1s^{1/2}$, and $1p^{1/2}$ in inverse kinematics. The calculations in the direct kinematics for $^{16}\mathrm{O}(p, 2p)$ reaction will also be restricted to $1s^{1/2}$ and $1p^{1/2}$. The kinematical conditions are chosen such that the effects of absorption on the final state nucleons are minimized. The spin observables computed with both direct and inverse kinematics will utilise the Arndt amplitudes [86] of the nucleon-nucleon interaction. It expected that since these amplitudes are calculated directly

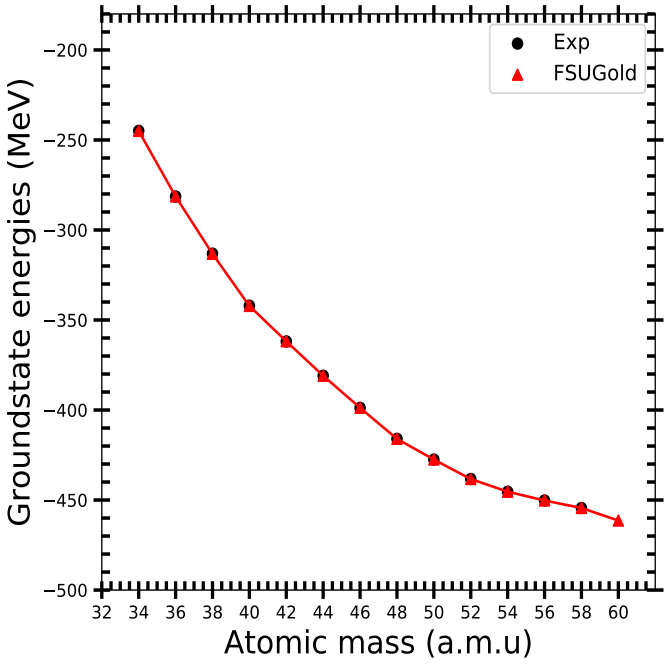

Figure 4.6: The groundstate energies of calcium isotopes as predicted by FSUGold parameter set and the data are taken from Ref [1]. The solid line serves merely to guide the eye.

from experimental phase shifts they will give a better approximation of spin observables compared to any other phenomenological model including the Horowitz-Love-Franey model.

Numerical checks form the backbone of any numerical model in physics. However, if one has experimental data to compare with then it is often easier to gauge predictive power of the model. Therefore in this study, where there is an absence of experimental data to compare against, theoretical model has to undergo stringent numerical tests. A Python code named `Spinorbs` was written to perfor the calculations of spin observables. We developed `Spinorbs` entirely within Python programming language. `Spinorbs` uses a kinematics code described in Appendix B. The Fig. 3.3 illustrates how `Spinorbs` computes polarization transfer observables. Note that since kinematics and transition matrix for the exclusive $(p, 2p)$ nuclear reaction with direct and inverse kinematics are different we have two versions of `Spinorbs`. We have a version designed for direct kinematics and the other written to do calculations for the inverse kinematics. The `Spinorbs` takes radial wavefunction which are computed within the framework of relativistic mean field theory[1](FSUGold) as part of input parameters to compute the boundstate wavefunction in momentum space (*see* Eq. (3.30)) needed to compute the invariant matrix element. To be certain that the radial functions used are reliable, a calculation was performed to confirm that the radial wavefunctions respect the normalization condition in Eq. (2.36). Note that the relativistic mean field theory calculation were calculated with `KE_RMF`[2] which was written in Python and Fortran using the Python package f2py. The integral to perform Fourier transform in Eq. (3.28) was evaluated using Gauss-Legendre integration and the results were verified using the other numerical integration quadratures such as Gauss-Kronrod [98]. We plot the momentum space upper and lower components of boundstate wave function for doubly magic oxygen isotopes Figs. 4.3 - **??**. In this study for IA1 representation the NN scattering amplitudes used are calculated directly

[1] Our RMF calculations are vindicated by experimental data. *See* Chapter 2
[2] *See* Appendix A on how `KE_RMF` code performs RMF calculation

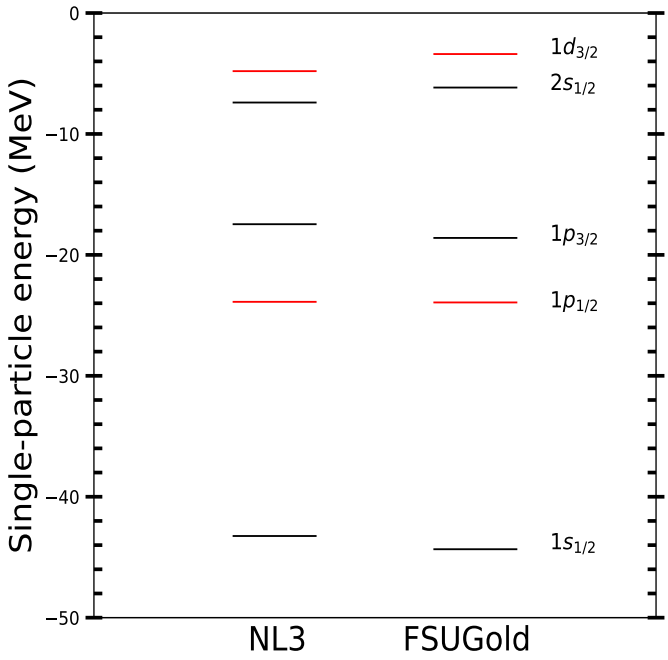

Figure 4.7: Single-neutron energy spectrum for ^{24}O as predicted by NL3 and FSUGold parameter sets.

from Arndt phases. In an effort to ensure proper calculation of the amplitudes the spin observables calculated with Arndt amplitudes were compared with the spin observables calculated with NN amplitudes coming from $\hat{F}^{11}$ (which are essentially the SPVAT form) amplitudes of IA2 representation and they were found to be equal.

4.4 Calculations of Spin Observables

The proper implementation of the boundstate wave function is an essential part of the relativistic impulse approximation models. To this end we computed the Fourier transforms of radial wavefunction of each state of the bound nucleons of the oxygen isotopes considered. In addition, since the invariant scattering matrix element (*see* Eq. (3.29)) is proportional to the Fourier transformed boundstate wavefunction, we examine the momentum nature of the wavefunction. The lower and upper components of the momentum space boundstate wavefunction for the orbitals of the doubly magic oxygen isotopes occupied by proton are presented in Fig. 4.3. The components were calculated with the FSUGold parameter set which is provided in Table 2.2 of chapter 2 and the significance of these plots other than for proper calculation of the spin observables is that they serve to show that FSUGold parameter set predict the oxygen isotopes considered here to be bound. For the orbitals considered it is apparent that both lower and upper wavefunctions are significant for momentum $k \leq 350$ MeV and reach maximum at around momentum $k \leq 150$ MeV. The results for the exclusive $(p, 2p)$ reaction spin observables for IA1 representation are presented in this chapter.

The results presented for the spin transfer orbservables can be separated into two categories namely those computed with direct kinematics and those that are calculated with the inverse kinematics. The choice for kinematical conditions for the spin observables in the direct kinematics is partly informed by those used in a TRIUMF experiment [73] to measure the analysing power and two spin-transfer

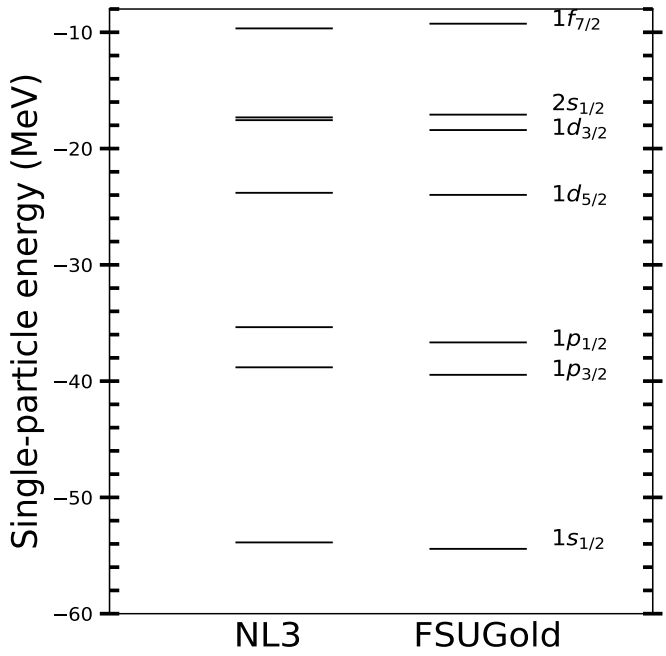

Figure 4.8: Single-neutron energy spectrum for ^{48}Ca as predicted by NL3 and FSUGold. Note the occurrence of level inversion wherein the $1d^{3/2}$ state appears below the $2s^{1/2}$ it is predicted by both models.

observables ($D_{s's}$ and $D_{s'l}$). For the direct kinematics we consider proton knockout reaction from $s^{1/2}$ state and $p^{1/2}$ state of the ^{16}O target via an exclusive $(p, 2p)$ reaction. The incoming polarized-proton of 504 MeV is used and the angles of scattered proton and outgoing proton are fixed at $\theta_{a'} = 22.12$ and $\theta_{b'} = -40.3$, respectively. The NN scattering matrix in these calculations is based on a direct parametrization of the Arndt ampltitudes. In order to ensure that our numerical implementation is properly executed, the spin observables of ^{16}O calculated directly from Arndt amplitudes [86] were compared to spin observables calculated with F^{11} amplitudes. The results are presented in Fig. 4.14 and were found to be in reasonable agreement with each other. These figures demonstrate that our RPWIA model to calculate the spin transfer observables, $D_{i'j}$, was implemented correctly. The results were generated with Python code `Spinorbs`. Fig. 4.15 - 4.16 displays the analysing power, polarization and transfer coefficients of $1p^{1/2}$ of ^{16}O calculated with direct kinematics.

Since there are no experimental data to constrain the inverse kinematical conditions for the measurement of spin transfer observables the following was taken into consideration in arriving at the choice of kinematics in this chapter. The incident energy of nuclei was chosen in such a way that there will be minimum distortion effects during the collision of the target proton and bound proton in the incident nuclei. The choice for angle pairs was also motivated by the same consideration as for incident energy and also a desire to minimize the effects of absorption on the final state nucleons. The kinematical conditions will also permit us to investigate deep lying states with inverse kinematics: the incoming energy of 504 MeV and the angle pair $(22.12°, -40.30°)$ for $\theta_{a'}$ and $\theta_{b'}$, respectively. The Figs. 4.17-4.20 show the results of analzing power, polarization and $D_{i'j}$ from $1s^{1/2}$ and $1p^{1/2}$ of ^{14}O calculated with the inverse kinematics.

The Fig. 4.14 illustrates the results of spin transfer observables of ^{16}O calculated directly from Arndt phase shifts and from F^{11}. The results are in agreement with each other showing that `Spinors`

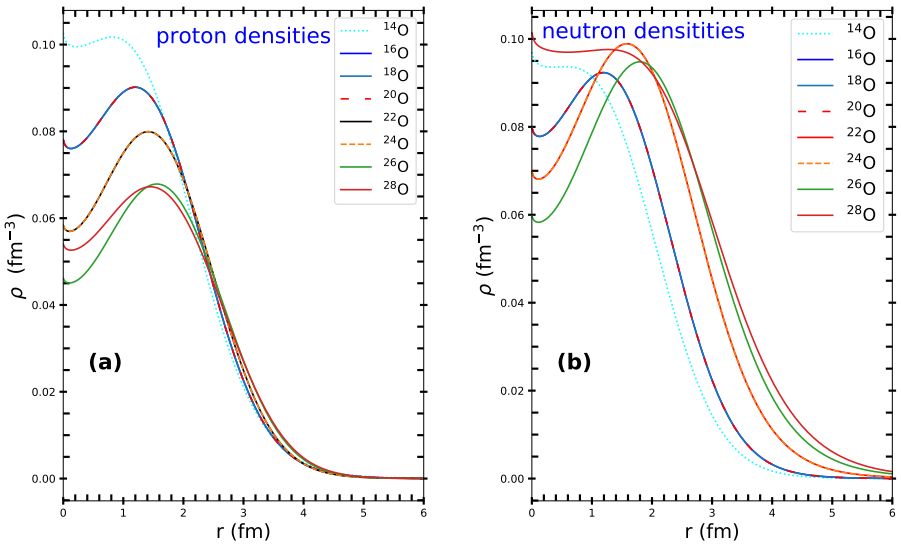

Figure 4.9: Proton, panel (a), and neutron, panel (b), vector densities for the various oxygen isotopes.

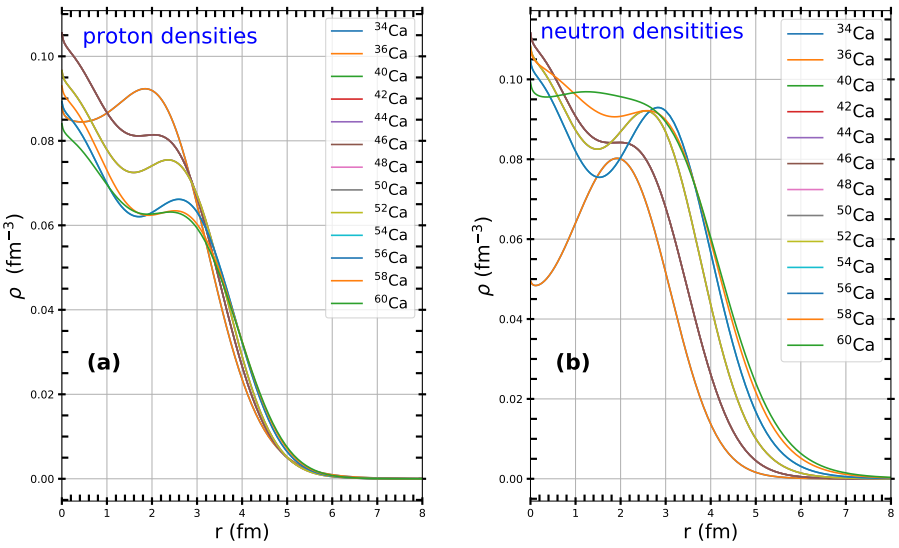

Figure 4.10: Proton, panel (a), and neutron, panel (b), vector densities for the various calcium isotopes.

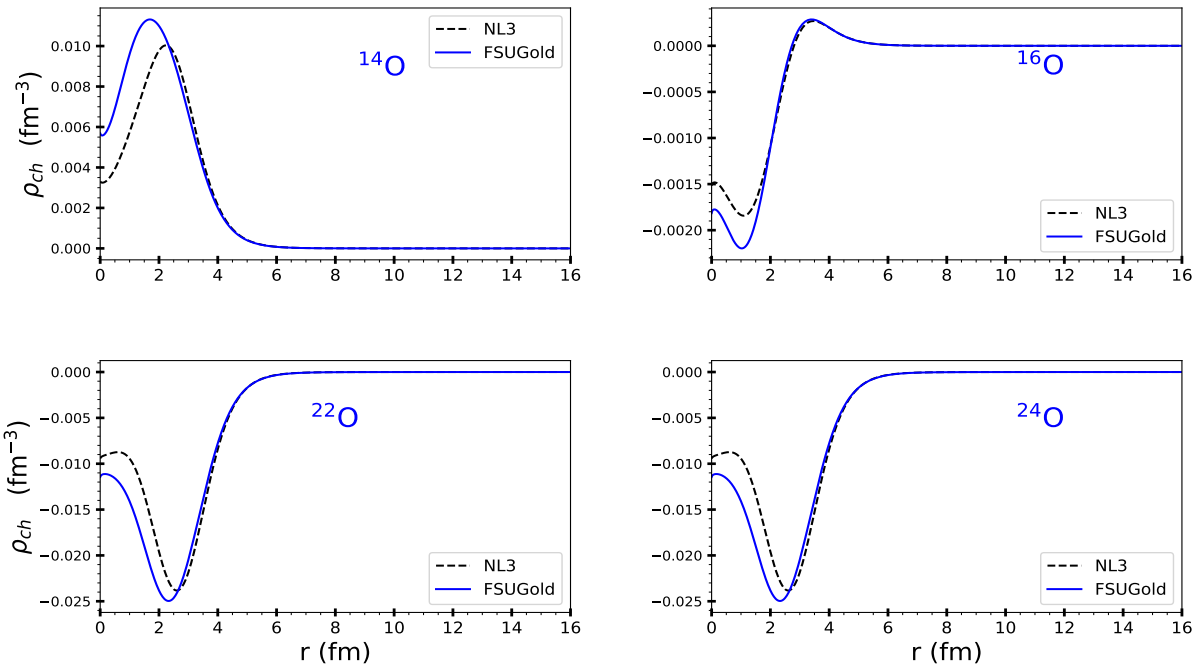

Figure 4.11: Evolution of charge density along doubly-magic oxygen nuclei as predicted by NL3 and FSUGold.

was properly programmed. The Figs. (4.17 - 4.18) illustrate the complete set of spin transfer observables of the ^{14,22,24}O isotopes from $1s^{1/2}$ computed with the inverse kinematics. The kimematical conditions are given above. We see that analyzing power A_y, induced polarization P, and D_{nn} are the only spin-transfer observables which differentiate between various oxygen isotopes. The remaining spin transfer observables are practically identical for all oxygen isotopes. This implies that in order to study the nuclear medium modification in oxygen isotopes with inverse kinematics using exclusive $(p, 2p)$ the spin observables that will need to be measured are analyzing power A_y, induced polarization P, and D_{nn}. In Fig. 4.19 - 4.20 we studied the spin transfer observables from $1p^{1/2}$ of ^{14,22,24}O isotopes, all spin transfer observables are the same for ^{22,24}O and different from ^{14}O.

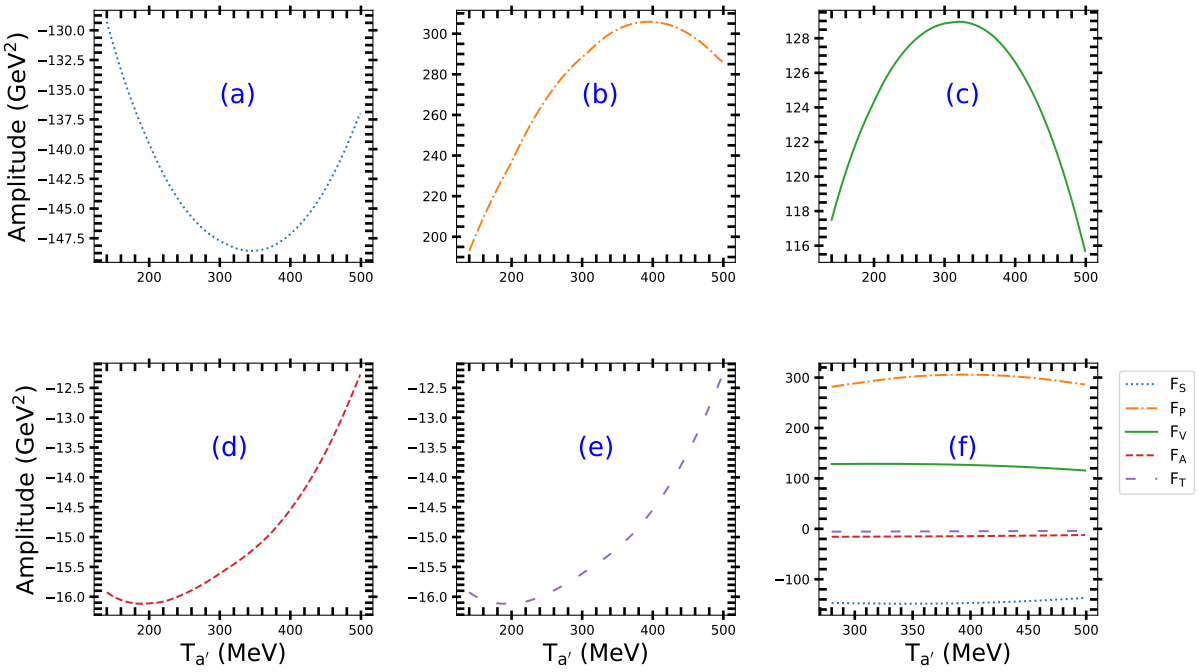

Figure 4.12: The real parts of IA1 amplitudes used for the computation of spin-transfer observables for proton knockout from ^{16}O target.

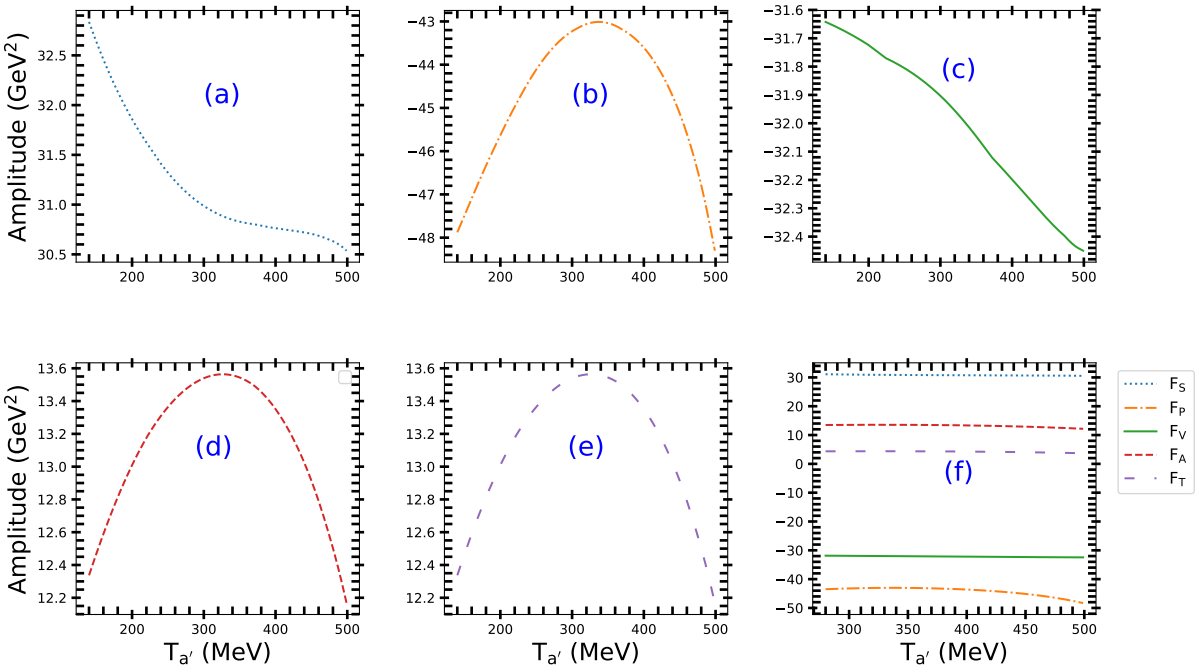

Figure 4.13: The imaginary parts of IA1 amplitudes used for the computation of spin-transfer observables for proton knockout from ^{16}O target.

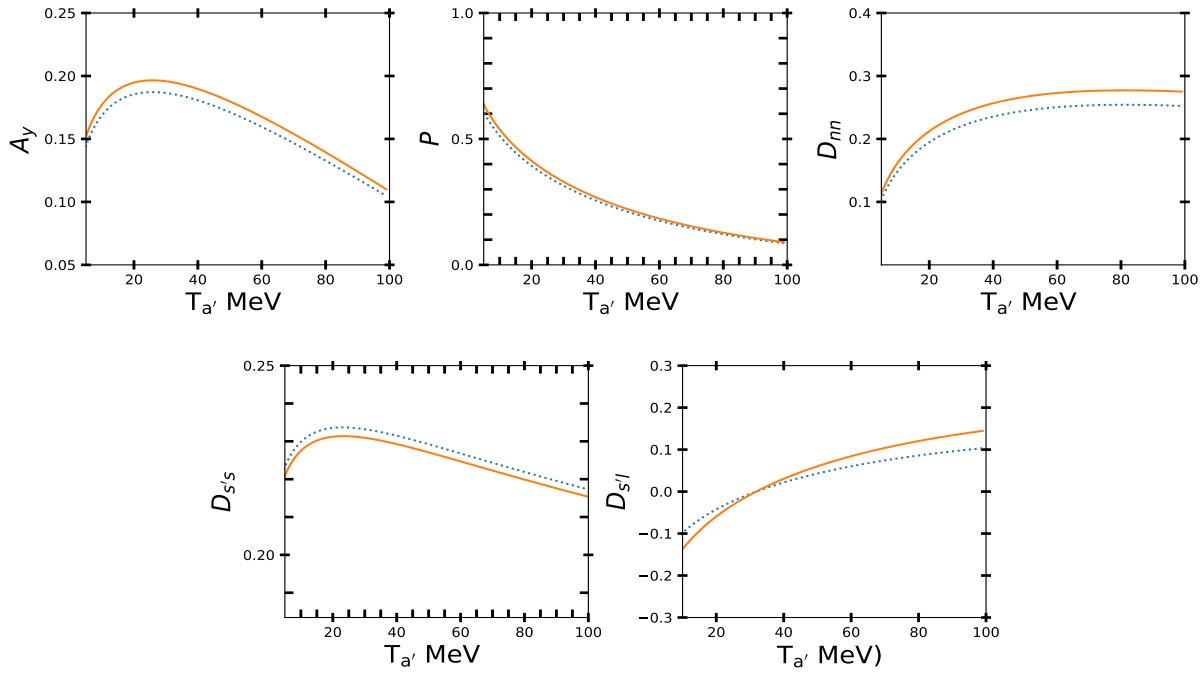

Figure 4.14: The $(p, 2p)$ spin observables as a function of laboratory kinetic energy $T_{a'}$ of the scattered proton a', for proton knock-out from the $1s^{1/2}$ orbital of ^{16}O at an incident energy of 504 MeV, and for coincident coplanar scattering angles $(22.12°, -40.30°)$. The solid lines depict spin observables calculated directly from Arndt amplitudes while the dotted line depicts amplitudes calculated from F^{11} amplitudes.

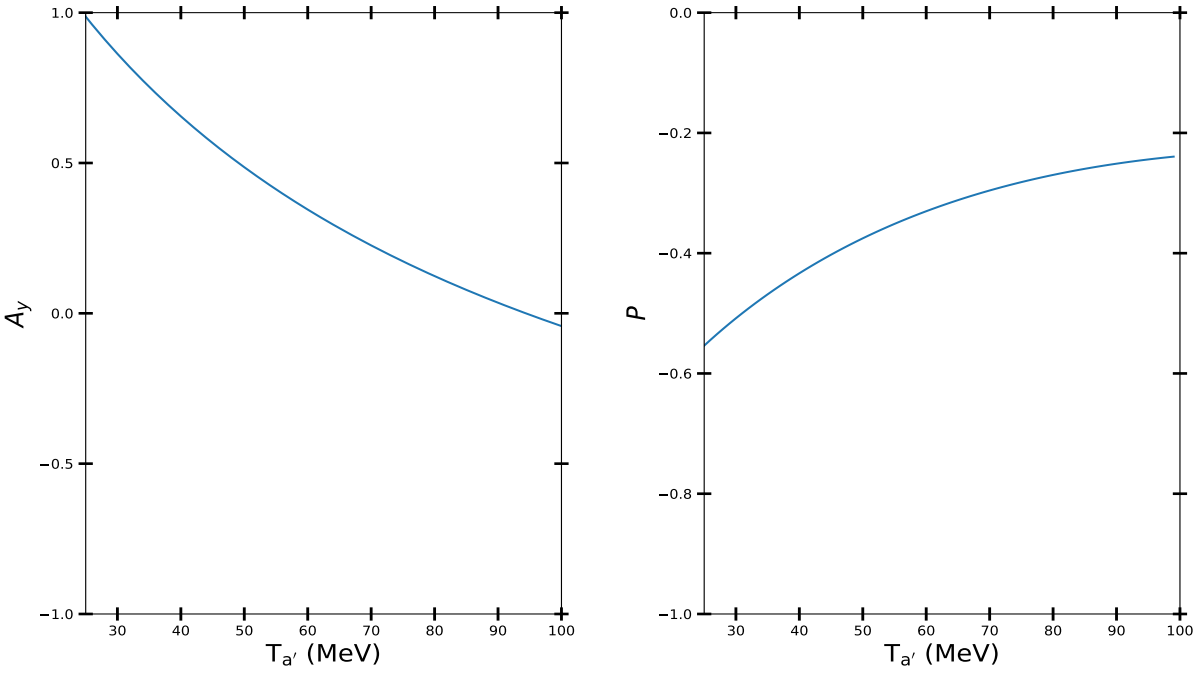

Figure 4.15: Values of analyzing power and induced polarization as a function of laboratory kinetic energy $T_{a'}$ of the scattered proton a', for proton knock-out from the $1p^{1/2}$ orbital of ^{16}O at an incident energy of 504 MeV, and for coincident coplanar scattering angles $(22.12°, -40.30°)$.

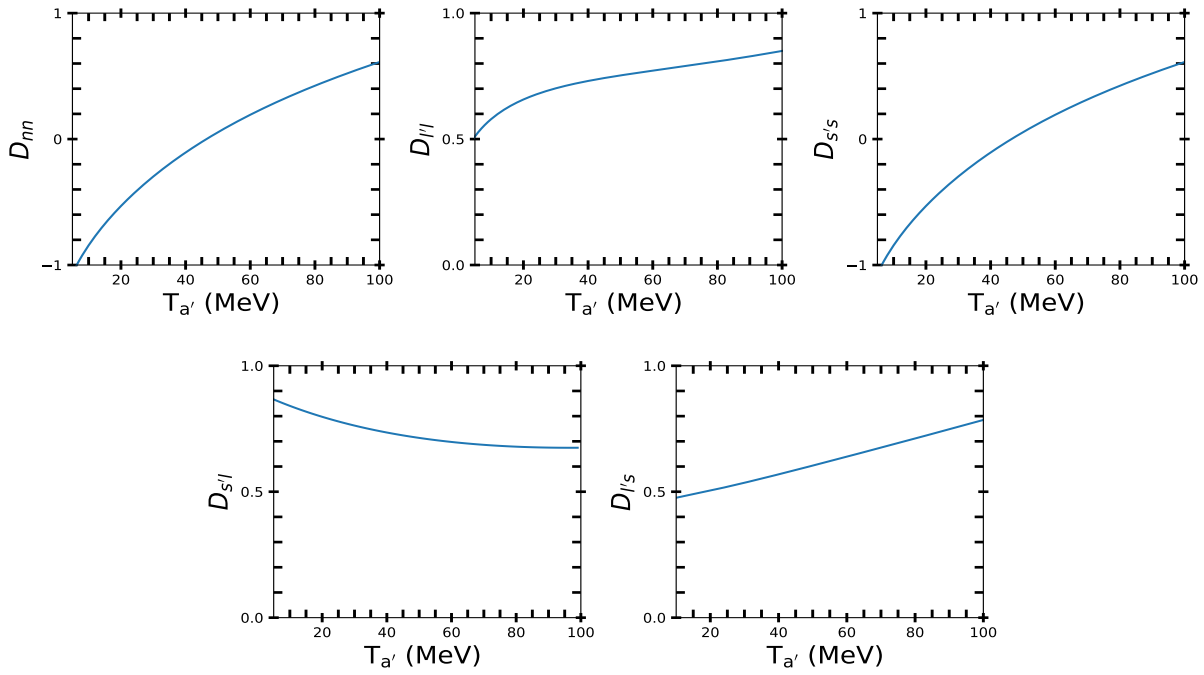

Figure 4.16: Values of polarization of transfer coefficients $D_{i'j}$ as a function of laboratory kinetic energy $T_{a'}$ of the scattered proton a', for proton knock-out from the $1p^{1/2}$ orbital of ^{16}O at an incident energy of 504 MeV, and for coincident coplanar scattering angles $(22.12°, -40.30°)$.

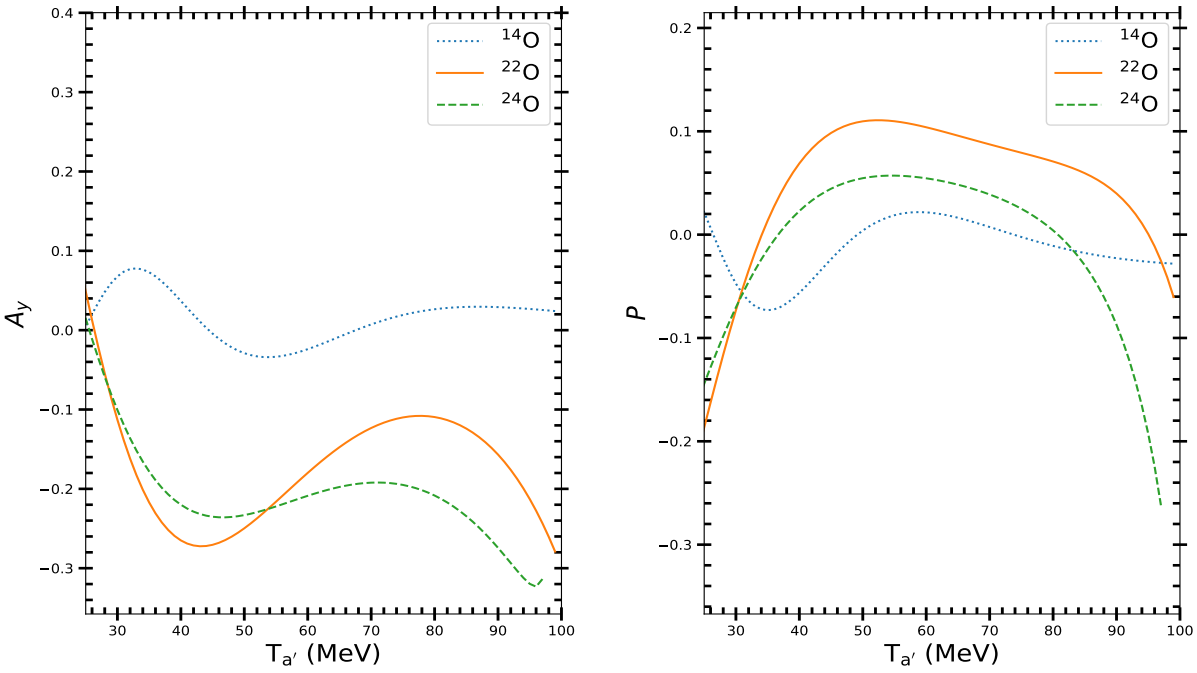

Figure 4.17: Values of analyzing power and induced polarization as a function of laboratory kinetic energy $T_{a'}$ of the scattered proton a', for proton knock-out from the $1s^{1/2}$ orbital of ^{14,22,24}O at an incident energy of 504 MeV, and for coincident coplanar scattering angles $(22.12°, -40.30°)$.

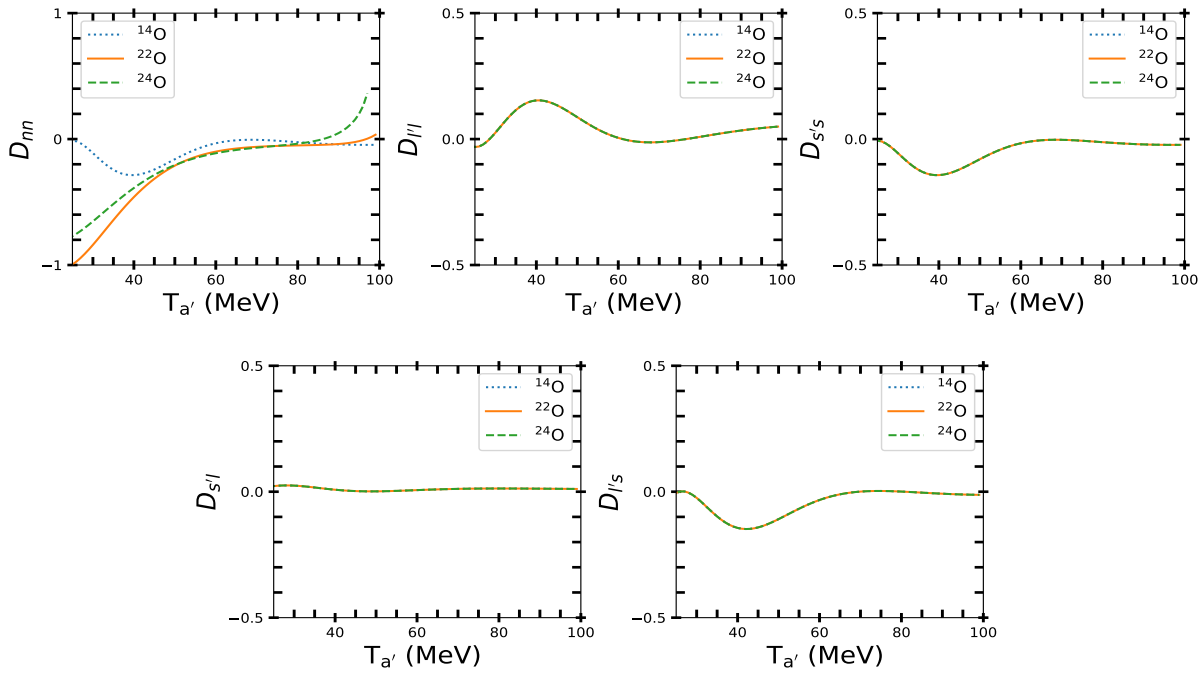

Figure 4.18: Values of polarization of transfer coefficients $D_{i'j}$ as a function of laboratory kinetic energy $T_{a'}$ of the scattered proton a', for proton knock-out from the $1s^{1/2}$ orbital of ^{14,22,24}O at an incident energy of 504 MeV, and for coincident coplanar scattering angles $(22.12°, -40.30°)$.

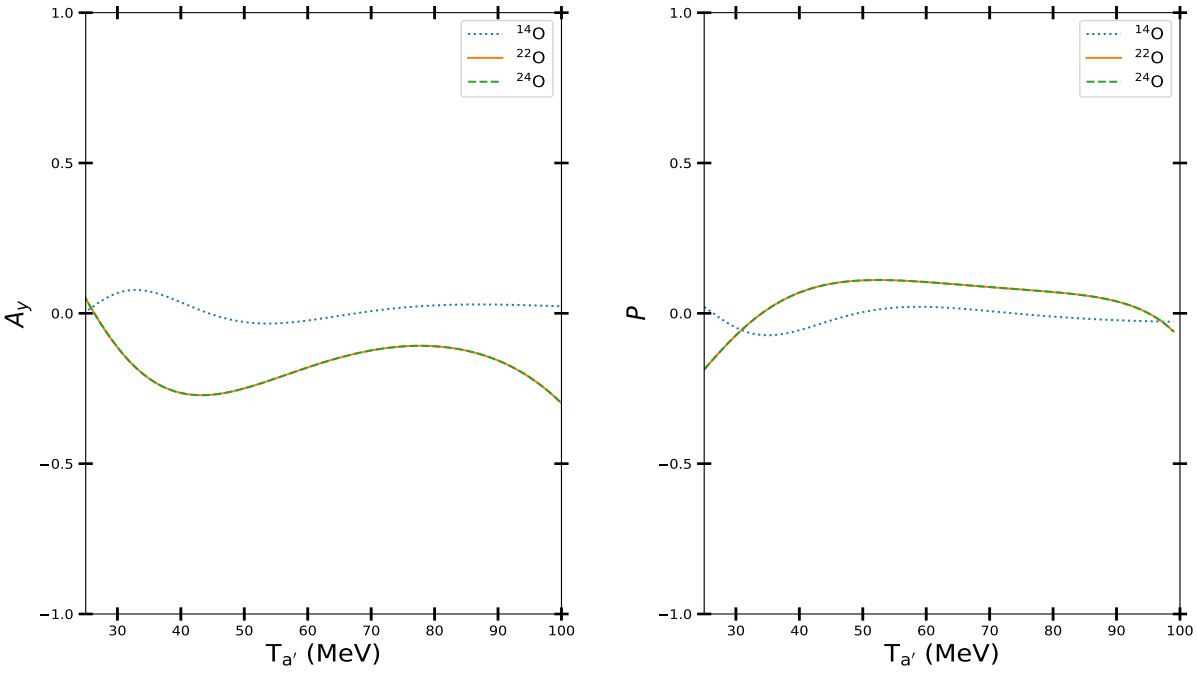

Figure 4.19: Values of analyzing power and induced polarization as a function of laboratory kinetic energy $T_{a'}$ of the scattered proton a', for proton knock-out from the $1p^{1/2}$ orbital of ^{14,22,24}O at an incident energy of 504 MeV, and for coincident coplanar scattering angles $(22.12°, -40.30°)$.

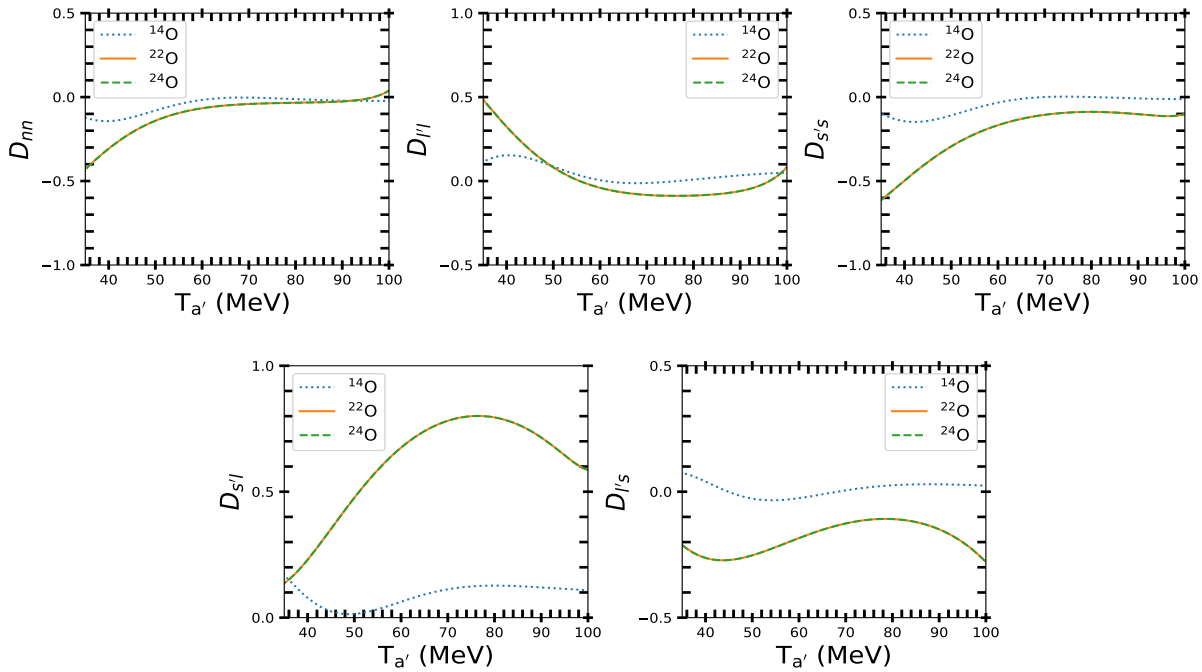

Figure 4.20: Values of polarization transfer coefficients $D_{i'j}$ as a function of laboratory kinetic energy $T_{a'}$ of the scattered proton a', for proton knock-out from the $1p^{1/2}$ orbital of ^{14,22,24}O at an incident energy of 504 MeV, and for coincident coplanar scattering angles $(22.12°, -40.30°)$.

Chapter 5

Summary and outlook

The first part (*see* chapter 2) of this manuscript sought to investigate nuclear structure, in particular the ground state properties, of finite nuclei throughout the nuclear landscape in the framework of relativistic mean field theory and the findings were presented in chapter 2. A variety of nuclear phenomena such as halos and skins were studied. We observed that the main difference between stable nuclei and nuclei far from the stability region is that neutron/proton-rich nuclei tend to have extended neutron/proton distributions in a form of nuclear halos, or skins. The unstable nuclei also have a smaller binding energy per nucleon compared to stable nuclei. The understanding of nuclei with large neutron-proton asymmetry provides us with unique insights into nuclear structure of nuclei unavailable in nature due to their lack of stability. The rare isotope beam (RIB) facilities make unstable isotopes accessible for the studies of astrophysics and nucleosynthesis in terrestrial laboratories. This allows us to study, among others things neutron skins, in essence neutron matter that was once thought to only exist in neutron stars. The groundstate properties of stable and unstable nuclei such as binding energies and charge radii were computed with FSUGold and NL3 parameter sets and compared with experimental data and good agreement was found. The results of chapter 2 indicated that NL3 and FSUGold predict ground state properties of nuclei throughout the nuclear chart very well (*see* Tables 4.1 and 4.2). In summary, in the first part of the manuscript we used the RMF theory to advance the understanding of nuclear force and contribute to the efforts of establishing the limits of nuclear existence.

In the second part (*see* chapter 3) of this manuscript we studied proton-induced knockout reactions in the intermediate energy regime (100 - 1000 MeV) from doubly magic nuclei using a fully relativistic formalism in the framework of relativistic plane wave approximation (RPWIA). The doubly magic nuclei or the so-called closed shell nuclei are preferred because they are suited for exclusive reaction process to take place. We developed a general RPWIA model that is suitable for the investigation of exclusive $(p, 2p)$ and (p, pn) reactions but in this work we only studied the exclusive $(p, 2p)$ reaction. This was motivated by the fact that the exclusive $(p, 2p)$ reactions have been studied extensively and these reactions tend to have large cross-sections. Moreover, in the laboratory, it is easier to extract the polarization transfer observables from the exclusive $(p, 2p)$ reactions as opposed to exclusive (p, pn). In addition, in the polarization measurements the exclusive $(p, 2p)$ are j-dependent which makes $(p, 2p)$ a unique nuclear spectroscopic tool unmatched by any knockout reactions. The relativistic impulse approximation to the $(p, 2p)$ reaction assumes that the scattering reaction can be reduced to a two body scattering process. In the direct kinematics the incident proton only interacts with the target proton in a particular orbital of the stationary nucleus. Similarly, for inverse kinematics the boundstate proton in the incident nucleus interacts with the target proton. In our model we take into consideration the fact that the reaction takes place in the nuclear field and incorporate the medium effects such as nuclear binding, Fermi motion, Pauli Blocking etc via the bound state wave function

computed from the relativistic mean field theory with FSUGold parameter set.

Our RPWIA model was used to study polarization transfer observables which are regarded to be sensitive to nuclear medium modification effects, while remaining insensitive to the final state interaction effects. The use of RPWIA in this study is justified by the following reasons:

1. RPWIA model incorporates the main features of the exclusive $(p, 2p)$ scattering reaction.
2. RPWIA model provides baseline calculation for inclusion of nuclear distortion effects.
3. RPWIA forms the baseline against which future RDWIA calculations must be compared.
4. From a theoretical view point the RPWIA offers analytical manipulation in a form of the trace method (*see* Appendix C) which eases numerical implementation.
5. RPWIA provides a first order approximation of the behaviour of the observables of exclusive scattering reactions.
6. RPWIA model is best suited for the study of spin transfer observables of the exclusive $A(a, a'b')B$ since distortions are negligible in such investigations.

Moreover, since this study is exploratory in its nature the we believe that RPWIA formalism provides the best framework to carry out our investigation because the more sophisticated RDWIA formalism is prone to errors and its execution takes time to produce results. However, the implementation of a fully relativistic distorted wave impulse approximation (RDWIA) builds on RPWIA thus this study is a first step towards building RDWIA.

We summarise the findings of this work as follows: we computed a complete set of exclusive $(p, 2p)$ knock-out reaction polarization transfer observables of closed shell oxygen isotopes ^{14,22,24}O with inverse kinematics at 504 MeV for coplanar angle pair $(22.12°, -40.30°)$. The main aim of the study was to investigate evolution of polarization transfer observables within this particular isotopic chain. The other objectives included identifying polarization transfer observables which discriminate between different isotopes as this offers the opportunity to investigate medium modification as the nucleus becomes neutron-rich. To this end, a relativistic plane wave impulse approximation was developed mainly because of insensitivity of polarization transfer observables to distortion effects and partly as this is a quantitative study the inclusion of distorting optical potentials on scattering wave function would have added an extra layer of complication to the calculations. The nuclear structure of the isotopes investigated were taken into account within the relativistic mean field approximation using the FSUGold parameter set. We would like to bring to the attention that the relativistic formalism presented in this manuscript can with ease be used for the inclusion of distortion effects as the invariant matrix element is computed directly. In addition, we stress that this formalism, albeit, with minor modifications can be used to study neutrino-induced strange particle production on nuclei or any quasifree knockout reaction of the form $A(a, a'b')B$.

We found that analysing power A_y, polarization P, and D_{nn} of $1s^{1/2}$ state of ^{14,22,24}O at 504 MeV for angle pair $(22.12°, -40.30°)$ are the only polarization transfer observables that distinguish between the different oxygen isotopes. The differences in the magnitudes of these observables are pronounced for analysing power A_y and polarization P. However, the differences in D_{nn} are peripheral, in fact, at certain energies this observable cannot discriminate between different oxygen isotopes. The rest of the spin transfer coefficients $(D_{l'l}, D_{s's}, D_{s'l}, D_{l's})$ are virtually the same for $1s^{1/2}$ state of ^{14,22,24}O at 504 MeV for angle pair $(22.12°, -40.30°)$. This is consistent with a long-held view that spin transfer observables are independent of the target nuclei[1]. The polarization transfer coefficients extracted

[1] In this case projectile nuclei

from $1p^{1/2}$ state of ^{14,22,24}O at 504 MeV for angle pair $(22.12^{\circ}, -40.30^{\circ})$ for the ^{22,24}O are the same and different from ^{14}O. The similarity between observables of ^{22,24}O for $1p^{1/2}$ state and, analogously, differences to ^{14}O could be due to kinematic choices or could be due to the fact that only s state is suited for measurement of polarization transfer observables. We argue it has nothing to do with the mass differences between these oxygen isotopes, otherwise the same results would have emerged in the calculations of spin observables from $1s^{1/2}$ state. This study is timely in a sense that plenty of rare isotope accelerator facilities are now operational and in the next few years years many more will become operational. Therefore, it is inevitable that soon these facilities will have capacity to measure spin transfer observables.

In future the following aspects in relativistic can be investigated:

1. Calculate spin transfer observables for different isotopic, isobaric and isotonic chains with the inverse kinematics for various kinematic conditions.

2. Investigate the influence of kinematic choices on the spin transfer observables for isotopic chain with the inverse kinematics.

3. Check the influence of effective masses on the the spin transfer observables for isotopic chain with the inverse kinematics.

4. Using a general Lorentz representation of NN interaction which is known as IA2 representation.

5. Inclusion of nuclear distortion effects for the incoming and outgoing channels where NN interaction is parametrized by a general Lorentz representation.

Appendix A

The description of the new RMF code

In order to use relativistic mean field approximation to get numerical results that can be compared with experimental data a new computer program called `KE_RMF`[1] was written. In order to optimize the `KE_RMF` code the f2py package in Python programming language was used. The the f2py package provides one the ability use Fortran speed in Python and run Fortran subroutines in Python. The `KE_RMF` code differs from the previously used RMF codes in that it uses the modern programming language, Python, maintaining the speed of compiled language such as Fortran or C++ and it also incorporates the pairing correlations which are important for the study of exotic nuclei. The `KE_RMF` code solves the system of coupled nonlinear differential equations of Eqs. (2.24 - 2.27) and (2.34 - 2.35) and the normalisation condition Eq. (2.36), in order to obtain nuclear groundstate properties from RMF theory approximation. The procedure used in `KE_RMF` begins with the initial guess for the scalar and vector potential in a Woods-Saxon form. Then a use of Shooting point method is made to solve the Dirac equation Eq. (2.24) iteratively. In the shooting method, we first integrates outward from small r to a predefined match radius r_m (the so-called shooting point), and then integrates inward from large r to r_m. In order to impose the proper boundary conditions the analytic solutions to the equations in the regions of large and small r were used. The solutions are scaled so that g_α is continuous at the shooting point r_m, and the radial wave functions are then normalized to unity, *see* Eq. (2.36). The discontinuity in f_α is taken advantage in order to fine-tune the energy eigenvalue as follows:

$$\delta E_\alpha = -m g_\alpha(r_m)[f_\alpha(r_m^+) - f_\alpha(r_m^-)] \tag{A.1}$$

The shooting method continues until $|\delta E_\alpha|$ is less than a pre-set tolerance value. Once the wave functions for single-particle states and boundstate energies are calculated from Woods-Saxon-shaped meson fields. The scalar and vector densities calculated from these wave functions are utilised as sources for the meson and electromagnetic fields and, in turn, the meson and electromagnetic fields determine the mean-field potentials for the nucleons. The Green functions techniques are utilised to produce new meson fields. The iterative procedure continues until self-consistency is obtained. Since the code was developed with specific intention of studying exotic nuclei it was important to also incorporates the pairing correlations which contribute significantly in open shell nuclei[99]. Pairing correlations emanates from a short range part of the nucleon-nucleon interaction. The Bardeen-Cooper-Schrieffer (BCS) model under constant gap approximation is preferred for including pairing correlations within RMF theory. The occupation numbers n_α was introduced to the sums of Eqs.

[1] KE in the codename are initials of names: Kanting Evidence

(2.37 - 2.40) to deal with pairing for open shell nuclei. When there are pairing correlations, $n_\alpha = 1$ for occupied levels and zero for unoccupied levels. The occupation numbers n_α is given by [100, 63]:

$$n_\alpha = \frac{1}{2}\left(1 - \frac{\epsilon_\alpha - \lambda}{(\epsilon_\alpha - \lambda)^2 + \Delta^2}\right) \tag{A.2}$$

where ϵ_α denotes the single-particle energy. The Fermi energy λ for protons (neutrons) is given by:

$$\sum_\alpha n_\alpha = Z(N), \tag{A.3}$$

and the sum is taken over proton (neutron) states. The occupation probability and the unoccupation probability are given by $n_\alpha = v^2$ and $u_\alpha^2 = 1 - v_\alpha^2$, respectively. The constant gap parameter is computed with the five-point formula:

$$\Delta = -\frac{1}{8}[M(N+2) - 4M(N+1) + 6M(N) - 4M(N-1) + M(N-2)], \tag{A.4}$$

where $M(N)$ is the atomic mass of a nucleus with N neutrons and Z protons.

For the nuclei studied in Chapter 2 using a the newly written code, `KE_RMF`, all integrations were performed for nuclear radius of 16 fm and a stepsize of 0.01 fm. The set of a couple differential equations were solved for a shooting point of 2 fm using a fourth-order Runge-Kutta algorithm. For a convergence criterion a tolerance level of 0.001 MeV was set on all single-particle energy levels. The total energy of system E was calculated using the following expression:

$$E = \sum_{\alpha_{occ}} \epsilon_\alpha (2j_\alpha + 1) - \frac{1}{2}\int d\vec{r}\big[- g_s\phi_0(r)\rho_s(r) + g_v V_0(r)\rho_B(r) + g_\rho b_0(r)\rho_3(r) + eA_0(r)\rho_p(r)\big] \tag{A.5}$$

A series of numerical checks was performed to ensure that the newly developed code was properly implemented this included comparing the our results to experimental data such as binding energy per nucleon and nuclear radii data. The binding energy can easily be calculated from the total energy of the system in Eq (A.5). Note that in this work we use the NL3 and FSUGold parameter sets which are listed in Table 2.2. However, other parameter sets of Walecka-inspired relativistic mean field theory models such as QHD-I,QHD-II, NL-1 can also be used in `KE_RMF` code.

Appendix B

Reaction Mechanism

The $(p, 2p)$ proton-induced knockout reactions are nuclear reactions of the form $A(a, a'b')$ in which an incoming proton a interacts with a boundstate nucleon in a target nucleus and knocks out this nucleon, generating a one-hole state in the residual nucleus. This reaction process is most dominant in the intermediate energy regime (100 - 1000 MeV). In this energy regime, the effect of the absorption of incident proton in the nuclear medium is minimal. Therefore, we can assume that the interaction is between the incident proton and bound proton. Furthermore, there is no violent interaction between incident proton and spectator nucleons of the residual nucleus. This kind of reaction differs from free scattering reaction by the binding aspect of probed (bound) nucleon as the separation energy is required to free a bound nucleon. In the free scattering process, the entire energy of the incident proton is available as the kinetic energy of the two outgoing protons (scattered and knocked out). $A(a, a'b')$ knockout reactions are important for the studies of the single-particle properties of a nucleus such as the shell structure and the effects on the bound nucleons. These nuclear reactions can be utilised to investigate nuclear information such as separation energies, spectroscopic factors, medium effects and nuclear distortions.

There is a one-hole state in a particular energy level in the residual nucleus left by ejected nucleon. If this hole is in the level below Fermi surface, the residual nucleus acquires an additional excitation energy corresponding to the energy of this single-particle state relative to the Fermi level. The conservation energy principle can be applied to the reaction depicted in Fig. B.1 and the binding energy B_N of state occupied the bound nucleon in stationary nucleus is:

$$B_N = S_N + E_C = T_a - T_{a'} + T_{b'} + T_C \tag{B.1}$$

In Eq. (B.1) $S_N = (m_A - m_C - m_N)c^2$ is the separation energy required to free a bound nucleon from the target nucleus. The quantities m_A, m_C, and m_N denotes are the masses of the target, residual nucleus $(A-1)$ and the ejected nucleon N, respectively. The kinetic energies of incoming proton a, scattered proton, ejected proton and residual nucleus are denoted by T_a, $T_{a'}$, $T_{b'}$ and T_C, respectively.

The binding energy of the individual state of the nucleon is an important quantity but equally important internal momentum of individual state inside the nucleus. The internal momentum of a specific state inside the nucleus can be determined upon applying the conservation of momentum principle on the $(p, 2p)$ knockout reaction depicted in Fig. B.1

$$\vec{k}_{A-1} = \vec{k}_a - \vec{k}_{a'} - \vec{k}_{b'} = -\vec{k}_C \tag{B.2}$$

It clear from Eq. (B.2) that the internal momentum of nucleon is associated with the momentum of the residual nucleus taken with negative sign. The internal momentum of the nucleon can be determined in two ways:

- Via measurements of momenta of all participants in the reaction.
- Via detection of the recoil momentum residual nucleus.

The simplified picture above is generally accepted but significant modifications are required for the inclusion of initial and final interactions. We provide a complete complete derivation of kinematics of the knockout reaction $A(a, a'b')B$ for both direct and inverse kinematics. In section B.1 we present the direct kinematics for a reaction of the form $A(a, a'b')B$ in both laboratory frame centre of mass frame. In section B.1 we present the derivation for kinematics for a reaction of the form $A(a, a'b')B$ in both laboratory frame centre of mass frame. Note that reaction mechanism presented above is applicable to knockout reaction $A(a, a'b')B$ for inverse kinematics wherein the role of incident proton and target nucleus are reversed. Section B.2 presents the derivation for the $A(a, a'b')B$ knockout reaction with the inverse kinematics.

B.1 Direct Kinematics Derivation

We now derive the direct kinematics for the knockout nuclear reaction of the form $A(a, a'b')B$. In this derivation will discuss both laboratory and centre of mass dynamics. We begin the derivation by looking at the scattering diagram for direct kinematics in the laboratory frame:

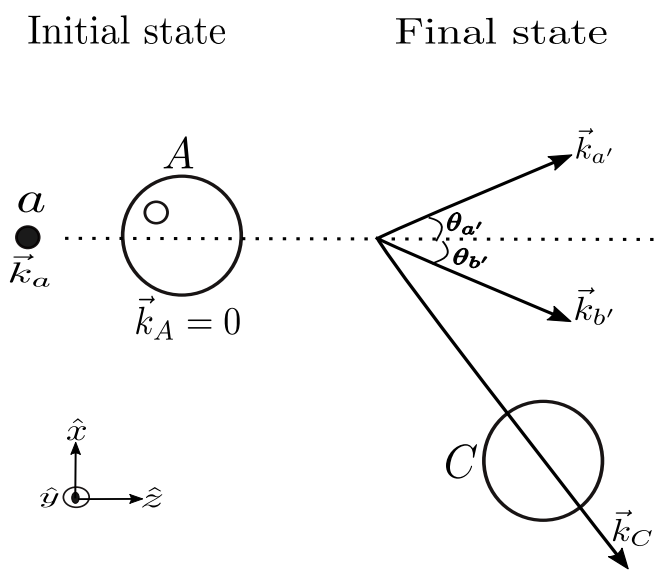

Figure B.1: The diagram depicting a quasifree scattering reaction $A(a, a'b')B$ with direct kinematics in the laboratory frame.

Start with 4-momentum conservation:

$$E_a + m_A = E_{a'} + E_{b'} + E_C, \tag{B.3}$$

$$\vec{k}_a = \vec{k}_{a'} + \vec{k}_{b'} + \vec{k}_C \tag{B.4}$$

where

$$E_a = T_a + m, \qquad m \equiv \text{proton mass} \tag{B.5}$$
$$E_{a'} = T_{a'} + m, \tag{B.6}$$

The quantity T_a is the initial kinetic energy of the incident proton in the laboratory frame. Note that all kinematical quantities are a function of the kinetic energy of the outgoing nucleon $T_{a'}$.

With,

$$|\vec{k}_a| = k_a = \sqrt{E_a^2 - m^2}, \tag{B.7}$$
$$|\vec{k}_{a'}| = k_{a'} = \sqrt{E_{a'}^2 - m^2}. \tag{B.8}$$

If we look at Eq. (B.3), the we see that $E_{b'}$ and E_C still unknown quantities. In Eq. (B.4) $E_{b'}$ and E_C are unknown. We are going to set up an equation for $k_{b'}$.

From Eq. (B.4)

$$\vec{k}_C = \vec{k}_a - \vec{k}_{a'} - \vec{k}_{b'}, \tag{B.9}$$
$$\vec{k}_C^2 = (\vec{k}_a - \vec{k}_{a'} - \vec{k}_{b'})(\vec{k}_A - \vec{k}_{a'} - \vec{k}_{b'}), \tag{B.10}$$
$$= \left[\vec{k}_a - (\vec{k}_{a'} + \vec{k}_{b'})\right]^2, \tag{B.11}$$
$$= \vec{k}_a^2 + (\vec{k}_{a'} + \vec{k}_{b'})^2 - 2\vec{k}_a \cdot (\vec{k}_{a'} + \vec{k}_{b'}) \tag{B.12}$$
$$= \vec{k}_a^2 + \vec{k}_{a'}^2 + \vec{k}_{b'}^2 + 2\vec{k}_a \cdot \vec{k}_{b'} - 2\vec{k}_a \cdot (\vec{k}_{a'} + \vec{k}_{b'}), \tag{B.13}$$
$$= k_a^2 + k_{a'}^2 + k_{b'}^2 - 2k_a k_{a'} \cos(\theta_{a'}) - 2k_a k_{b'} \cos(\theta_{b'}) + 2k_a k_{b'} \cos(\theta_{a'} + \theta_{b'}) \tag{B.14}$$

From Eq. (B.3)

$$E_a - E_{a'} + m_A - E_{b'} = E_C \tag{B.15}$$

$$E_a - E_{a'} + m_A - \sqrt{\vec{k}_{b'}^2 + m^2} = \sqrt{k_C^2 + m_C^2} \tag{B.16}$$

Let

$$C_1 = E_a - E_{a'} + m_A \tag{B.17}$$

$$C_1 - \sqrt{k_{b'}^2 + m^2} = \sqrt{k_C^2 + m_C^2} \tag{B.18}$$

Square Eq. (B.18)

$$\left[C_1 - \sqrt{k_{b'}^2 + m^2}\right]^2 = k_C^2 + m_C^2 \tag{B.19}$$

$$C_1^2 + k_{b'}^2 + m^2 - 2C_1\sqrt{\vec{k}_{b'}^2 + m^2} = k_C^2 + m_C^2, \tag{B.20}$$

$$= k_a^2 + k_{a'}^2 + k_{b'}^2 - 2k_a k_{a'}\cos(\theta_{a'}) - 2k_a k_{b'}\cos(\theta_{b'}) + 2k_{a'}k_{b'}\cos(\theta_{a'} + \theta_{b'}) + m_C^2. \tag{B.21}$$

$$C_1^2 + \cancel{k_{b'}^2} + m^2 - 2C_1\sqrt{\vec{k}_{b'}^2 + m^2} = \cancel{k_{b'}^2} + k_{b'}\left[2k_{a'}\cos(\theta_{a'}+\theta_{b'}) - 2k_a\cos(\theta_{b'})\right] + k_a^2 + k_{a'}^2 - 2k_a k_{a'}\cos(\theta_{a'}) + m_C^2 \tag{B.22}$$

$$-2C_1\sqrt{\vec{k}_{b'}^2 + m^2} = k_{b'}\left[2k_{a'}\cos(\theta_{a'} + \theta_{b'}) - 2k_a\cos(\theta_{b'})\right] + k_a^2 + k_{a'}^2 - 2k_a k_{a'}\cos(\theta_{a'}) + m_C^2 - m^2 - C_1 \tag{B.23}$$

Let

$$C_2 = k_a^2 + k_{a'}^2 - 2k_a k_{a'}\cos(\theta_{a'}) - C_1^2 + m_C^2 - m^2, \tag{B.24}$$

$$C_3 = 2k_{a'}\cos(\theta_{a'} + \theta_{b'}) - 2k_a\cos(\theta_{b'}) \tag{B.25}$$

$$-2C_1\sqrt{k_{b'}^2 + m^2} = C_3 k_{b'} + C_2 \tag{B.26}$$

Square Eq. (B.26)

$$4C_1(k_{b'}^2 + m^2) = C_3^2 k_{b'}^2 + C_2^2 + 2C_2 C_3 k_{b'} \tag{B.27}$$

$$k_{b'}^2[4C_1^2 - C_3^2] + k_{b'}[-2C_2C_3] + [4m^2C_1^2 - C_2^2] = 0 \tag{B.28}$$

Let

$$A = 4C_1^2 - C_3^2, \tag{B.29}$$

$$B = -2C_2C_3, \tag{B.30}$$

$$C = 4m^2C_1^2 - C_2^2 \tag{B.31}$$

$$Ak_{b'}^2 + Bk_{b'} + C = 0 \tag{B.32}$$

Hence

$$k_{b'} = \frac{-B \pm \sqrt{\Delta}}{2A} \tag{B.33}$$

where

$$\Delta = B^2 - 4AC. \tag{B.34}$$

From Eq. (B.33), we can deduce the magnitude of $\vec{k}_{b'}$.
Then

$$E_{b'} = \sqrt{k_{b'}^2 - m} \tag{B.35}$$

and

$$T_{b'} = E_{b'} - m \tag{B.36}$$

$$E_C = E_a - E_{a'} + m_A - E_{b'} \tag{B.37}$$

Then

$$T_C = E_C - m_C \tag{B.38}$$

and

$$k_C = \sqrt{E_C^2 - m_C^2} \tag{B.39}$$

To determine the angles of the residual nucleus, we look at the Cartertian components:
From Eq. (B.4)

$$\vec{k}_a = \vec{k}_{a'} + \vec{k}_{b'} + \vec{k}_C \tag{B.40}$$

We have

$$\begin{aligned}
\vec{k}_a &= k_a \hat{z}, && \text{(B.41)}\\
\vec{k}_{a'} &= k_{a'} \cos(\theta_{a'}) \hat{z} + k_{a'} \sin(\theta_{a'}) \hat{x}, && \text{(B.42)}\\
\vec{k}_{b'} &= k_{b'} \cos(\theta_{b'}) \hat{z} - k_{b'} \sin(\theta_{b'}) \hat{x}, && \text{(B.43)}\\
\vec{k}_C &= k_C \cos(\theta_C) \hat{z} - k_{a'} \sin(\theta_C) \hat{x} && \text{(B.44)}
\end{aligned}$$

Calculation of the three momenta

$$\vec{k}_A = \vec{k}_{a'} + \vec{k}_{b'} + \vec{k}_C \tag{B.45}$$

$\hat{z}$:

$$k_a = k_{a'} \cos(\theta_{a'}) + k_{b'} \cos(\theta_{b'}) + k_C \cos(\theta_C) \tag{B.46}$$

Therefore:

$$\cos(\theta_C) = \frac{k_a - k_{a'} \cos(\theta_{a'}) - k_{b'} \cos(\theta_{b'})}{k_C} \tag{B.47}$$

$\hat{x}$:

$$0 = k_{a'} \sin(\theta_{a'}) - k_{b'} \sin(\theta_{b'}) - k_C \sin(\theta_C), \tag{B.48}$$

$$\sin(\theta_C) = \frac{k_{a'} \sin(\theta_{a'}) - k_{b'} \sin(\theta_{b'})}{k_C} \tag{B.49}$$

Momentum of residual nucleus:

$$\vec{k}_{mis} = -\vec{k}_C. \tag{B.50}$$

Now we need to transform to the centre of mass frame. Laboratory frame:
Consider now the A-a center of mass:

Before the collision we can write

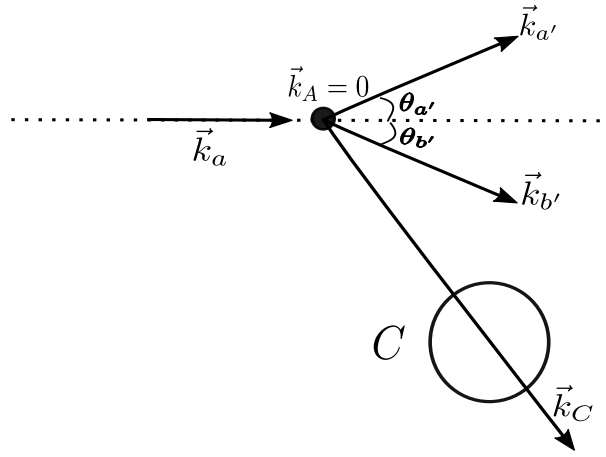

Figure B.2: The diagram depicting a quasifree scattering reaction $A(a, a'b')B$ with direct kinematics in the laboratory frame.

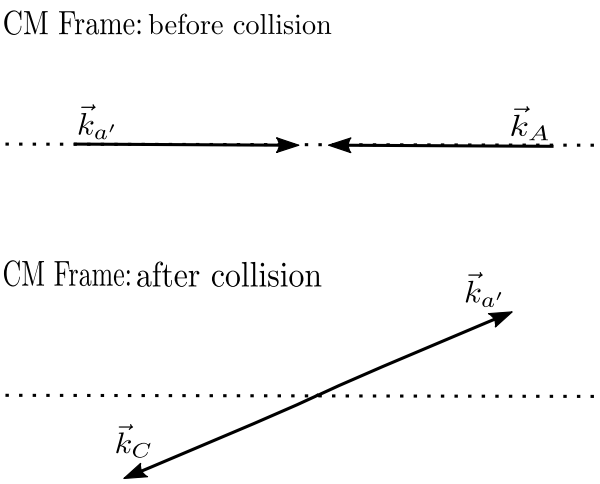

Figure B.3: The diagram depicting a quasifree scattering reaction $A(a, a'b')B$ with direct kinematics in the laboratory frame.

$$s = (k_a + k_A)^2 \tag{B.51}$$

This quantity is Lorentz-invariant and can be evaluated in two frames in two frames: (i) laboratory and (ii) centre of mass

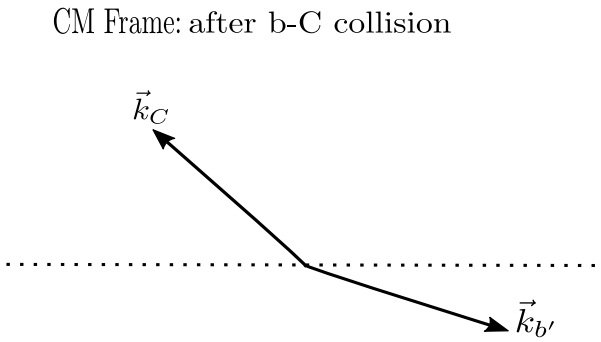

Figure B.4: The diagram depicting a centre of mass frame after b-C collision

$$
\begin{aligned}
s &= (k_a + k_A)^2 && \text{(B.52)}\\
&= k_a^2 + k_A^2 + 2k_a \cdot k_A, && \text{(B.53)}\\
&= m^2 + m_A^2 + 2k_a \cdot k_A \equiv \text{general expression for } s \text{ if both particles are on-shell.} && \text{(B.54)}
\end{aligned}
$$

In the laboratory frame:

$$\vec{k}_a \neq 0 \qquad \& \qquad \vec{k}_A = 0 \tag{B.55}$$

Hence

$$
\begin{aligned}
s &= m^2 + m_A^2 + 2E_a E_A - 2\vec{k}_a \cdot \underbrace{\vec{k}_A}_{=0} && \text{(B.56)}\\
&= m^2 + m_A^2 + 2E_a m_A, && \text{(B.57)}
\end{aligned}
$$

where $E_a \equiv$ total laboratory energy of incident proton. *See* Eq. (B.5). Let us now evaluate Eq. (B.54) in the centre of mass frame:

$$
\begin{aligned}
s &= m^2 + m_A^2 + 2E_a E_A - 2\vec{k}_a \cdot \vec{k}_A, && \text{(B.58)}\\
&= m^2 + m_A^2 + 2E_{a,cm} E_{A,cm} - 2\vec{k}_{a,cm} \cdot (-\vec{k}_{a,cm}), && \text{(B.59)}\\
&= m^2 + m_A^2 + 2E_{a,cm} E_{A,cm} + 2\vec{k}_{a,cm}^2 && \text{(B.60)}\\
&= m^2 + m_A^2 + 2\sqrt{\vec{k}_{a,cm}^2 + m^2}\sqrt{\vec{k}_{a,cm}^2 + m_A^2} + 2\vec{k}_{a,cm}^2 && \text{(B.61)}
\end{aligned}
$$

Therefore

$$
\begin{aligned}
2\sqrt{\vec{k}_{a,cm}^2 + m^2}\sqrt{\vec{k}_{a,cm}^2 + m_A^2} &= \underbrace{s - m^2 - M_A^2}_{A} - 2\vec{k}_{a,cm}^2 \\
&= A - 2k_{A,cm}^2
\end{aligned}
\tag{B.62}
$$

Square Eq. (B.62)

$$4(\vec{k}^2_{a,cm}+m^2)(\vec{k}^2_{a,cm}+m_A^2) \quad = \quad A^2+4\vec{k}^4_{a,cm}-4A\vec{k}^2_{a,cm} \tag{B.63}$$

$$\cancel{4\vec{k}^4_{a,cm}}+4m^2\vec{k}^2_{a,cm}+4m_A^2\vec{k}^2_{a,cm}+4m^2m_A^2=A^2+\cancel{4\vec{k}^4_{a,cm}}-4A\vec{k}^2_{a,cm} \tag{B.64}$$

$$\vec{k}^2_{a,cm}[\underbrace{4m^2+4m_A^2+4A}_{4s}]=A^2-4m^2m_A^2 \tag{B.65}$$

Since

$$\begin{aligned} 4m^2+4m_A^2+4A &= 4m^2+4m_A^2+4s-4m^2-4m_A^2, & \text{(B.66)}\\ &= 4s. & \text{(B.67)}\end{aligned}$$

$$(4s)\vec{k}_{a,cm}=\left(s-m^2+m_A^2\right)^2-4m^2m_A^2 \tag{B.68}$$

$$k_{a,cm}=\frac{1}{2\sqrt{s}}\left[\left(s-m^2+m_A^2\right)^2-4m^2m_A^2\right]^{\frac{1}{2}} \tag{B.69}$$

$$s = Eq.(B.57)$$

After the collision we can define a quantity:

$$s_{a'C}=(k_{a'}+k_C)^2 \qquad \text{This is an invariant quantity. It can be evaluated in any frame.} \tag{B.70}$$

The evaluation of Eq. (B.70) will proceed along exactly the same lines as Eq. (B.54) in the centre of mass frame. Since

$$\vec{k}_C=-\vec{k}_{a'} \tag{B.71}$$

Hence, we can say:

$$k_{a',cm}=\frac{1}{2\sqrt{s_{a'C}}}\left[\left(s_{a'C}-m^2-m_C^2\right)^2-4m^2m_C^2\right]^{\frac{1}{2}} \tag{B.72}$$

Where we need to now evaluate $s_{a'C}$ in the laboratory frame:

$$\begin{aligned} s_{a'C} &= m^2+m_C^2+2k_{a'}\cdot k_C & \text{(B.73)}\\ &= m^2+m_C^2+2E_{a'}E_C-2\vec{k}_{a'}\cdot\vec{k}_C \qquad \text{lab frame,} & \text{(B.74)}\\ &= m^2+m_C^2+2E_{a'}E_C-2k_{a'}k_C\cos(\theta_{a'C}) & \text{(B.75)}\end{aligned}$$

Where $\theta_{a'C} \equiv$ laboratory angle between a' and C. $\longrightarrow$ *See* Eq. (B.84).

$$\begin{aligned} E_{a'} &= \text{Eq. (B.6)}, & \text{(B.76)}\\ E_C &= \text{Eq. (B.37)}, & \text{(B.77)}\\ k_{a'} &= \text{Eq. (B.8)}, & \text{(B.78)}\\ k_C &= \text{Eq. (B.39)}. & \text{(B.79)}\end{aligned}$$

We will need to calculate $\theta_{a'C}$
We know that

$$\begin{aligned}
\vec{k}_{a'} \cdot \vec{k}_C &= k_{a'} k_C \cos(\theta_{a'C}), && \text{(B.80)}\\
&= (\vec{k}_{a'})_x (\vec{k}_C)_x + (\vec{k}_{a'})_z (\vec{k}_C)_z && \text{(B.81)}\\
&= (k_{a'} \sin(\theta_{a'}))(-k_C \sin(\theta_C)) + (k_{a'} \cos(\theta_{a'}))(k_C \cos(\theta_C)) && \text{(B.82)}\\
&= k_{a'} k_C \big[\cos(\theta_{a'})(\cos(\theta_C) - \sin(\theta_{a'})(\sin(\theta_C)\big] && \text{(B.83)}
\end{aligned}$$

Therefore:

$$\cos(\theta_{a'C}) = \cos(\theta_{a'}) \cos(\theta_C) - \sin(\theta_{a'}) \sin(\theta_C) \tag{B.84}$$

where

$$\begin{aligned}
\cos(\theta_C) &= \text{Eq. (B.49)}, && \text{(B.85)}\\
\sin(\theta_C) &= \text{Eq. (B.47)}. && \text{(B.86)}
\end{aligned}$$

After collision we define

$$s_{b'C} = (k_{b'} + k_C)^2 \tag{B.87}$$

For $s_{a'C}$ we will define

$$k_{b',cm} = \frac{1}{2\sqrt{s_{b'C}}} \Big[\left(s_{b'C} - m^2 - m_C^2\right)^2 - 4m^2 m_C^2 \Big]^{\frac{1}{2}} \tag{B.88}$$

where

$$s_{b'C} = m^2 + m_C^2 + 2E_b E_C - 2k_b k_C \cos(\theta_{b'C}) \tag{B.89}$$

with

$$\begin{aligned}
E_{b'} &= \text{Eq. (B.35)}, && \text{(B.90)}\\
E_C &= \text{Eq. (B.37)}, && \text{(B.91)}\\
k_{b'} &= \text{Eq. (B.33)}, && \text{(B.92)}\\
k_C &= \text{Eq. (B.39)}, && \text{(B.93)}
\end{aligned}$$

$$\begin{aligned}
\vec{k}_{b'} \cdot \vec{k}_C &= (\vec{k}_{b'})_x (\vec{k}_C)_x + (\vec{k}_{b'})_z (\vec{k}_C)_z && \text{(B.94)}\\
&= (-k_{b'} \sin(\theta_{b'}))(-k_C \sin(\theta_C)) + (k_{b'} \cos(\theta_{b'}))(k_C \cos(\theta_C)) && \text{(B.95)}\\
&= k_{b'} k_C \left[\cos(\theta_{b'})(\cos(\theta_C) + \sin(\theta_{b'})(\sin(\theta_C)\right] && \text{(B.96)}
\end{aligned}$$

Therefore:

$$\cos(\theta_{b'C}) = \cos(\theta_{b'}) \cos(\theta_C) - \sin(\theta_{b'}) \sin(\theta_C) \tag{B.97}$$

where

$$\cos(\theta_C) = \text{Eq. (B.47)}, \tag{B.98}$$
$$\sin(\theta_C) = \text{Eq. (B.49)}. \tag{B.99}$$

We wrote a python code, `DirectKine`, to compute the kinematics for a nuclear reaction of the form $A(a, a'b')B$ in the direct kinematics. In Fig. B.5 below, the flowchart illustrates how `DirectKine` calculates the kinematics for the $A(a, a'b')B$. In this work `DirectKine` was used for the kinematics of the $(p, 2p)$ knockout reaction. However, `DirectKine` can be used for any knockout reaction of the form $A(a, a'b')B$. For instance, where incident nucleon or alpha particle knocks out a nucleon or cluster from a target nucleus.

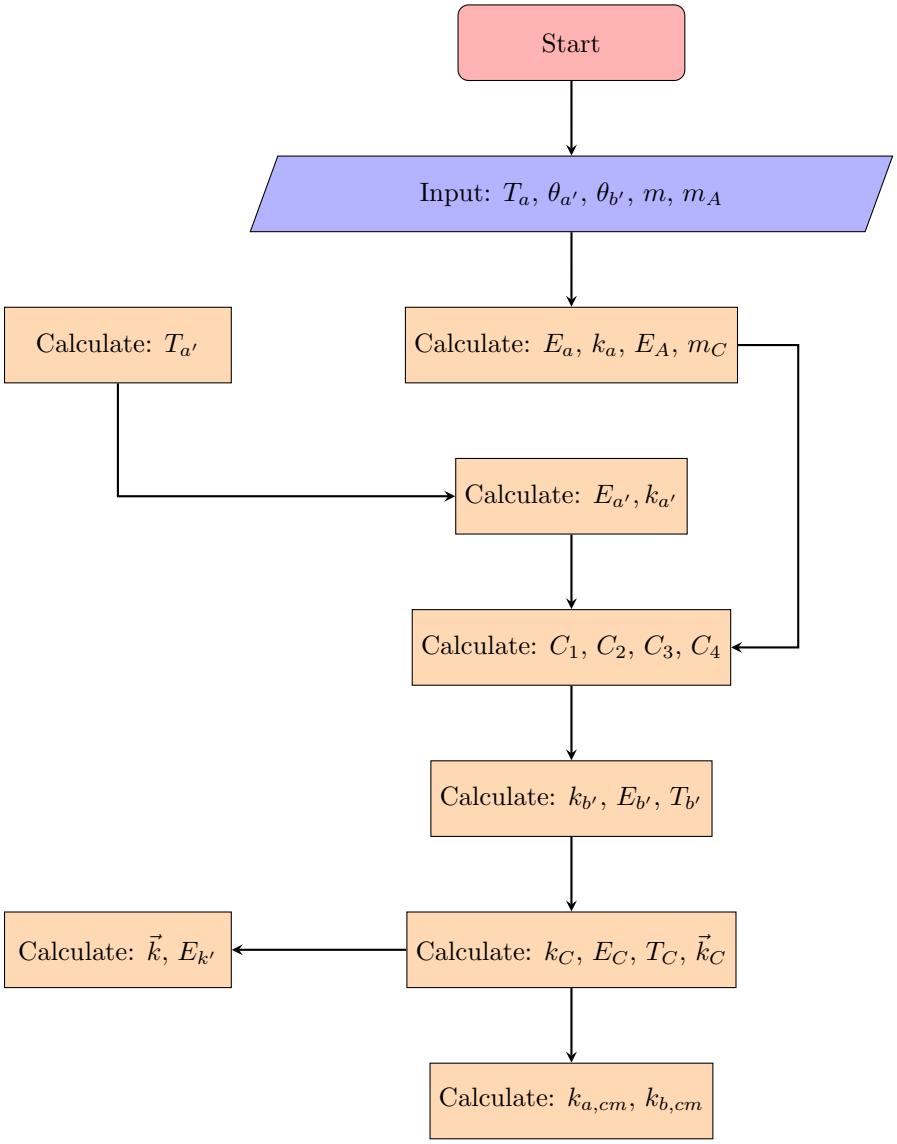

Figure B.5: The flowchart illustrates how our code calculates the kinematics for the $A(a, a'b')B$ nuclear reaction.

B.2 Inverse Kinematics Derivation

In this section, we will derive the following:

- Lab kinematics for the inverse reaction
- CM kinematics for the inverse reaction

The scattering diagram for inverse kinematics in the LAB frame is shown in Fig. B.6

$$A + \mathrm{p} \longrightarrow 2\mathrm{p} + A - 1 \tag{B.100}$$

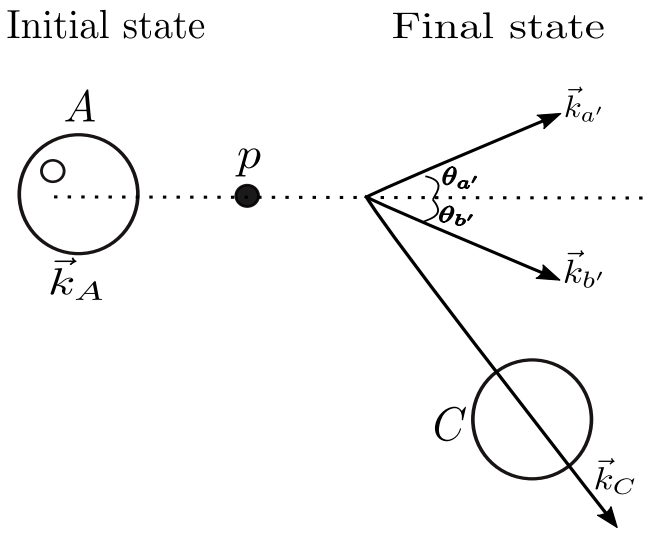

Figure B.6: The diagram depicting a quasifree scattering reaction $A(a, a'b')B$ with inverse kinematics in the laboratory frame.

The separation energy of a nucleon inside the nucleus is given by:

$$S = T_a - (T_{a'} + T_{b'} + T_C) \tag{B.101}$$

The momentum of the knocked out nucleon from inside the nucleus is written as:

$$\vec{k}_{mis} = -\vec{k}_C \tag{B.102}$$

Start with 4-momentum conservation:

$$E_A + m = E_{a'} + E_{b'} + E_C, \tag{B.103}$$

$$\vec{k}_A = \vec{k}_{a'} + \vec{k}_{b'} + \vec{k}_C \tag{B.104}$$

where

$$E_A = T_A + m_A, \tag{B.105}$$
$$E_{a'} = T_{a'} + m, \tag{B.106}$$
$$|\vec{k}_A| = k_A = \sqrt{E_A^2 - m_A^2} \tag{B.107}$$
$$|\vec{k}_{a'}| = k_{a'} = \sqrt{E_{a'}^2 - m^2} \tag{B.108}$$

Now we follow name procedure as in section B.1 to derive an equation for $k_{b'}$.
From Eq. (B.104)

$$\vec{k}_C = \vec{k}_A + \vec{k}_{a'} - \vec{k}_{b'}, \tag{B.109}$$
$$\vec{k}_C^2 = (\vec{k}_A + \vec{k}_{a'} - \vec{k}_{b'})(\vec{k}_A + \vec{k}_{a'} - \vec{k}_{b'}), \tag{B.110}$$
$$= \left[\vec{k}_A - (\vec{k}_{a'} + \vec{k}_{b'})\right]^2, \tag{B.111}$$
$$= \vec{k}_A^2 + \left(\vec{k}_{a'} + \vec{k}_{b'}\right)^2 - 2\vec{k}_A \cdot \left(\vec{k}_{a'} + \vec{k}_{b'}\right), \tag{B.112}$$
$$= \vec{k}_A^2 + \vec{k}_{a'}^2 + \vec{k}_{b'}^2 + 2\vec{k}_{a'} \cdot \vec{k}_{b'} - 2\vec{k}_A \cdot \vec{k}_{a'} - 2\vec{k}_A \cdot \vec{k}_{b'}. \tag{B.113}$$

From Eq. (B.103)

$$E_A + m = E_{a'} + \sqrt{\vec{k}_{b'}^2 + m^2} + \sqrt{\vec{k}_C^2 + m_C^2} \tag{B.114}$$

$$E_A - E_{a'} + m - \sqrt{\vec{k}_{b'}^2 + m^2} = \sqrt{\vec{k}_C^2 + m_C^2} \tag{B.115}$$

Let

$$C_1 = E_A - E_{a'} + m \tag{B.116}$$

$$C_1 - \sqrt{\vec{k}_{b'}^2 + m^2} = \sqrt{\vec{k}_C^2 + m_C^2} \tag{B.117}$$

Square Eq. (B.117)

$$\left[C_1 - \sqrt{\vec{k}_{b'}^2 + m^2}\right]^2 = \vec{k}_C^2 + m_C^2 \tag{B.118}$$

$$C_1^2 + \cancel{k_{b'}^2} + m^2 - 2C_1\sqrt{\vec{k}_{b'}^2 + m^2} = \vec{k}_A^2 + \vec{k}_{a'}^2 + \cancel{\vec{k}_{b'}^2} + 2k_{a'}k_{b'}\cos(\theta_{a'b'}) - 2k_Ak_{a'}\cos(\theta_{Aa'}) - 2k_Ak_{b'}\cos(\theta_{Ab'}) \tag{B.119}$$

$$-2C_1\sqrt{k_{b'}^2 + m^2} = k_A^2 + k_{a'}^2 - 2k_Ak_{a'}\cos(\theta_{a'}) - 2k_Ak_{b'}\cos(\theta_{b'}) + 2k_{a'}k_{b'}\cos(\theta_{a'} + \theta_{b'}) + m_C^2 - m^2 - C_1^2 \tag{B.120}$$

Let

$$C_2 = k_A^2 + k_{a'}^2 - 2k_Ak_{a'}\cos(\theta_{a'}) - C_1^2 + m_C^2 - m^2, \tag{B.121}$$
$$C_3 = 2k_{a'}\cos(\theta_{a'} + \theta_{b'}) - 2k_A\cos(\theta_{b'}) \tag{B.122}$$

$$-2C_1\sqrt{k_{b'}^2+m^2} = C_2 + C_2 k_{b'} \tag{B.123}$$

Square Eq. (B.123),

$$4C_1(k_{b'}^2+m^2) = C_3^2 k_{b'}^2 + 2C_2C_3k_{b'} + C_2^2 \tag{B.124}$$

$$k_{b'}^2[4C_1^2 - C_3^2] + k_{b'}[-2C_2C_3] + 4m^2C_1^2 - C_2^2 = 0 \tag{B.125}$$

Let

$$\begin{aligned} A &= 4C_1^2 - C_3^2 && \text{(B.126)}\\ B &= -2C_2C_3, && \text{(B.127)}\\ C &= 4m^2C_1^2 - C_2^2. && \text{(B.128)} \end{aligned}$$

$$Ak_{b'}^2 + Bk_{b'} + C = 0 \tag{B.129}$$

Hence

$$k_{b'} = \frac{-B \pm \sqrt{\Delta}}{2A} \tag{B.130}$$

Where

$$\Delta = B^2 + 4AC \tag{B.131}$$

From Eq. (B.130)

$$E_{b'} = \sqrt{(k_{b'}^2 - m^2)} \tag{B.132}$$

and

$$T_{b'} = E_{b'} - m \tag{B.133}$$

From Eq. (B.103)

$$E_C = E_A - E_{a'} + m - E_{b'} \tag{B.134}$$

Then

$$T_C = E_C - m_C \tag{B.135}$$

and

$$k_C = \sqrt{E_C^2 - m_C^2} \tag{B.136}$$

To determine the angles of the residual nucleus, we look at the Cartesian components:

$$\begin{aligned} \vec{k}_A &= k_A\hat{z}, && \text{(B.137)}\\ \vec{k}_{a'} &= k_{a'}\cos(\theta_{a'})\hat{z} + k_{a'}\sin(\theta_{a'})\hat{x}, && \text{(B.138)}\\ \vec{k}_{b'} &= k_{b'}\cos(\theta_{b'})\hat{z} - k_{b'}\sin(\theta_{b'})\hat{x}, && \text{(B.139)}\\ \vec{k}_C &= k_C\cos(\theta_C)\hat{z} - k_C\sin(\theta_C)\hat{x} && \text{(B.140)} \end{aligned}$$

Calculation of the three momenta

$$\vec{k}_A = \vec{k}_{a'} + \vec{k}_{b'} + \vec{k}_C \tag{B.141}$$

$\hat{z}$

$$k_A = k_{a'}\cos(\theta_{a'}) + k_{b'}\cos(\theta_{b'}) + k_C\cos(\theta_C) \tag{B.142}$$

$$\cos(\theta_C) = \frac{k_A - k_{a'}\cos(\theta_{a'}) - k_{b'}\cos(\theta_{b'})}{k_C} \tag{B.143}$$

$\hat{x}$

$$0 = k_{a'}\sin(\theta_{a'}) - k_{b'}\sin(\theta_{b'}) - k_C\sin(\theta_C), \tag{B.144}$$

$$\sin(\theta_C) = \frac{k_{a'}\sin(\theta_{a'}) - k_{b'}\sin(\theta_{b'})}{k_C}. \quad \text{This is same as Eq. B.49} \tag{B.145}$$

Consider now the $A-a$ center of mass:

Define

$$s = (k_A + k_a)^2 \tag{B.146}$$

This quantity is Lorentz-invariant and can be evaluated in the two frames: (i) laboratory and (ii) centre of mass

$$s = k_A^2 + k_a^2 + 2k_A\cdot k_a, \tag{B.147}$$

$$= m_A^2 + m^2 + 2k_A\cdot k_a \tag{B.148}$$

In the laboratory frame: $\vec{k}_a = 0$, hence

$$s = m_A^2 + m^2 + 2E_A m \tag{B.149}$$

In the centre of mass frame:

$$s = m_A^2 + m^2 + 2E_A E_a - 2\vec{k}_{A,cm}\cdot\vec{k}_{a,cm}, \tag{B.150}$$

$$= m_A^2 + m^2 + 2\sqrt{\vec{k}_{A,cm}^2 + m_A^2}\sqrt{\vec{k}_{A,cm}^2 + m^2} - 2\vec{k}_{A,cm}^2 \tag{B.151}$$

$$2\sqrt{\vec{k}_{A,cm}^2 + m_A^2}\sqrt{\vec{k}_{A,cm}^2 + m^2} = \underbrace{s - m_A^2 - m^2}_{} - 2\vec{k}_{a,cm}^2 = A - 2k_{A,cm}^2 \tag{B.152}$$

Square Eq. (B.152)

$$4(\vec{k}_{A,cm}^2 + m_A^2)(\vec{k}_{A,cm}^2 + m^2) = A^2 + 4k_{A,cm}^4 - 4Ak_{A,cm}^2 \tag{B.153}$$

$$\cancel{4k_{A,cm}^4} + 4m^2k_{A,cm}^2 + 4m^2k_{A,cm}^2 + 4m^2m_A^2 = A^2 + \cancel{4k_{A,cm}^4} - 4Ak_{A,cm}^2 \tag{B.154}$$

$$k_{A,cm}^2\left[\underbrace{4m^2+m_A^2+4A}_{4s}\right]=A^2-4m^2m_A^2 \tag{B.155}$$

$$k_{A,cm}=\frac{1}{2\sqrt{s}}\left[(s-m^2-m_A^2)^2-4m^2m_A^2\right]^{\frac{1}{2}} \tag{B.156}$$

$$s=\text{Eq. (B.149)}$$

After the collision, we define a quantity:

$$s_{a'C}=(k_{a'}+k_C)^2 \tag{B.157}$$

The calculation of Eq. (B.157) will proceed along the same lines as Eq. (B.146) since

$$\vec{k}_C=-\vec{k}_{a'} \tag{B.158}$$

Therefore

$$k_{a',cm}=\frac{1}{2\sqrt{s_{a'C}}}\left[s_{a'C}-m^2-m_C^2)^2-4m^2m_A^2\right]^{\frac{1}{2}} \tag{B.159}$$

Where $s_{a'C}$ can be evaluated in the laboratory frame: We find

$$s_{a'C}=m^2+m_C^2+2E_aE_C-2k_ak_C\cos(\theta_{a'C}) \tag{B.160}$$

Where

$$\begin{aligned} E_{a'} &= \text{Eq. (B.106)}, && \text{(B.161)}\\ E_C &= \text{Eq. (B.134)}, && \text{(B.162)}\\ k_{a'} &= \text{Eq. (B.108)}, && \text{(B.163)}\\ k_C &= \text{Eq. (B.136)} && \text{(B.164)} \end{aligned}$$

$$\cos(\theta_{a'C})=\cos(\theta_{a'})\cos(\theta_C)-\sin(\theta_{a'})\sin(\theta_C) \tag{B.165}$$

where

$$\begin{aligned} \cos(\theta_C) &= \text{Eq. (B.143)}, && \text{(B.166)}\\ \sin(\theta_C) &= \text{Eq. (B.145)} && \text{(B.167)} \end{aligned}$$

We define

$$s_{b'C}=(k_{b'}+k_C)^2 \tag{B.168}$$

where we find

$$k_{b',cm}=\frac{1}{2\sqrt{s_{b'C}}}\left[\left(s_{b'C}-m^2-m_C^2\right)^2-4m^2m_C^2\right]^{\frac{1}{2}} \tag{B.169}$$

where

$$E_{b'} = \text{Eq. (B.132)}, \tag{B.170}$$
$$E_C = \text{Eq. (B.134)}, \tag{B.171}$$
$$k_{b'} = \text{Eq. (B.130)}, \tag{B.172}$$
$$k_C = \text{Eq. (B.136)}. \tag{B.173}$$

$$s_{b'C} = m^2 + m_C^2 + 2E_{b'}E_C - 2k_{b'}k_C\cos(\theta_{b'C}) \tag{B.174}$$

$$\cos(\theta_{b'C}) = \cos(\theta_{b'})\cos(\theta_C) - \sin(\theta_{b'})\sin(\theta_C) \tag{B.175}$$

$$\cos(\theta_C) = \text{Eq. (B.143)}, \tag{B.176}$$
$$\sin(\theta_C) = \text{Eq. (B.145)}. \tag{B.177}$$

We wrote a python code, `InverseKine`, to compute the kinematics for a nuclear reaction of the form $A(a, a'b')B$ in the inverse kinematics. `InverseKine` is similar to `DirectKine` hence Fig. B.5 illustrates how `InverseKine` calculates the kinematics for the $A(a, a'b')B$ knockout reaction. Note the roles of incident proton and target are interchanged in `InverseKine`.

Appendix C

The Trace Method

We begin our derivation of the square of invariant transition matrix for the exclusive $(\vec{p}, 2\vec{p})$ using trace methods with the expression, Eq. (3.29), derived in chapter 3:

$$T(s_a, s_{a'}, s_{b'}) = \sum_{L=S}^{T} F_L[U(\vec{k}_{a'}, s_{a'}) \otimes U(\vec{k}_{b'}, s_{b'})](\lambda^L \otimes \lambda_L)[U(\vec{k}_a, s_a) \otimes \mathcal{U}_{LJM_J}(-\vec{K})]. \tag{C.1}$$

The boundstate proton wave function $\mathcal{U}_{LJM_J}(-\vec{K}) = \mathcal{U}_\alpha(-\vec{K})$ is labelled by single-particle quantum numbers L, J, and M_J. The Eq. (C.1) represents the invariant transition matrix element for a two-body scattering process in which the initial proton is bound. We apply the following property of matrices on Eq. (C.1):

$$(A \otimes B)(C \otimes D) = (AC) \otimes (BD) \tag{C.2}$$

to get

$$T(s_a, s_{a'}, s_{b'}) = \sum_{L=S}^{T} F_L[\bar{U}_i(\vec{k}_{a'}, s_{a'})(\lambda^L)_{ij} U_j(\vec{k}_a, s_a)][\bar{U}_k(\vec{k}_{b'}, s_{b'})(\lambda_L)_{kl} \mathcal{U}_{LJM_J}(-\vec{K})_l]. \tag{C.3}$$

Upon taking the complex conjugate of Eq. (C.3) and using the property below

$$[\bar{X}AY]^* = [\bar{X}AY]^\dagger = [\bar{Y}\bar{A}X], \tag{C.4}$$

one gets:

$$T^*(s_a, s_{a'}, s_{b'}) = \sum_{L=S}^{T} F_L^*[(\bar{\mathcal{U}}_\alpha)_r(\bar{\lambda}_L)_{rs}(U_{b'})_s][(\bar{U}_a)_k(\bar{\lambda}^L)_{mn}(U_{a'})_n]. \tag{C.5}$$

The product of Eqs. (C.3) and (C.5) is equal to $|T(s_a, s_{a'}, s_{b'}|^2$ which is the most significant quantity that is needed to compute spin observables of interest in section 3.3

$$
\begin{aligned}
|T(s_a, s_{a'}, s_{b'}|^2 = \sum_{LL'=S}^{T} & F_L F^*_{L'}[\bar{U}_i(\vec{k}_{a'}, s_{a'})(\lambda^L)_{ij} U_j(\vec{k}_a, s_a)][\bar{U}_k(\vec{k}_{b'}, s_{b'})(\lambda_L)_{kl}(\mathcal{U}_\alpha)_l] \\
& \times [(\bar{\mathcal{U}}_\alpha)_r(\bar{\lambda}_L)_{rs} U_s(\vec{k}_{a'}, s_{a'})][(\bar{U}_k(\vec{k}_a, s_a)(\bar{\lambda}^L)_{mn} U_n(\vec{k}_{a'}, s_{a'})], \\
= \sum_{LL'=S}^{T} & F_L F^*_{L'}[U_s(\vec{k}_{a'}, s_{a'})\bar{U}_i(\vec{k}_{a'}, s_{a'})(\lambda^L)_{ij} U_j(\vec{k}_a, s_a)\bar{U}_r(\vec{k}_a, s_a)(\bar{\lambda}^{L'})_{rs}] \\
& \times [U_n(\vec{k}_{b'}, s_{b'})\bar{U}_k(\vec{k}_{b'}, s_{b'})(\lambda_L)_{kl}\{\mathcal{U}_\alpha\bar{\mathcal{U}}_\alpha\}_{lm}(\bar{\lambda}_{L'})_{mn}].
\end{aligned}
\tag{C.6}
$$

The energy projection operator is given by

$$
\sum_s U_\alpha(\vec{k}, s)\bar{U}_\beta(\vec{k}, s) = \left(\frac{\not{k} + m}{2m}\right)_{\alpha\beta}. \tag{C.7}
$$

and the spin projection operator is given by

$$
\hat{\Sigma}(s) = \frac{1 + \gamma_5 \not{s}}{2}. \tag{C.8}
$$

Similarly, the following identity of Dirac spinors holds

$$
\begin{aligned}
\sum_s U_\alpha(\vec{k}, s)\bar{U}_\beta(\vec{k}, s) &= \left(\frac{\not{k} + m}{2m} \cdot \frac{1 + \gamma_5 \not{s}}{2}\right)_{\alpha\beta}, && \text{(C.9)} \\
&= \left(\Lambda_+(k, m)\hat{\Sigma}(\mathbf{i}, s)\right)_{\alpha\beta}. && \text{(C.10)}
\end{aligned}
$$

In a polarized $(p, 2p)$ experiment, the spin projections of particles a and a' are fixed in the entrance and exit channels and spin projections of particles b and b' are left unfixed. In order to fix the spin projections of particles a and a' we use a spin projector $\hat{\Sigma}(s)$ as illustrated below. In accounting for the particles b and b', we the sum over the total angular momentum projection M_b and the spin projection $s_{b'}$. This results in a desired form of matrix element:

$$
\begin{aligned}
\sum_{M_b s_{b'}} |\mathcal{M}|^2 &= \sum_{M_b s_{b'}} \sum_{L,L'}^{T} F_L F^*_{L'} \Big[\Big(\Lambda_+(k_{a'}, m)\hat{\Sigma}(\hat{\mathbf{i}}, s)\Big)_{si}(\lambda^L)_{ij}\Big(\Lambda_+(k_a, m)\hat{\Sigma}(\hat{\mathbf{i}}, s)\Big)_{jr}(\bar{\lambda}^{L'})_{rs})\Big] \\
&\times[(\Lambda_+(k_{b'}, m)_{nk}(\lambda_L)_{kl}(\mathcal{U}_\alpha\bar{\mathcal{U}}_\alpha)_{lm}(\bar{\lambda}_{L'})_{mn}]. && \text{(C.11)}
\end{aligned}
$$

All possible combinations of spin projections over a and a' are represented by indices s_i and s_f, respectively.

$$
\begin{aligned}
\sum_{M_b s_{b'}} |\mathcal{M}|^2 &= \sum_{M_b s_{b'}} \sum_{L,L'}^{T} F_L F^*_{L'} \Big[\Big(\Lambda_+(k_{a'}, m)\hat{\Sigma}(\hat{\mathbf{i}}, s)\Big)_{si}(\lambda^L)_{ij}\Big(\Lambda_+(k_a, m)\hat{\Sigma}(\hat{\mathbf{i}}, s)\Big)_{jr}(\bar{\lambda}^{L'})_{rs})\Big] \\
&\times[(\Lambda_+(k_{b'}, m)_{nk}(\lambda_L)_{kl}(\mathcal{U}_\alpha\bar{\mathcal{U}}_\alpha)_{lm}(\bar{\lambda}_{L'})_{mn}]. && \text{(C.12)}
\end{aligned}
$$

It was in shown Ref. [101] that Casimir trick performed on spinors holds even for bound-state spinors. However, the following identities have to be satisfied:

$$\sum_m \mathcal{Y}_{+km}(\hat{\mathbf{k}})\mathcal{Y}^*_{+km}(\hat{\mathbf{k}}) = \sum_m \mathcal{Y}_{-km}(\hat{\mathbf{k}})\mathcal{Y}^*_{-km}(\hat{\mathbf{k}}), \tag{C.13}$$

$$= \frac{2j+1}{8\pi}, \tag{C.14}$$

$$\sum_m \mathcal{Y}_{+km}(\hat{\mathbf{k}})\mathcal{Y}^*_{-km}(\hat{\mathbf{k}}) = \sum_m \mathcal{Y}_{-km}(\hat{\mathbf{k}})\mathcal{Y}^*_{+km}(\hat{\mathbf{k}}), \tag{C.15}$$

$$= -\frac{2j+1}{8\pi}(\sigma\cdot\hat{\mathbf{k}}). \tag{C.16}$$

With the above identities established, we are now in a position to introduce boundstate propagator[1].

$$S_\alpha(\mathbf{k}) = \frac{1}{2j+1}\sum_\delta(\mathcal{U}_{\alpha\delta}(\mathbf{k})\bar{\mathcal{U}}_{\alpha\delta}(\mathbf{k})), \tag{C.17}$$

$$= \not{k}_\alpha + m_\alpha, \tag{C.18}$$

$$= \frac{(\not{k}_\alpha + m_\alpha)}{2m_\alpha}\times 2m_\alpha, \tag{C.19}$$

$$= 2m_\alpha\Lambda_+(k_\alpha, m_\alpha) \qquad \text{where} \qquad (\alpha = \{E,\kappa\}). \tag{C.20}$$

The mass-, energy- and momentum-like quantities are defined as

$$m_\alpha = M = \left(\frac{\pi}{k^2}\right)\Big[g^2_\alpha(k) - f^2_\alpha(k)\Big], \tag{C.21}$$

$$E_\alpha = M = \left(\frac{\pi}{k^2}\right)\Big[g^2_\alpha(k) + f^2_\alpha(k)\Big], \tag{C.22}$$

$$k_\alpha = M = \left(\frac{\pi}{k^2}\right)\Big[2g_\alpha(k)f_\alpha(k)\hat{\mathbf{k}}\Big], \tag{C.23}$$

which are consistent with the on-shell relation:

$$k^2_\alpha = E^2_\alpha - \mathbf{k}^2_\alpha = m^2_\alpha. \tag{C.24}$$

Note that the similarity between the free and bound propagators enables us to use trace techniques to compute polarization observables for both free and bound nucleons. If the distortions of the bound nucleon are included the simplicity of trace method gets lost, thus, these expressions are only valid when the distortions are not incorporated. The Figs. C.1 and C.2 display the plots of the effective energy-, mass-, momentum-like quantities as a function of momentum for the $1p^{3/2}$ proton and neutron hole states of ^{24}O. From the figures we observe that $E_\alpha \approx m_\alpha \gg k_\alpha$. This emanates from the fact that even though $f_\alpha(k)$ is reinforced in the nuclear medium, it remains to be very dominated by $g_\alpha(k)$.

[1] Note that the α refer to the quantum numbers of the boundstae wavefuntion not the Lorentz index.

Note that cross section and spin observables are directly proportional to the term $k_\alpha + m_\alpha$ in C.19, and since $k_\alpha \ll E_\alpha$ and $k_\alpha \approx E_\alpha$ cross section and spin observables become directly proportional to E_α. This allows us to interpret E_α in Eq. C.21 as a bound-nucleon density in momentum space. Therefore, we can conclude that knockout reactions such as $A(a, a'b')B$ serve as a direct probe of momentum distribution in the bound-nucleon wavefunction.

Finally summing over repeated indices we obtain:

$$\begin{aligned}\sum_{M_b s_{b'}} |\mathcal{M}|^2 &= \sum_{M_b s_{b'}} \sum_{L,L'}^{T} F_L F_{L'}^* \mathrm{Tr}\Big[\Big(\Lambda_+(k_{a'}, m)\hat{\Sigma}(\hat{\mathbf{i}}, s)\Big)(\lambda^L)\Big(\Lambda_+(k_a, m)\hat{\Sigma}(\hat{\mathbf{i}}, s)\Big)(\bar{\lambda}^{L'}))\Big] \\ &\quad \times \mathrm{Tr}[(\Lambda_+(k_{b'}, m)(\lambda_L)(\mathcal{U}_\alpha \bar{\mathcal{U}}_\alpha)(\bar{\lambda}_{L'})]. \end{aligned} \tag{C.25}$$

We can now define hadronic tensor as:

$$H^{LL'}(k_a, k_{a'}, m, s_a, s_{a'}) = \mathrm{Tr}\Big[\Lambda_+(k_{a'}, m)\hat{\Sigma}(\hat{\mathbf{i}}, s_{a'})\lambda^L \Lambda_+(k_a, m)\hat{\Sigma}(\hat{\mathbf{i}}, s_a)\bar{\lambda}^{L'}\Big], \tag{C.26}$$

and target tensor as follows:

$$W_{LL'}(\vec{K}, k_{b'}, m, M_b) = \mathrm{Tr}[(\Lambda_+(k_{b'}, m)(\lambda_L)(\mathcal{U}_\alpha \bar{\mathcal{U}}_\alpha)(\bar{\lambda}_{L'})]. \tag{C.27}$$

The Eq. (C.25) can now be recast in a more compact fashion:

$$\sum_{M_b s_{b'}} |\mathcal{M}|^2 = \sum_{M_b s_{b'}} \sum_{L,L'}^{T} F_L F_{L'}^* H^{LL'}(k_a, k_{a'}, m, s_a, s_{a'}) W_{LL'}(\vec{K}, k_{b'}, m, M_b) \tag{C.28}$$

Here the quantity $H^{LL'}(k_a, k_{a'}, m, s_a, s_{a'})$ is a spin dependent hadronic tensor (also known as projectile tensor), it contains the information about the polarization of the protons in the entrance and exit channels of the exclusive $(\vec{p}, 2\vec{p})$ nuclear reaction. The expression $W_{LL'}(\vec{K}, k_{b'}, m, M_b)$ is the target tensor (response function), it contains information about bound proton in the nucleus. It is evident that all the information about the scattering cross-sections and polarization transfer observables is contained in the hadronic and target tensors. The explicit evaluation of the two expressions $H^{LL'}(k_a, k_{a'}, m, s_a, s_{a'})$ and $W_{LL'}(\vec{K}, k_{b'}, m, M_b)$ is straightforward and not discussed in this work. The interested reader is advised to consult Ref [76] for the procedure.

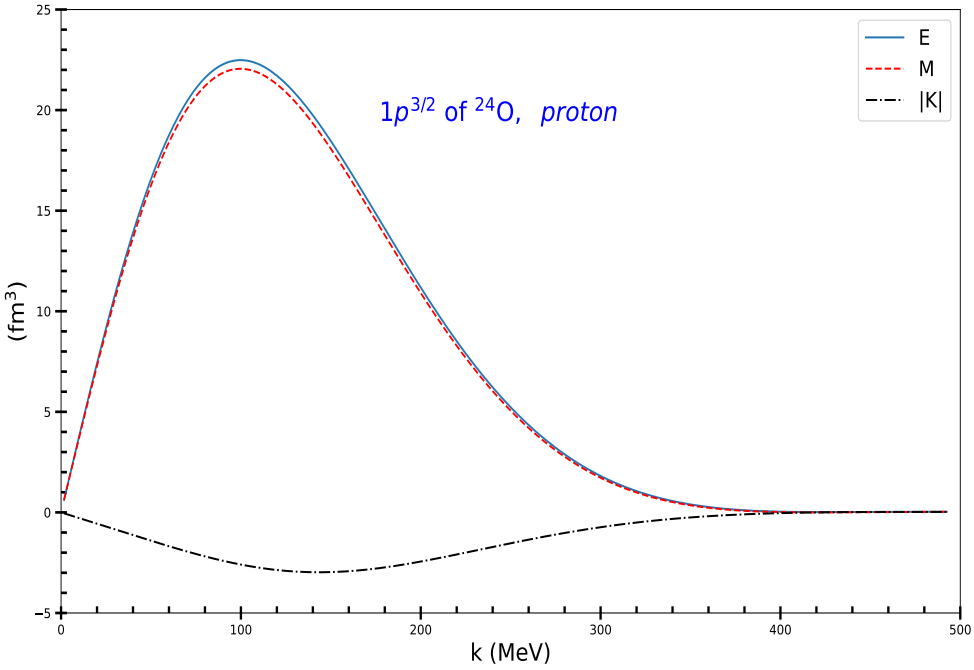

Figure C.1: The effective energy-, mass-, momentum-like quantities as a function of momentum for the $1p^{3/2}$ proton state of ^{24}O.

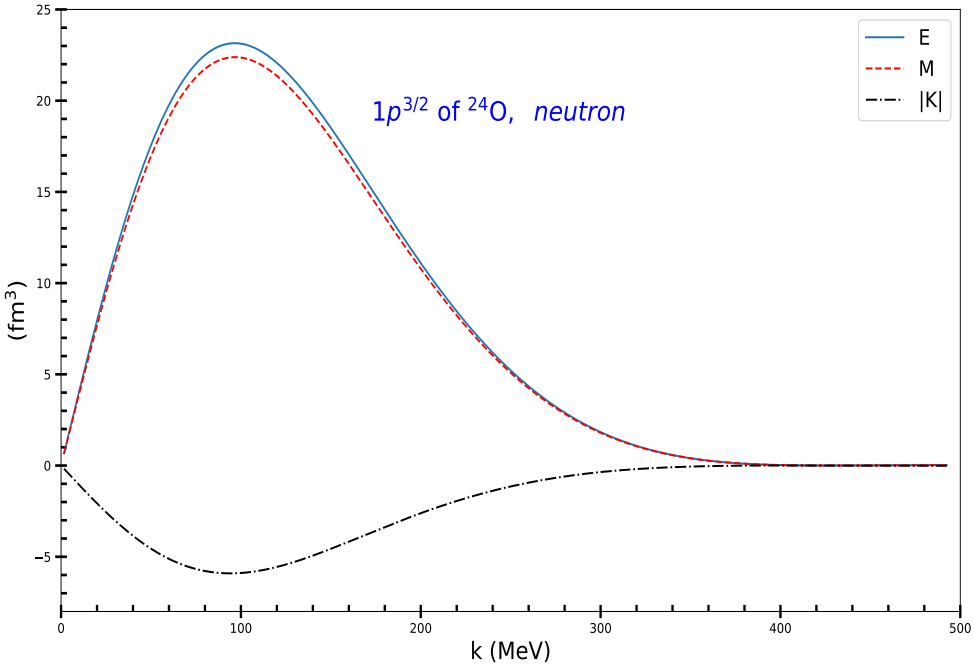

Figure C.2: The effective energy-, mass-, momentum-like quantities as a function of momentum for the $1p^{3/2}$ neutron state of ^{24}O.

Bibliography

[1] M. Wang, G. Audi, F. Kondev, W. Huang, S. Naimi, and X. Xu, "The AME2016 atomic mass evaluation (II). Tables, graphs and references," *Chinese Physics C*, vol. 41, no. 3, p. 030003, 2017.

[2] G. Lalazissis, J. König, and P. Ring, "New parametrization for the Lagrangian density of relativistic mean field theory," *Physical Review C*, vol. 55, no. 1, p. 540, 1997.

[3] B. Todd-Rutel and J. Piekarewicz, "Neutron-rich nuclei and neutron stars: A new accurately calibrated interaction for the study of neutron-rich matter," *Physical review letters*, vol. 95, no. 12, p. 122501, 2005.

[4] J. L. Friar, G. Payne, V. Stoks, and J. De Swart, "Triton calculations with the new Nijmegen potentials," *Physics Letters B*, vol. 311, no. 1-4, pp. 4–8, 1993.

[5] A. Nogga, D. Hüber, H. Kamada, and W. Glöckle, "Triton binding energies for modern NN forces and the π-π exchange three-nucleon force," *Physics Letters B*, vol. 409, no. 1-4, pp. 19–25, 1997.

[6] N. Barnea, W. Leidemann, and G. Orlandini, "State-dependent effective interaction for the hyperspherical formalism with noncentral forces," *Nuclear Physics A*, vol. 693, no. 3-4, pp. 565–578, 2001.

[7] H. Kamada, A. Nogga, W. Gloeckle, E. Hiyama, M. Kamimura, K. Varga, Y. Suzuki, M. Viviani, A. Kievsky, S. Rosati, *et al.*, "Benchmark test calculation of a four-nucleon bound state," *Physical Review C*, vol. 64, no. 4, p. 044001, 2001.

[8] J. Walecka, "A theory of highly condensed matter," *Annals of physics*, vol. 83, no. 2, pp. 491–529, 1974.

[9] Serot, BD and Walecka, JD, "Advances in Nuclear Physics, edited by JW Negele and E. Vogt," 1986.

[10] Clark, BC and Mercer, Robert L and Ravenhall, DG and Saperstein, AM, "Optical-Model Partial-Wave Analysis of 1-GeV Proton-Nucleus Elastic Scattering," *Physical Review C*, vol. 7, no. 1, p. 466, 1973.

[11] Arnold, LG and Clark, BC and Mercer, RL and Ravenhall, DG and Saperstein, AM, "Optical-model partial-wave analyses of p-^{4}He elastic scattering," *Physical Review C*, vol. 14, no. 5, p. 1878, 1976.

[12] L. Arnold, B. Clark, and R. Mercer, "Relativistic optical model analysis of medium energy p-^{4}He elastic scattering experiments," *Physical Review C*, vol. 19, no. 3, p. 917, 1979.

[13] L. G. Arnold, B. Clark, R. Mercer, and P. Schwandt, "Dirac optical model analysis of p - ^{40}Ca elastic scattering at 180 MeV and the wine-bottle-bottom shape," *Physical Review C*, vol. 23, no. 5, p. 1949, 1981.

[14] B. Clark, "The Interaction Between Medium Energy Nucleons in Nuclei-1982, Proceedings of the Workshop of the Interaction Between Medium Energy Nucleons in Nuclei," in *AIP Conf.*, AIP, 1983.

[15] J. McNeil, J. Shepard, and S. Wallace, "Impulse-approximation dirac optical potential," *Physical Review Letters*, vol. 50, no. 19, p. 1439, 1983.

[16] J. McNeil, L. Ray, and S. J. Wallace, "Impulse approximation nn amplitudes for proton-nucleus interactions," *Physical Review C*, vol. 27, no. 5, p. 2123, 1983.

[17] C. J. Horowitz and D. P. Murdock, "Quasielastic proton-nucleus scattering in a relativistic plane-wave impulse approximation," *Physical Review C*, vol. 37, no. 5, p. 2032, 1988.

[18] O. Chamberlain and E. Segrè, "Proton-proton collisions within lithium nuclei," *Physical Review*, vol. 87, no. 1, p. 81, 1952.

[19] J. Cladis, W. Hess, and B. Moyer, "Nucleon momentum distributions in deuterium and carbon inferred from proton scattering," *Physical Review*, vol. 87, no. 3, p. 425, 1952.

[20] T. Gooding and H. Pugh, "Quasi-elastic scattering of 153 MeV protons by p-state protons in C12: I. Experimental," *Nuclear Physics*, vol. 18, pp. 46–64, 1960.

[21] H. Tyren, S. Kullander, O. Sundberg, R. Ramachandran, P. Isacsson, and T. Berggren, "Quasi-free proton-proton scattering in light nuclei at 460 MeV," *Nuclear Physics*, vol. 79, no. 2, pp. 321–373, 1966.

[22] B. Gottschalk and K. Strauch, "Quasi-Elastic Proton-Proton Scattering at 158 MeV," *Physical Review*, vol. 120, no. 3, p. 1005, 1960.

[23] J. Roynette, C. Ruhla, M. Arditi, J. Jacmart, and M. Riou, "Nouvelle etude des reactions (p,2p) sur ^{6}Li et ^{7}Li a 155 MeV," *Physics Letters*, vol. 19, no. 6, pp. 497–499, 1965.

[24] P. Kitching and W. McDonald, "Th. AJ Maris, and CAZ Vasconcellos," *Adv. Nucl. Phys*, vol. 15, p. 43, 1985.

[25] K. Hatanaka, M. Kawabata, N. Matsuoka, Y. Mizuno, S. Morinobu, M. Nakamura, T. Noro, A. Okihana, K. Sagara, K. Takahisa, *et al.*, "Exclusive measurement of proton quasifree scattering and density dependence of the nucleon-nucleon interaction," *Physical review letters*, vol. 78, no. 6, p. 1014, 1997.

[26] K. Lim and I. McCarthy, "Information about the two-body force inside nuclei from $(p, 2p)$ reactions," *Physical Review Letters*, vol. 13, no. 14, p. 446, 1964.

[27] N. Kanayama, Y. Kudo, H. Tsunoda, and T. Wakasugi, "Various effects on the nonrelativistic dwia for $(p, 2p)$ reactions," *Progress of Theoretical Physics*, vol. 83, no. 3, pp. 540–551, 1990.

[28] Krein, G and Maris, Th AJ and Rodrigues, Benhur Borges and Veit, Eliane Angela, "Medium effects on spin observables of proton knockout reactions," *Physical Review C*, vol. 51, no. 5, p. 2646, 1995.

[29] G. Jacob and T. A. Maris, "Quasi-free scattering and nuclear structure," *Reviews of Modern Physics*, vol. 38, no. 1, p. 121, 1966.

[30] G. Jacob and T. A. Maris, "Quasi-Free Scattering and Nuclear Structure. II.," *Reviews of Modern Physics*, vol. 45, no. 1, p. 6, 1973.

[31] A. Antonov, M. Gaidarov, M. Ivanov, D. Kadrev, M. Aïche, G. Barreau, S. Czajkowski, B. Jurado, G. Belier, A. Chatillon, *et al.*, "The electron-ion scattering experiment ELISe at the International Facility for Antiproton and Ion Research (FAIR)—A conceptual design study," *Nuclear Instruments and Methods in Physics Research Section A: Accelerators, Spectrometers, Detectors and Associated Equipment*, vol. 637, no. 1, pp. 60–76, 2011.

[32] Tanihata, I and Hamagaki, H and Hashimoto, Oe and Shida, Y and Yoshikawa, N and Sugimoto, K and Yamakawa, O and Kobayashi, T and Takahashi, N, "Measurements of interaction cross sections and nuclear radii in the light *p*-shell region," *Physical Review Letters*, vol. 55, no. 24, p. 2676, 1985.

[33] H. Simon, D. Aleksandrov, T. Aumann, L. Axelsson, T. Baumann, M. Borge, L. Chulkov, R. Collatz, J. Cub, W. Dostal, *et al.*, "Direct experimental evidence for strong admixture of different parity states in ^{11}Li," *Physical review letters*, vol. 83, no. 3, p. 496, 1999.

[34] Navin, A and Anthony, DW and Aumann, T and Baumann, T and Bazin, Dominique and Blumenfeld, Y and Brown, BA and Glasmacher, T and Hansen, PG and Ibbotson, RW and others, "Direct Evidence for the Breakdown of the N = 8 Shell Closure in ^{12} Be," *Physical review letters*, vol. 85, no. 2, p. 266, 2000.

[35] J. Terry, D. Bazin, B. Brown, C. Campbell, J. Church, J. Cook, A. Davies, D.-C. Dinca, J. Enders, A. Gade, *et al.*, "Direct evidence for the onset of intruder configurations in neutron-rich Ne isotopes," *Physics Letters B*, vol. 640, no. 3, pp. 86–90, 2006.

[36] M. Thoennessen, "Current status and future potential of nuclide discoveries," *Reports on Progress in Physics*, vol. 76, no. 5, p. 056301, 2013.

[37] I. Tanihata, "Neutron halo nuclei," *Journal of Physics G: Nuclear and Particle Physics*, vol. 22, no. 2, p. 157, 1996.

[38] A. Ozawa, T. Kobayashi, T. Suzuki, K. Yoshida, and I. Tanihata, "New magic number, N = 16, near the neutron drip line," *Physical review letters*, vol. 84, no. 24, p. 5493, 2000.

[39] P. Adrich, A. Klimkiewicz, M. Fallot, K. Boretzky, T. Aumann, D. Cortina-Gil, U. D. Pramanik, T. W. Elze, H. Emling, H. Geissel, *et al.*, "Evidence for Pygmy and Giant Dipole Resonances in ^{130}Sn and ^{132}Sn," *Physical review letters*, vol. 95, no. 13, p. 132501, 2005.

[40] T. Otsuka, R. Fujimoto, Y. Utsuno, B. A. Brown, M. Honma, and T. Mizusaki, "Magic numbers in exotic nuclei and spin-isospin properties of the NN interaction," *Physical Review Letters*, vol. 87, no. 8, p. 082502, 2001.

[41] J. Dobaczewski, I. Hamamoto, W. Nazarewicz, and J. Sheikh, "Nuclear shell structure at particle drip lines," *Physical review letters*, vol. 72, no. 7, p. 981, 1994.

[42] B. Chen, J. Dobaczewski, K.-L. Kratz, K. Langanke, B. Pfeiffer, F.-K. Thielemann, and P. Vogel, "Influence of shell-quenching far from stability on the astrophysical r-process," *Physics Letters B*, vol. 355, no. 1-2, pp. 37–44, 1995.

[43] R. Kanungo, C. Nociforo, A. Prochazka, T. Aumann, D. Boutin, D. Cortina-Gil, B. Davids, M. Diakaki, F. Farinon, H. Geissel, *et al.*, "One-Neutron Removal Measurement Reveals ^{24}O as a New Doubly Magic Nucleus," *Physical review letters*, vol. 102, no. 15, p. 152501, 2009.

[44] Hoffman, CR and Baumann, T and Bazin, D and Brown, J and Christian, G and Denby, Deborah H and DeYoung, PA and Finck, JE and Frank, N and Hinnefeld, J and others, "Evidence for a doubly magic ^{24}O," *Physics Letters B*, vol. 672, no. 1, pp. 17–21, 2009.

[45] R. V. Janssens, "Unexpected doubly magic nucleus," *Nature*, vol. 459, no. 7250, pp. 1069–1070, 2009.

[46] M. Stanoiu, F. Azaiez, Z. Dombrádi, O. Sorlin, B. Brown, M. Belleguic, D. Sohler, M. Saint Laurent, M. Lopez-Jimenez, Y. Penionzhkevich, *et al.*, " N = 14 and 16 shell gaps in neutron-rich oxygen isotopes," *Physical Review C*, vol. 69, no. 3, p. 034312, 2004.

[47] D. Sohler, M. Stanoiu, Z. Dombrádi, F. Azaiez, B. Brown, M. Saint-Laurent, O. Sorlin, Y.-E. Penionzhkevich, N. Achouri, J. Angélique, *et al.*, "In-beam γ-ray spectroscopy of the neutron-rich nitrogen isotopes $^{19-22}$N," *Physical Review C*, vol. 77, no. 4, p. 044303, 2008.

[48] C. Rodriguez-Tajes, D. Cortina-Gil, H. Alvarez-Pol, T. Aumann, E. Benjamim, J. Benlliure, M. Borge, M. Caamano, E. Casarejos, A. Chatillon, *et al.*, "Structure of ^{22}N and the N = 14 subshell," *Physical Review C*, vol. 83, no. 6, p. 064313, 2011.

[49] M. Stanoiu, D. Sohler, O. Sorlin, F. Azaiez, Z. Dombrádi, B. Brown, M. Belleguic, C. Borcea, C. Bourgeois, Z. Dlouhy, *et al.*, "Disappearance of the N = 14 shell gap in the carbon isotopic chain," *Physical Review C*, vol. 78, no. 3, p. 034315, 2008.

[50] B. Jonson, "Light dripline nuclei," *Physics Reports*, vol. 389, no. 1, pp. 1–59, 2004.

[51] M. Lindroos, "Review of isol-type radioactive beam facilities," in *Proceedings of EPAC*, vol. 2004, p. 6, 2004.

[52] P. Van Duppen, "Isotope separation on line and post acceleration," in *The Euroschool Lectures on Physics with Exotic Beams, Vol. II*, pp. 37–77, Springer, 2006.

[53] D. J. Morrissey and B. M. Sherrill, "Radioactive nuclear beam facilities based on projectile fragmentation," *Philosophical Transactions of the Royal Society of London. Series A: Mathematical, Physical and Engineering Sciences*, vol. 356, no. 1744, pp. 1985–2006, 1998.

[54] M. Leino, "In-flight separation with gas-filled systems," *Nuclear Instruments and Methods in Physics Research Section B: Beam Interactions with Materials and Atoms*, vol. 126, no. 1-4, pp. 320–328, 1997.

[55] T. Wakasa, K. Ogata, and T. Noro, "Proton-induced knockout reactions with polarized and unpolarized beams," *Progress in Particle and Nuclear Physics*, vol. 96, pp. 32–87, 2017.

[56] S. Sakaguchi, T. Uesaka, T. Wakui, S. Chebotaryov, T. Kawahara, S. Kawase, E. Milman, T. L. Tang, K. Tateishi, and T. Teranishi, "Studies of unstable nuclei with spin-polarized proton target," in *International Journal of Modern Physics: Conference Series*, vol. 40, p. 1660071, World Scientific, 2016.

[57] J. D. Bjorken and S. D. Drell, "Relativistic quantum mechanics," 1964.

[58] B. D. Serot, "A relativistic nuclear field theory with π and ρ mesons," *Physics Letters B*, vol. 86, no. 2, pp. 146–150, 1979.

[59] J. Boguta and A. Bodmer, "Relativistic calculation of nuclear matter and the nuclear surface," *Nuclear Physics A*, vol. 292, no. 3, pp. 413–428, 1977.

[60] P.-G. Reinhard, M. Rufa, J. Maruhn, W. Greiner, and J. Friedrich, "Nuclear ground-state properties in a relativistic meson-field theory," *Zeitschrift für Physik A Atomic Nuclei*, vol. 323, no. 1, pp. 13–25, 1986.

[61] S.-J. Lee, J. Fink, A. Balantekin, M. Strayer, and A. Umar, "PG. Reinhard, JA Maruhn and W. Greiner," *Phy. Rev. Lett*, vol. 57, no. 2916, p. 59, 1986.

[62] M. Sharma, M. Nagarajan, and P. Ring, "Rho meson coupling in the relativistic mean field theory and description of exotic nuclei," *Physics Letters B*, vol. 312, no. 4, pp. 377–381, 1993.

[63] Y. Sugahara and H. Toki, "Relativistic mean-field theory for unstable nuclei with non-linear σ and ω terms," *Nuclear Physics A*, vol. 579, no. 3-4, pp. 557–572, 1994.

[64] W. Long, J. Meng, N. Van Giai, and S.-G. Zhou, "New effective interactions in relativistic mean field theory with nonlinear terms and density-dependent meson-nucleon coupling," *Physical Review C*, vol. 69, no. 3, p. 034319, 2004.

[65] J. Blaizot, D. Gogny, and B. Grammaticos, "Nuclear compressibility and monopole resonances," *Nuclear Physics A*, vol. 265, no. 2, pp. 315–336, 1976.

[66] H. Mueller and B. D. Serot, "Relativistic mean-field theory and the high-density nuclear equation of state," *arXiv preprint nucl-th/9603037*, 1996.

[67] C. Horowitz and J. Piekarewicz, "Neutron star structure and the neutron radius of ^{208}Pb," *Physical Review Letters*, vol. 86, no. 25, p. 5647, 2001.

[68] C. J. Horowitz and D. P. Murdock, "Quasielastic proton-nucleus scattering in a relativistic plane-wave impulse approximation," *Physical Review C*, vol. 37, no. 5, p. 2032, 1988.

[69] C. Chan, T. Drake, R. Abegg, D. Frekers, and O. Häusser, "K, hicks, da hutcheon, l. lee, ca miller, r. schubank, ej stepehenson and s. yen," *J. Phys. G*, vol. 15, p. L55, 1989.

[70] C. Chan, T. Drake, R. Abegg, D. Frekers, O. Häusser, K. Hicks, D. Hutcheon, L. Lee, C. Miller, R. Schubank, *et al.*, "A complete measurement of spin-observables for intermediate-energy inclusive quasielastic polarized proton scattering from 12c," *Nuclear Physics A*, vol. 510, no. 4, pp. 713–730, 1990.

[71] B. Van der Ventel, G. Hillhouse, P. De Kock, and S. Wallace, "Polarization transfer observables for quasielastic proton-nucleus scattering in terms of a complete Lorentz invariant representation of the NN scattering matrix," *Physical Review C*, vol. 60, no. 6, p. 064618, 1999.

[72] G. Hillhouse, B. van der Ventel, and P. de Kock, "Sensitivity of quasielastic proton-nucleus analyzing power to nuclear medium effects," *Czechoslovak Journal of Physics*, vol. 51, no. 1, pp. A213–A220, 2001.

[73] C. Miller, K. Hicks, R. Abegg, M. Ahmad, N. Chant, D. Frekers, P. Green, L. Greeniaus, D. Hutcheon, P. Kitching, *et al.*, "Spin-dependent scattering of deeply bound nucleons," *Physical Review C*, vol. 57, no. 4, p. 1756, 1998.

[74] T. Noro, T. Baba, K. Hatanaka, M. Ito, M. Kawabata, N. Matsuoka, Y. Mizuno, S. Morinobu, M. Nakamura, A. Okihana, *et al.*, "A study of nucleon properties in nuclei through (p, 2p) reactions," *Nuclear Physics A*, vol. 629, no. 1-2, pp. 324–333, 1998.

[75] B. Van der Ventel and G. Hillhouse, "Sensitivity of exclusive proton knockout spin observables to different lorentz invariant representations of the nn interaction," *Physical Review C*, vol. 69, no. 2, p. 024618, 2004.

[76] S. Wyngaardt, *Relativistic plane wave description of spin transfer observables for proton knock-out reactions*. PhD thesis, Stellenbosch University, 2001.

[77] Y. Kudo and K. Miyazaki, "Analyzing powers for (p,2p) reactions with effective NN interactions," *Physical Review C*, vol. 34, no. 4, p. 1192, 1986.

[78] G. Hillhouse, J. Mano, S. Wyngaardt, B. Van der Ventel, T. Noro, and K. Hatanaka, "Relativistic predictions of spin observables for exclusive proton knockout reactions," *Physical Review C*, vol. 68, no. 3, p. 034608, 2003.

[79] Tjon, JA and Wallace, Stephen J, "General Lorentz-invariant representation of NN scattering amplitudes," *Physical Review C*, vol. 32, no. 5, p. 1667, 1985.

[80] Tjon, JA and Wallace, SJ, "Generalized impulse approximation for relativistic proton scattering," *Physical Review C*, vol. 36, no. 3, p. 1085, 1987.

[81] Goldberger, Marvin Leonard and Nambu, Yoichiro and Oehme, Reinhard, "Dispersion relations for nucleon-nucleon scattering," *Annals of Physics*, vol. 2, no. 3, pp. 226–282, 1957.

[82] G. E. Brown and A. D. Jackson, "The nucleon-nucleon interaction," *North-Holland Publishing Company, Amsterdam.*, 1976.

[83] D. Adams and M. Bleszynski, "On the relevance of the Dirac equation to the scattering of medium-energy nucleons from nuclei," *Physics Letters B*, vol. 136, no. 1-2, pp. 10–14, 1984.

[84] G. Hillhouse, B. van der Ventel, S. Wyngaardt, and P. De Kock, "Nuclear medium modifications of the NN interaction via quasielastic (p,p) and (p,n) scattering," *Physical Review C*, vol. 57, no. 1, p. 448, 1998.

[85] C. Horowitz, "Relativistic Love-Franey model: Covariant representation of the NN interaction for N-nucleus scattering," *Physical Review C*, vol. 31, no. 4, p. 1340, 1985.

[86] R. A. Arndt and D. Roper, *VPI and SU Scattering Analysis Interactive Dialin Program and Data Base.* 1986.

[87] K. Langanke, J. A. Maruhn, and S. E. Koonin, *Computational nuclear physics*. Springer, 1991.

[88] Y. W. Akanni, *A Microscopic Description of Elastic Scattering from Unstable Nuclei within a Relativistic Framework*. PhD thesis, Stellenbosch University, 2018.

[89] I. Angeli and K. P. Marinova, "Table of experimental nuclear ground state charge radii: An update," *Atomic Data and Nuclear Data Tables*, vol. 99, no. 1, pp. 69–95, 2013.

[90] S. Abrahamyan, Z. Ahmed, H. Albataineh, K. Aniol, D. Armstrong, W. Armstrong, T. Averett, B. Babineau, A. Barbieri, V. Bellini, *et al.*, "Measurement of the neutron radius of ^{208}Pb through parity violation in electron scattering," *Physical review letters*, vol. 108, no. 11, p. 112502, 2012.

[91] B. A. Brown, "The oxygen isotopes," *International Journal of Modern Physics E*, vol. 26, no. 01n02, p. 1740003, 2017.

[92] M. Thoennessen, "Reaching the limits of nuclear stability," *Reports on Progress in Physics*, vol. 67, no. 7, p. 1187, 2004.

[93] M. Langevin, E. Quiniou, M. Bernas, J. Galin, J. Jacmart, F. Naulin, F. Pougheon, R. Anne, C. Détraz, D. Guerreau, *et al.*, "Production of neutron-rich nuclei at the limits of particles stability by fragmentation of 44 MeVu ^{40}Ar projectiles," *Physics Letters B*, vol. 150, no. 1-3, pp. 71–74, 1985.

[94] M. Thoennessen, T. Baumann, B. Brown, J. Enders, N. Frank, P. Hansen, P. Heckman, B. Luther, J. Seitz, A. Stolz, *et al.*, "Single proton knock-out reactions from ^{24,25,26}F ," *Physical Review C*, vol. 68, no. 4, p. 044318, 2003.

[95] D. Guillemaud-Mueller, J. Jacmart, E. Kashy, A. Latimier, A. Mueller, F. Pougheon, A. Richard, Y. E. Penionzhkevich, A. Artuhk, A. Belozyorov, *et al.*, "Particle stability of the isotopes ^{26}O and Ne 32 in the reaction 44 MeV/nucleon ^{48}Ca + Ta," *Physical Review C*, vol. 41, no. 3, p. 937, 1990.

[96] M. Fauerbach, D. Morrissey, W. Benenson, B. Brown, M. Hellström, J. Kelley, R. Kryger, R. Pfaff, C. Powell, and B. Sherrill, "New search for o 26," *Physical Review C*, vol. 53, no. 2, p. 647, 1996.

[97] H. Sakurai, S. Lukyanov, M. Notani, N. Aoi, D. Beaumel, N. Fukuda, M. Hirai, E. Ideguchi, N. Imai, M. Ishihara, *et al.*, "Evidence for particle stability of ^{31}F and particle instability of ^{25}N and ^{28}O," *Physics Letters B*, vol. 448, no. 3-4, pp. 180–184, 1999.

[98] A. S. Konrod, *Nodes and weights of quadrature formulas.* Springer, 1965.

[99] J. Meng, H. Toki, S.-G. Zhou, S. Zhang, W. Long, and L. Geng, "Relativistic continuum hartree bogoliubov theory for ground-state properties of exotic nuclei," *Progress in Particle and Nuclear Physics*, vol. 57, no. 2, pp. 470–563, 2006.

[100] Y. Gambhir and P. Ring, "Relativistic mean-field description of the ground-state nuclear properties," *Pramana*, vol. 32, no. 4, pp. 389–404, 1989.

[101] S. Gardner and J. Piekarewicz, "Relativistically generated asymmetry in the missing-momentum distribution from the $(e, e'p)$ reaction," *Physical Review C*, vol. 50, no. 6, p. 2822, 1994.